

Thesis
2
2007

This is to certify that the
dissertation entitled

FEMTOSECOND SPECTROSCOPIC STUDIES OF
VIBRATIONAL COHERENCE FROM
BACTERIOCHLOROPHYLL SOLUTIONS AND LIGHT-
HARVESTING PROTEINS

presented by

Katherine R. Shelly

has been accepted towards fulfillment
of the requirements for the

Ph. D. degree in Chemistry

Warren F. Beck

Major Professor's Signature

2 June 2006

Date

MSU is an Affirmative Action/Equal Opportunity Institution

LIBRARY
Michigan State
University

PLACE IN RETURN BOX to remove this checkout from your record.
TO AVOID FINES return on or before date due.
MAY BE RECALLED with earlier due date if requested.

DATE DUE	DATE DUE	DATE DUE

**FEMTOSECOND SPECTROSCOPIC STUDIES OF VIBRATIONAL COHERENCE
FROM BACTERIOCHLOROPHYLL SOLUTIONS AND LIGHT-HARVESTING
PROTEINS**

By

Katherine R. Shelly

A DISSERTATION

**Submitted to
Michigan State University
in partial fulfillment of the requirements
for the degree of**

DOCTOR OF PHILOSOPHY

Department of Chemistry

2006

ABSTRACT

By

Katherine R. Shelly

The femtosecond dynamic-absorption technique was used to obtain pump-probe transients with impulsive excitation of the Q_y absorption band at room temperature in polar and non-polar solutions of bacteriochlorophyll a . The dynamics of bacteriochlorophyll a in protein-derived binding sites was characterized in experiments with the B777 and B820 subunits of the LH1 light-harvesting complex from *Rhodospirillum rubrum* G9. In all of the systems with strong axial ligation, from pyridines in solution or histidine residues in the protein, two time regions of vibrational coherence were observed: a rapidly damped portion, in the < 800 -fs time region, and a slowly damped portion, on the < 8 -ps time scale. Only the rapidly damped portion was observed in acetone or 1-propanol solutions. The slowly damped portion is assigned to narrow line shapes arising from intramolecular vibrations of the BChl macrocycle. The rapidly damped portion is assigned to inhomogeneously broadened line shapes arising from intermolecular modes with polar and non-polar components in the surrounding solvent or protein environment.

To BJ

for your unconditional encouragement and patience

ACKNOWLEDGMENTS

The work I have completed at Michigan State University is a result of collective efforts from my parents, family, and friends. I have received infinite support from the people who surround me, for which I would have never made it through the last five grueling years without.

This dissertation is dedicated first and foremost to my husband, BJ, for giving me the confidence to make it through this tumultuous endeavor. Your encouragement was and still is unmatched by any other. This degree is certainly as much yours as it is mine.

I also want to thank my graduate colleagues. You have made this experience one I will never forget. I will not only walk away from here with my degree, but I will have your friendship, which I value even more.

Finally, I would like to thank Professor Warren Beck. It is only with your guidance that I close this chapter of my life. You have provided me with the opportunities and knowledge that made my graduate experience more fulfilling than I could have ever imagined.

TABLE OF CONTENTS

LIST OF TABLES.....	viii
LIST OF FIGURES.....	ix
INTRODUCTION.....	1
CHAPTER 1	
INTRODUCTION.....	3
1.0 Photosynthetic Reaction Centers.....	3
1.0.1 Charge-Transfer Reactions in Photosynthetic Reaction Centers.....	3
1.0.2 Structure of the Photosynthetic Reaction Center.....	4
1.1 Electron-Transfer Theory.....	7
1.2 Coupled Modes in Photosynthesis.....	10
1.3 Assignments for the Coupled Modes.....	12
1.4 Resonance Raman Activity in Intermolecular Modes.....	13
1.5 Research Design.....	15
1.6 References.....	16
CHAPTER 2	
THEORY AND EXPERIMENTAL METHODS FOR THE STUDY OF VIBRATIONAL COHERENCE.....	22
2.0 Introduction	22
2.1. Theory.....	22
2.1.1 Wave Packets.....	22
2.1.2 Resonance Raman Spectroscopy.....	23
2.1.3 Dynamic-Absorption Spectroscopy.....	25
2.1.4 Frequency Domain vs. Time Domain.....	26
2.2 Experimental: Femtosecond Pump-Probe Spectrometer Design and Characterization.....	27
2.2.1 Ti:Sapphire Oscillator.....	27
2.2.2 Extracavity Pulse Compression.....	31
2.2.3 Rapid-Scanning Modified Mach-Zehnder Interferometer.....	31
2.2.3.1 Layout of Interferometer.....	31

2.3 Data Acquisition.....	37
2.4 References.....	42
CHAPTER 3	
VIBRATIONAL COHERENCE FROM THE DIPYRIDINE COMPLEX OF BACTERIOCHLOROPHYLL <i>a</i>: INTRAMOLECULAR MODES IN THE 10–220-cm⁻¹ REGIME, INTERMOLECULAR SOLVENT MODES, AND RELEVANCE TO PHOTOSYNTHESIS.....	
3.0 Introduction.....	45
3.1 Experimental Procedures.....	46
3.1.1 Sample Preparation.....	46
3.1.2 Continuous-Wave Spectroscopy.....	47
3.1.3 Femtosecond Spectroscopy.....	47
3.2 Results.....	47
3.2.1 Continuous-Wave Spectroscopy.....	47
3.2.2 Dynamic-Absorption Experiments.....	49
3.2.3 Rapidly-Damped Vibration Coherence from Bacteriochlorophyll <i>a</i> and Pyridine.....	51
3.3 Data Analysis.....	57
3.3.1 Fourier-Magnitude Spectrum Estimation.....	57
3.3.2 Modeling of the Slowly Damped Components.....	60
3.3.3 Modeling of the Rapidly Damped Component.....	60
3.4 Discussion.....	62
3.3.1 Observation of Two Damping Time Scales.....	62
3.5 References.....	67
CHAPTER 4	
INTERMOLECULAR VIBRATIONAL COHERENCE BETWEEN BACTERIOCHLOROPHYLL <i>a</i> AND POLAR AND NONPOLAR SOLVENTS.....	
4.0 Introduction.....	70
4.1 Experimental Procedures.....	70
4.1.1 Sample Preparation.....	70
4.1.1.1 Bacteriochlorophyll <i>a</i> in polar solvents.....	70
4.1.1.2 Bacteriochlorophyll <i>a</i> in nonpolar solvents.....	71
4.1.2 Continuous-Wave Spectroscopy.....	71
4.1.3 Femtosecond Spectroscopy.....	71
4.2 Results.....	72
4.2.1 Continuous-Wave Spectroscopy.....	72

4.2.2 Dynamic-Absorption Experiments.....	78
4.3 Discussion.....	91
4.3.1 Structural Assignments.....	92
4.3.2 Line Shapes for Intermolecular and Intramolecular Modes in Solution and Proteins.....	98
4.4 References.....	100
 CHAPTER 5	
INTERMOLECULAR VIBRATIONAL COHERENCE FROM BACTERIOCHLOROPHYLL- CONTAINING PROTEINS, B777 AND B820.....	
5.0 Introduction.....	106
5.1 Experimental Procedures.....	106
5.1.1 Sample Preparation.....	106
5.1.1.1 Isolation and Preparation of B820 Subunits.....	109
5.1.1.2 Isolation and Preparation of B777 Subunits.....	112
5.1.2 Continuous-Wave Spectroscopy.....	112
5.1.3 Femtosecond Spectroscopy.....	112
5.2 Results.....	113
5.2.1 Continuous-Wave Spectroscopy.....	113
5.2.2 Dynamic-Absorption Experiments.....	116
5.3 Discussion.....	123
5.3.1 Comparison of Rapidly-Damped Vibrational Coherence in B777 and B820.....	123
5.3.2 Assignments for Components in the Vibrational Coherence in B777 and B820.....	126
5.3.3 BChl–Protein Interactions in B820 and in the Photosynthetic Reaction Center.....	127
5.4 Conclusions and Future Work.....	130
5.5 References.....	134

LIST OF TABLES

Table		Page
3.1	Frequencies, normalized deconvolved intensities, and damping constants for the underdamped oscillatory components observed in the pump-probe signal from bacteriochlorophyll <i>a</i> in pyridine solvent	61
3.2	Log-normal line shape parameters for the solvent-mode distribution	64
4.1	Model parameters for the rapidly damped vibrational coherence observed in BChl <i>a</i> solutions	90
5.1	Model parameters for the rapidly damped vibrational coherence observed in BChl-containing proteins	122
5.2	Potential residue candidates for the interaction between the BChl dimer and the surrounding protein medium in B820	129
5.3	Potential residue candidates for the interaction between the BChl dimer and the surrounding protein medium in <i>Rhodobacter sphaeroides</i>	132

LIST OF FIGURES

Figure		Page
1.1	The photosynthetic reaction center from <i>Rhodospseudomonas viridis</i> , rendered from RCSB Protein Data Bank file 1ajj. This view shows the topology of the cytochrome (green, top), L (blue), M (pink), and H (green, bottom) subunits	5
1.2	Chromophores in the reaction center from <i>Rhodospseudomonas viridis</i> . The arrows represent the direction of the electron transfer reactions	6
1.3	Diabatic harmonic potential-energy curves for the reactant (E_a) and product (E_b) of an electron-transfer reaction as a function of the displacement of one of the normal modes of vibration n ; λ_n marks the mode-specific reorganization energy, and $-\Delta E^0$ is the driving force	8
2.1	Excited-state and ground-state coherent wave-packet motion in the dynamic absorption experiment. The excited-state and ground-state potential-energy surfaces are drawn as parabolas that are displaced with respect to a generalized multimode coordinate; r_g and r_e mark the equilibrium ground-state and excited-state geometries, respectively. Thick arrows represent the resonant pump-laser field; thin arrows show the direction that the wave packets evolve during the first passage on the two surfaces. The numbers indicate event times, starting with ground-state probability density, creation of the excited-state wave packet by the pump field, creation of the ground-state wave packet by the pump field, and evolution during the first vibration	24
2.2	The Mira 900-F ti:sapphire laser oscillator and pulse compressor employed in the dynamic-absorption spectroscopy experiments. <i>Symbols</i> : M1, output coupler; BP1-BP2, Brewster prisms; M2-M3, flat cavity mirrors; BRF, birefringent filter; L1, focusing lens; M4-M5, curved mirrors; TiAl ₂ O ₃ , titanium: sapphire crystal; M6, flat mirror; M7, flat end mirrors; p1-p2, SF10 prisms	28
2.3	Output intensity spectrum of 60-fs (sech ² ; 12-nm (fwhm) spectral width) pulses from the ti:oscillator	29
2.4	Zero-background autocorrelation trace of a 60-fs (sech ²) pulse obtained from the ti:sapphire oscillator	30
2.5	Extracavity compressor employed in the dynamic-absorption spectroscopy experiments. <i>Symbols</i> : M1-M6, silver mirrors; M7, half silver mirror; p1-p2, SF10 Brewster-angled prisms	32

2.6	Modified Mach-Zehnder rapid-scanning interferometer employed in the dynamic-absorption spectroscopy experiments. <i>Symbols</i> : M1-M9, silver mirrors; BS1-BS2, beam splitters; C1-C2, compensation optics; $\lambda/2$, half-wave plates; P1-P2, Glan-laser calcite polarizers; PEM-90, photoelastic modulator	33
2.7	Sample and detection portion of the Modified Mach-Zehnder rapid-scanning interferometer employed in the dynamic-absorption spectroscopy experiments. <i>Symbols</i> : M1-M6, silver mirrors; BS1, beam splitters; C1, compensation optics; P1, Glan-laser calcite polarizers; α , β -barium borate crystal; PMT, photomultiplier tube; PD, photodiode	34
2.8	Multiple traces obtained simultaneously during dynamic-absorption experiments of bacteriochlorophyll <i>a</i> in pyridine. The probe beam was detected at 757 nm. Two complete scans of the rapid-scanning delay stage are shown as a function of real time. <i>Top</i> : Pump-probe delay determined from the position of the rapid-scanning delay stage. <i>Middle</i> : Zero-background autocorrelation. <i>Bottom</i> : Single-wavelength dynamic-absorption transient	38
2.9	Zoomed traces from figure 2.8. obtained from bacteriochlorophyll <i>a</i> in pyridine. The probe beam was detected at 757 nm. A portion of one scan of the pump-probe delay is shown as a function of real time. <i>Top</i> : Probe delay as determined from the position of the rapid-scanning delay stage. <i>Middle</i> : Zero-background autocorrelation. <i>Bottom</i> : Single-wavelength dynamic-absorption transient	40
2.10	Single-wavelength dynamic-absorption transient of bacteriochlorophyll <i>a</i> in pyridine solvent displayed as a function of probe delay. The probe beam was detected at 757 nm	41
3.1	Continuous-wave absorption and fluorescence spectra from bacteriochlorophyll <i>a</i> in pyridine plotted as relative dipole strengths, $A(\nu)/\nu$ and $F(\nu)/\nu^3$, respectively. The spectra are normalized to unit area. The fluorescence spectrum was excited at 790 nm (12700 cm^{-1})	48
3.2	Pump-probe signal obtained from BChl in pyridine solvent	50
3.3	Triple exponential fit (top) and corresponding residual oscillatory part of the pump-probe signal from BChl in pyridine (bottom)	52
3.4	Hanning-windowed Fourier-magnitude spectrum of the 200-8000-fs range	53

3.5	Pump-probe signal obtained under the same optical conditions from BChl in pyridine solvent and in neat pyridine. The top graph shows the range corresponding to the population change in the BChl ground state. The y axes employ a consistent relative-intensity scaling	55
3.6	Oscillatory signal with a frequency of 200 cm^{-1} and a damping time of 100 fs (top panel). Oscillatory signal from top panel multiplied by a Hanning window function described by equation 3.1 (middle panel). Hanning-windowed Fourier-magnitude spectrum of the 200-cm^{-1} oscillation (bottom panel)	59
3.7	Expanded view of the rapidly damped oscillation from BChl in pyridine solvent (see figure 3.5.) superimposed with a model (dashed curve) arising from a distribution of mode frequencies, as shown in the bottom panel	63
4.1	Continuous-wave absorption spectra at $22\text{ }^{\circ}\text{C}$ from BChl <i>a</i> in cyclohexane solvent at BChl:pyridine ratios of (a)1:0.6, (b)1:1.2, and (c)1:100. The vertical line represents 580 nm	73
4.2	Continuous-wave absorption spectra at $22\text{ }^{\circ}\text{C}$ from BChl <i>a</i> in three neat solvents: (a) pyridine, (b) 1-propanol, and (c) acetone	74
4.3	Structure of bacteriochlorophyll <i>a</i> molecule, the dominant chromophore in purple non-sulfur photosynthetic light-harvesting proteins	76
4.4	Continuous-wave absorption and fluorescence spectra from BChl in pyridine solvent plotted as the dipole strength, $A(\nu)/\nu$ and $F(\nu)/\nu^3$, respectively, and normalized to unit area. The dashed curve shows the intensity spectrum emitted by the titanium-sapphire oscillator. The shaded region shows the range of the transmitted probe light that was passed by the monochromator to the detector in the dynamic-absorption experiment	77
4.5	Dynamic-absorption transient from BChl in pyridine. The inset shows an expanded view of the 0–1-ps portion of the signal. The ordinate is scaled relative to the magnitude of the pump-induced change in transmission that follows the initial (0-5 ps) exponential decay arising from solvation dynamics	79
4.6	Expanded view of the rapidly damped oscillation observed in the dynamic-absorption transient from BChl <i>a</i> in pyridine (see figure 4.5) and three optimized single-modulation-component models employing different line shapes: (a) a discrete 225-cm^{-1} cosinusoid (equation 4.1) with the damping time $\gamma = 92\text{ fs}$, (b) a Gaussian distribution of damped cosinusoids with a center frequency of 225 cm^{-1} and a width (fwhm) of	

50 cm^{-1} , and (c) a log-normal distribution of damped cosinusoids with a center frequency of 285 cm^{-1} and a width (fwhm) of 97 cm^{-1} . The models for (b) and (c) were defined by equation 4.2, with the distributions $\mathcal{L}(\omega)$ set as a Gaussian and as a log-normal, respectively. The scaling of the ordinate is relative to the magnitude of the pump–probe ground-state depletion signal, as indicated in figure 4.5

81

4.7 Modeling the rapidly damped vibrational coherence observed in BChl *a* solutions with a distribution of slowly damped cosinusoids, $\mathcal{L}(\omega)$, as defined by equation 4.2. A log-normal distribution $\mathcal{L}(\omega)$, (a), defined by its center frequency, ω_0 , width, $\Delta\omega$, and asymmetry (or skew), ρ , is sampled over its full width. Each sample defines the intensity of a Lorentzian line shape that corresponds in the time domain, (b), to a cosinusoid at the sampled frequency ω with a homogeneous (or intrinsic) damping time, γ , here set arbitrarily to 1.5 ps. Summing of the cosinusoids obtained by sampling over the full width of the distribution $\mathcal{L}(\omega)$, (c), results in a rapidly damped waveform, (d), that resembles the vibrational coherence observed in BChl solutions

82

4.8 Expanded view of the rapidly damped oscillation observed in the dynamic-absorption transient from BChl *a* in pyridine (see figures 4.5 and 4.6) superimposed with a model defined by the sum of two independent log-normal distributions $\mathcal{L}(\omega)$ of damped cosinusoids, each defined by equation 4.2. The scaling of the ordinate is relative to the magnitude of the pump–probe ground-state depletion signal, as in figure 4.5. *Bottom*: Plots of $\mathcal{L}(\omega)$ for the two components observed in pyridine and their sum, $\mathcal{M}(\omega)$ (thick curve). The model parameters are provided in table 4.1

85

4.9 Expanded view of the rapidly damped oscillation observed in the dynamic-absorption transient from BChl *a* in acetone superimposed with a model defined by the sum of two independent log-normal distributions $\mathcal{L}(\omega)$ of damped cosinusoids, each defined by equation 4.2. The scaling of the ordinate is relative to the magnitude of the pump–probe ground-state depletion signal, as in figure 4.5. *Bottom*: Plots of $\mathcal{L}(\omega)$ for the two components observed in acetone and their sum, $\mathcal{M}(\omega)$ (thick curve). The model parameters are provided in table 4.1

86

4.10 Expanded view of the rapidly damped oscillation observed in the dynamic-absorption transient from BChl *a* in 1-propanol superimposed with a model defined by the sum of three independent log-normal distributions $\mathcal{L}(\omega)$ of damped cosinusoids, each defined by equation 4.2. The scaling of the ordinate is relative to the magnitude of the pump–probe ground-state depletion signal, as in figure 4.5. *Bottom*: Plots of $\mathcal{L}(\omega)$ for the three components observed in 1-propanol and their sum.

	$\mathcal{L}(\omega)$ for the three components observed in 1-propanol and their sum, $\mathcal{M}(\omega)$ (thick curve). The model parameters are provided in table 4.1	88
4.11	Expanded view of the rapidly damped oscillation observed in the dynamic-absorption transient from BChl <i>a</i> with a single pyridine axial ligand in cyclohexane superimposed with a model defined by the sum of two independent log-normal distributions $\mathcal{L}(\omega)$ of damped cosinusoids, each defined by equation 4.2. The scaling of the ordinate is relative to the magnitude of the pump-probe ground-state depletion signal, as in figure 4.5. <i>Bottom</i> : Plots of $\mathcal{L}(\omega)$ for the two components observed in cyclohexane and their sum, $\mathcal{M}(\omega)$ (thick curve)	89
4.12	A possible model obtained using a molecular mechanics calculation with the MMX force field and the PCModel program for the interaction between two non-ligated pyridine solvent molecules and the π -electron density of the BChl macrocycle in the dipyridine complex	95
4.13	A possible model obtained using a molecular mechanics calculation with the MMX force field and the PCModel program for the interaction between acetone solvent dipoles and the π -electron density of the BChl macrocycle	96
5.1	Model of the LH1 light-harvesting complex generated from the calculations of Schulten and coworkers. Only the chromophores are shown here. (Refer to figure 5.3 for the details of how each pair of BChl are divided by a pair of membrane-separating α helices.)	104
5.2	Crystal structure of the LH2 complex from <i>Rhodospseudomonas acidophila</i> as reported by Caffrey and coworkers. The α and β units are shown in red and blue, respectively, the B800 pigments in purple, the B850 pigments in green, and the carotenoids in yellow. The structure can be found under the accession number 2FKW in the RCSB Protein Data Bank	105
5.3	Model of the B820 subunit from LH1 based on the calculations of Schulten and coworkers	107
5.4	Hypothesized model for the B777 subunit formed from the B820 subunit of LH1. LH1 is the result of dissociating B820 into two polypeptides, each with a single ligated BChl macrocycle, so there are two possible B777 structures in a given sample	108
5.5	Absorption spectra illustrating the formation of B777 subunits from detergent-solublized chromatophores isolated from <i>R. rubrum</i> G9, top panel. At low concentrations of <i>n</i> -octyl- <i>rac</i> -2,3-dipropyl sulfoxide	

- (ODPS), only the chromatophores are present, as indicated by the absorption maximum at 873 nm. At intermediate detergent concentrations, chromatophores, B820 subunits and B777 subunits are all present within the sample. The B820 population is indicated by the formation of the absorption peak at 820 nm. B777 subunits are exclusively present at an increased concentration of ODPS detergent (~3.0% (w/v)). The bottom panel shows an expanded view of the Q_y absorption band, so that the conversion of the initial 870 nm peak to the 777 nm peak can be more easily observed 110
- 5.6 Absorption spectra illustrating the formation of B820 subunits from detergent-solubilized chromatophores isolated from *R. rubrum* G9 over a period of 17 hours, top panel. The chromatophores were solubilized with 0.75% (w/v) octyl β -D-glucopyranoside (OG). The bottom panel shows an expanded view of the Q_y absorption band. No chromatophores are present in the sample 22 hours after the addition of OG solution 111
- 5.7 Continuous-wave absorption and fluorescence spectra from B777 in ODPS plotted as the dipole strength, $A(\nu)/\nu$ and $F(\nu)/\nu^3$, respectively, and normalized to unit area. The dashed curve shows the intensity spectrum emitted by the ti:sapphire oscillator. The shaded region shows the range of the transmitted probe light that was passed by the monochromator to the detector in the dynamic-absorption experiment 114
- 5.8 Continuous-wave absorption and fluorescence spectra from B820 in OG plotted as the dipole strength, $A(\nu)/\nu$ and $F(\nu)/\nu^3$, respectively, and normalized to unit area. The dashed curve shows the intensity spectrum emitted by the ti:sapphire oscillator. The shaded region shows the range of the transmitted probe light that was passed by the monochromator to the detector in the dynamic-absorption experiment 115
- 5.9 Pump-probe signal obtained from B777 in ODPS at room temperature 117
- 5.10 Pump-probe signal obtained from B820 in OG at room temperature 118
- 5.11 Expanded view of the rapidly damped oscillation observed in the dynamic-absorption transient from B777 in ODPS (see figure 5.9) superimposed with a model defined by the sum of two independent log-normal distributions $\mathcal{L}(\omega)$ of damped cosinusoids, each defined by equation 5.2. The scaling of the ordinate is relative to the magnitude of the pump-probe ground-state depletion signal, as in figure 5.9. Bottom: Plots of $\mathcal{L}(\omega)$ for the two components observed in ODPS and their sum, $\mathcal{M}(\omega)$ (thick curve). The model parameters are provided in table 5.1 120

- 5.12 Expanded view of the rapidly damped oscillation observed in the dynamic-absorption transient from B820 in OG (see figure 5.10) superimposed with a model defined by the sum of two independent log-normal distributions $\mathcal{L}(\omega)$ of damped cosinusoids, each defined by equation 5.2. The scaling of the ordinate is relative to the magnitude of the pump-probe ground-state depletion signal, as in figure 5.10. Bottom: Plots of $\mathcal{L}(\omega)$ for the two components observed in OG and their sum, $\mathcal{M}(\omega)$ (thick curve). The model parameters are provided in table 5.1 121
- 5.13 Space-filling (CPK) representation of the BChl dimer in the B820 subunit from LH1 based on the calculations of Schulten and coworkers 125
- 5.14 Model of the BChl dimer in the B820 subunit from LH1 based on the calculations of Schulten and coworkers. The polar residues in the vicinity of the dimer are shown as line structures; tryptophan 41, tryptophan 43, tryptophan 48, and tyrosine 41. These residues are possible candidates for the interaction between the π -electron density of the dimer and the protein medium. In order to simplify the figure, the axially coordinated histidines, H32 and H39, are not shown 128
- 5.15 The primary electron donor, P, from the reaction center from *Rhodobacter sphaeroides*. The polar residues in the vicinity of the special pair are shown as line structures; serine 190, serine 205, serine 224, tryptophan 156, asparagine 187, threonine 186, and histidine 168. These residues are possible candidates for the interaction between the π -electron density of the special pair and the protein medium. In order to simplify the figure, the axially coordinated histidines, H173 and H202, are not shown 131

INTRODUCTION

Resonance Raman spectroscopy has been used to examine ground-state and excited-state vibrational dynamics of a variety of complex systems, such as the photosynthetic reaction center. While this technique offers valuable information about the equilibrium geometry and dynamics as well as the electronic structure of the chromophore, it has some limitations. A significant limitation in resonance Raman spectroscopy is that broad low-frequency line shapes arising from inhomogeneously broadened features are not easily discerned from the baseline.

Dynamic absorption spectroscopy, a femtosecond pump-probe, time-domain form of resonance Raman spectroscopy, affords us a spectroscopic tool that is capable of detecting the broad line shapes of the coupled intermolecular modes and distinguishing them from intramolecular modes.

The dissertation is organized as follows:

Chapter 1 begins with a short discussion of charge-transfer reactions in photosynthetic reaction centers and raises the question of the structural origin of the quantum efficiency of natural photosynthesis electron-transfer processes in reaction-center protein complexes. It is followed by a detailed narrative on electron-transfer theory. Finally, the model target systems are presented.

Chapter 2 begins with an explanation of vibrational coherence and wave packet theory. A comparison of experimental techniques used to examine wave packet motions is next. This is followed by a detailed description of the laser system used in the experiments discussed in this dissertation. The chapter concludes with a discussion of

signal processing.

In Chapter 3, the first observations of vibrational coherence in the 10-220-cm⁻¹ region from bacteriochlorophyll *a* in solution will be presented. The distinction between bacteriochlorophyll's *intramolecular* normal modes and *intermolecular* modes between the bacteriochlorophyll and the surrounding solvent will be discussed.

In Chapter 4, the rapidly damped vibrational coherence observed at room temperature in bacteriochlorophyll *a* solutions in pyridine, acetone, 1-propanol and cyclohexane is compared. The results in this chapter show for the first time that intermolecular modes between large electronic chromophores and the surrounding solvent can be resonance-Raman active.

In Chapter 5, the rapidly damped vibrational coherence observed at room temperature in the bacteriochlorophyll-containing proteins B777 and B820 are compared to the vibrational coherence observed in bacteriochlorophyll *a* solutions. The structural origin of the rapidly damped vibrational coherence will be discussed.

CHAPTER 1

INTRODUCTION

1.0 Photosynthetic Reaction Centers

1.0.1 Charge-Transfer Reactions in Photosynthetic Reaction Centers

The work presented in the following chapters is motivated by the persistent question of the structural origin of the quantum efficiency of natural photosynthesis electron-transfer processes in reaction-center protein complexes.¹⁻⁸ The mechanism of the primary charge-separation in the photosynthetic reaction center remains a topic of intense interest despite many years of sustained efforts among several labs.^{1,9,10} Over the last twenty years, covalently linked donor–acceptor supramolecular assemblies¹¹⁻¹⁴ have been synthesized by a number of groups with the intention of emulating some of the photochemical properties of photosynthetic reaction centers. Long-lived charge-separations with relatively high quantum yields have been achieved,¹⁵⁻¹⁷ and some impressive progress has been made in connecting light-harvesting arrays¹⁸⁻²⁰ to charge-separation units to make artificial reaction centers that reproduce the essential features of bacterial photosynthesis.^{21,22}

The artificial systems lack, however, the protein-derived medium that is exploited by the natural photosynthetic reaction centers to obtain an effective irreversibility for the charge-separated states. The protein's folded structure apparently provides more than just a rigid scaffold that holds the donor–acceptor pairs in a favorable geometry. Protein-derived vibrational motions are apparently *coupled* to the forward electron-transfer reactions so that they occur in a nearly *activationless* manner,²³ and it is likely that formation of charge-separated products is accompanied by reorganizational motions of

the protein that resemble in some ways the dynamics of molecular solvents.²⁴⁻²⁸ At present, the role of the solvent medium in the quantum efficiency of synthetic donor acceptor assemblies is a topic of interest.

1.0.2 Structure of the Photosynthetic Reaction Center

The reaction centers found in purple bacteria have been studied extensively.¹⁻⁸ The X-ray crystal structures of the reaction centers of *Rhodoseudomonas viridis* (see figure 1.1) and *Rhodobacter sphaeroides* have been known for almost fifteen years. The redox-active chromophores are arranged along two chromophore branches (L and M), which are related by a pseudo C_2 symmetry axis between the primary electron donor P and the non-heme Fe ion, as shown in figure 1.2. The L and M branches serve as electron acceptors for P. A main interest of current research is focused on understanding of how the initial-electron transfer reactions occur only along the L branch. There is good reason to believe that the protein-derived surroundings of P and of the adjacent monomeric bacteriochlorophyll *a* macrocycles (B_L and B_M), contribute to the breaking of symmetry that results in the charge separation reaction in a given direction. BChl dimers may be favored as primary electron donor structures in reaction centers due to their charge-transfer properties, which might contribute to the high quantum efficiency and spatial directionality of the initial electron-transfer events. Model systems for artificial photosynthesis have been developed by Wasielewski and coworkers that function with a single chlorophyll although not as efficiently as native reaction centers.¹¹

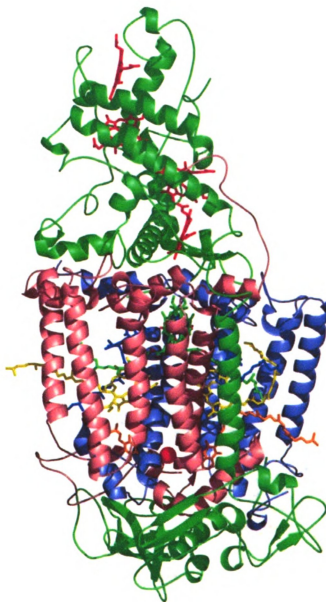


Figure 1.1. The photosynthetic reaction center from *Rhodospseudomonas viridis*,³ rendered from RCSB Protein Data Bank²⁹ file 1ajj. This view shows the topology of the cytochrome (green, top), L (blue), M (pink), and H (green, bottom) subunits.

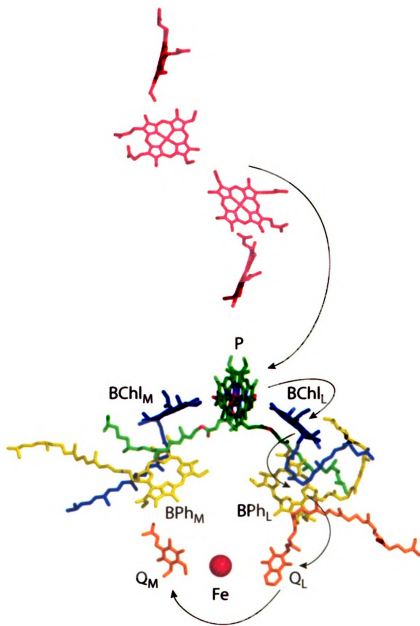


Figure 1.2. Chromophores in the reaction center from *Rhodospseudomonas viridis*.³ The arrows represent the directionality of the electron transfer reactions.

1.1 Electron-Transfer Theory

In the Marcus theory,³⁰⁻³³ the reorganization energy is the free energy required to move the atoms of the donor-acceptor pair, and to some extent those of the intervening medium, so that the structure of the product state is assumed in advance of the instantaneous electron-transfer event (see figure 1.3). The vibrational modes that are said to be coupled to an electron-transfer reaction are thought to be the ones that make significant contribution to this energy. The reorganization energy is traditionally separated into two terms:

$$\lambda = \lambda_i + \lambda_o \quad (1.1)$$

The inner-sphere term, λ_i , is the change in energy associated with the change of structure of the donor and acceptor molecules. The outer-sphere term, λ_o , is the part associated with the change of structure of the solvent medium.²⁹

For donor-acceptor systems in a molecular solvent, the simplest approach for the calculation of the outer-sphere reorganization energy employs dielectric-continuum theory, which treats the solvent as a continuous medium characterized by optical and static dielectric constants ϵ_o and ϵ_s :

$$\lambda_o = (\Delta q)^2 \left(\frac{1}{\epsilon_o} - \frac{1}{\epsilon_s} \right) \left(\frac{1}{2a_1} + \frac{1}{2a_2} - \frac{1}{R} \right) \quad (1.2)$$

Here the solvent forms a cavity of radius a_1 and a_2 around the donor and acceptor, respectively; Δq is the charge transferred, and R is the distance from the donor to the acceptor.³⁴ There are problems with using such a picture to treat long-distance electron-transfer reactions in a protein. A protein's folded structure presents a discontinuous, heterogeneous medium of varying polarizability,³⁵ and there is reason to suspect that the

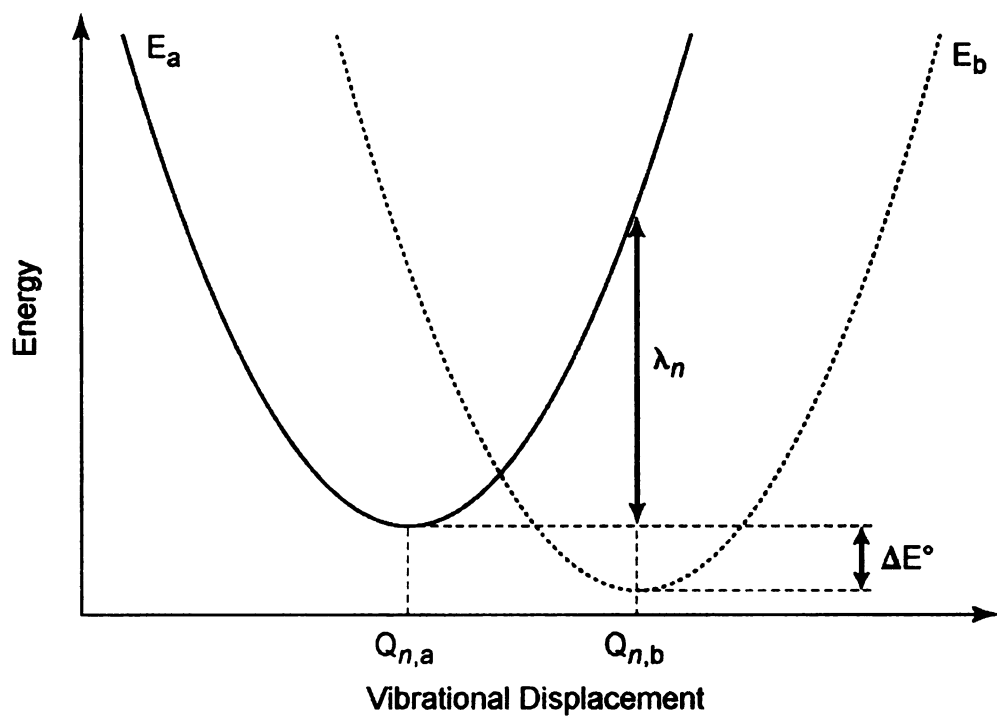


Figure 1.3. Diabatic harmonic potential-energy curves for the reactant (E_a) and product (E_b) of an electron-transfer reaction as a function of the displacement of one of the normal modes of vibration n ; λ_n marks the mode-specific reorganization energy, and $-\Delta E^\circ$ is the driving force.

bridge between the donor and acceptor is through bonded and hydrogen-bonded pathways rather than just through space.³⁶⁻⁴³ An opposing view from Dutton and coworkers^{44,45} holds that long-distance electron transfer in proteins occurs through a homogeneous barrier that is not necessarily directed through covalent pathways. Recent work by the Winkler/Gray group supports the former view in that electron transfer through bonded linkages over a given distance was shown to be much faster than through nonbonding interactions.⁴⁶

The magnitude of the reorganization energy plays an important role in determining the rate of an electron-transfer reaction.³² For non-adiabatic electron transfer in the high-temperature limit, where the relevant normal modes of vibration can be treated classically, the reorganization energy and the driving force, $-\Delta G^0$, control the magnitude of the Gibbs free energy of activation, ΔG^*

$$\Delta G^* = (\lambda + \Delta G^0)^2 / 4\lambda \quad (1.3)$$

For a spontaneous reaction, the driving force is the negative of the Gibbs free-energy difference between the product and reactant states at their respective equilibrium geometries; spontaneous reactions ($\Delta G^0 < 0$) have *positive* driving forces. The expression for the rate constant,

$$k = \frac{2\pi}{\hbar} \frac{V_{DA}^2}{(4\pi\lambda k_B T)^{1/2}} \exp\left(-\Delta G^* / k_B T\right) \quad (1.4)$$

includes in the pre-exponential term an electronic donor-acceptor coupling factor, V_{DA} , which describes the spatial overlap of the electron density from the donor and acceptor at

the geometry of the transition state. Note that the preexponential and exponential terms contain factors of $\lambda^{-1/2}$ and λ^{-1} , respectively, so one would predict that the highest electron-transfer rates are obtained when λ is minimized, say, by constructing a rigid donor–acceptor system and by running the reaction in a non-polar medium. For spontaneous reactions, however, the rate constants magnitude is sensitively controlled by how well the driving force is matched to the reorganization energy. The usual expectation that the rate constant should increase as the driving force increases corresponds to the *normal regime* of the Marcus theory ($-\Delta G^0 < \lambda$). The maximum rate occurs when $-\Delta G^0 = \lambda$, the condition that produces *activationless* kinetics ($\Delta G^* \approx 0$). The *inverted regime*, where the rate constant *decreases* as the driving force increases, is encountered as the driving force is increased past the matching condition ($-\Delta G^0 > \lambda$).⁴⁷

1.2 Coupled Modes in Photosynthesis

The reaction centers from purple bacteria exhibit a set of redox-active chromophores and surrounding protein structures that apparently optimize the reorganization energy and driving forces for each electron-transfer step so that the reactions exhibit a temperature-independent or weakly temperature-dependent profile.⁴⁸ Vibrational modes derived from the protein medium in the 80–120-cm⁻¹ regime^{23,48-51} are apparently coupled in *each* step even though a broad range of time scales, a range of intervening protein structures, and several types of cofactors are involved, as can be seen in figures 1.1 and 1.2:

1. the reduction of the bacteriochlorophyll dimer (special pair) primary electron donor, P, by the cytochrome subunit,⁵²

2. the light-driven primary electron-transfer step from P to the bacteriopheophytin acceptor, BPh_L⁵³⁻⁵⁶
3. the secondary electron transfer from BPh_L to the quinone Q_a.⁵⁷⁻⁵⁹

The first and third reactions are ground-state reactions involving relatively slow electron transfers over long distances. In contrast, the second reaction listed above is a light-initiated, excited-state reaction that occurs so rapidly ($\tau \approx 3\text{ps}$) that reactants may not be vibrationally equilibrated,^{55,56} so the temperature dependence is not as easily interpreted. Experimental evidence from studies of electron-transfer in photosynthetic reaction centers strongly support the claim that low-frequency modes, in the 100-cm^{-1} regime, are associated with the reaction coordinate. Small and coworkers showed that a Franck-Condon progression along low-frequency normal-mode coordinates accounts for a substantial fraction of the optical reorganization energy using photochemical hole-burning spectroscopy at cryogenic temperatures.^{53,54} Vos, Martin and coworkers observed vibrational wave packet motion in pump-probe transients from reaction center preparations⁶⁰⁻⁶⁴ using femtosecond pump-probe spectroscopy. The work detected several low frequency modes under 160 cm^{-1} .^{60,62,63,65,66} Similar low-frequency modes were observed by Stanley and Boxer⁶⁷ in modulations of the spontaneous fluorescence from P*. The damping time for wave-packet motion is comparable to the electron-transfer time scale,⁶⁰ so the possibility that the active modes are coupled to the electron-transfer reaction coordinate has been raised by Vos et al.,⁶⁸ Shuvalov and coworkers,⁶⁹⁻⁷² and Zinth and coworkers.^{73,74}

1.3 Assignments for the Coupled Modes

Vos, Martin, and coworkers detected several active modes in the vibrational coherence from the stimulated emission from P*. The strongest features were observed in the 90-160-cm⁻¹ range.⁷⁵ The lowest frequencies (10–30 cm⁻¹) in the observed set were assigned to *collective* protein-derived motions.⁶⁰ This suggestion was made in consideration of the peak observed in the 50-cm⁻¹ region of the vibrational density of states obtained from molecular dynamics simulations in small proteins;⁷⁶ a similar feature is observed in non-resonant Raman spectra from small protein crystals.⁷⁷ Small and coworkers assigned the 30-cm⁻¹ modes they detected in hole-burning experiments to protein phonons.^{53,54}

Vos, Martin, and coworkers then showed that the vibrational coherence from P* exhibits frequency shifts and intensity changes in response to a range of point mutations that alter the hydrogen-bonding pattern between the pair of bacteriochlorophyll (BChl) macrocycles and the surrounding protein subunits.⁷⁸ The active modes in the 90–160-cm⁻¹ range were assigned not to the BChl macrocycles themselves but to the protein structure itself because mutations that affected the electronic configuration of P did not cause frequency shifts.^{75,78} This conclusion was supported by Struve *et al.*⁷⁵ and Chachisvilis and coworkers;⁷⁶ both reporting that BChl *in solution* does not exhibit vibrational coherence.

These results lead us to suggest that the coupled modes arise from *intermolecular* modes between the chromophores and the surrounding protein medium rather than involving collective motions of the bridging protein between the donor and acceptor. A

tuning of the electronic properties of the embedded chromophores through predominantly solvatochromic effects would be mediated by these modes, which would resemble those between a chromophore and its *clustered* solvent molecules. A change in the electron configuration of the donor or acceptor might be expected to displace weak, formally non-bonding interactions with protein-derived groups such as hydrogen bonds, polar solvent (dipole–dipole) interactions, or perhaps even non-polar solvent (London dispersion) interactions. These interactions are known to exhibit frequencies in the right range to be the coupled modes whose frequencies were identified experimentally. In molecular liquids, intermolecular mode frequencies detected in nonresonant optical Kerr effect experiments lie in the 10–200-cm⁻¹ range;⁷⁹ collective motions of liquids are noted in the 10-cm⁻¹ regime,⁸⁰ but pair-wise interactions are found in the 60–100-cm⁻¹ range.⁸¹

1.4 Resonance Raman Activity in Intermolecular Modes

Electron-transfer reactions coupled to protein–chromophore intermolecular modes would be mediated by a partial delocalization of the chromophores electron density onto the protein-derived group. Therefore, it is probable that the relevant modes would be active in the resonance Raman spectrum. Mathies and coworkers are among the few to detect intermolecular modes in condensed phases using resonance Raman spectroscopy in the frequency domain. Resonance-Raman active modes were detected from alcohol⁸² and water⁸³ solutions of the solvated electron. The solvated electron is a diffuse structure that makes a significant ground-to-excited-state change in size and shape;⁸⁴⁻⁸⁸ it apparently interacts strongly enough with a number of solvent molecules in the first shell that the absorption transition is vibronically coupled to a number of solvent intramolecular

modes.^{82,83} The lowest frequency Raman-active modes observed in water, at 110 cm^{-1} , are the intermolecular hindered translational modes between the electron and molecules in the first solvation shell.⁸³

In contrast, Waterland and Kelley⁸⁹ did not observe features from intermolecular modes in their UV resonance Raman studies of the nitrate ion in several solvents, perhaps because the π -electron density of the nitrate ion is highly localized. Barbara and coworkers⁹⁰ noted significant solvent dependences in the intervalence charge-transfer rate and in the damping of the ground-state vibrational coherence in the femtosecond pump-probe studies of the cyanide-bridged Ru(II,III) mixed-valence complex, but no solvent-dependent components were directly observed. As in the case of the nitration ion, a highly localized π -electron density is probably responsible for the lack of detection of intermolecular modes.

Chromophores with spatially delocalized π -electron density owing to conjugation are much more likely to exhibit vibronic coupling to intermolecular modes. We suggest that time-domain resonance Raman methods, such as the pump-probe method called *dynamic absorption spectroscopy* that was described by Shank, Mathies and coworkers,⁹¹⁻⁹⁵ are very likely to be successful in the study of intermolecular modes in delocalized π -electron systems. In the frequency domain, broad low-frequency line shapes arising from inhomogeneously broadened features are not easily discerned from the baseline. In the time domain, however, the same line shapes result in sharp, rapidly damped features in the vibrational coherence, and the broad line shapes can be resolved into components on the basis of their distinct phases. Resonance Raman activity should be exhibited by intermolecular chromophore-protein or chromophore-solvent modes that are displaced

owing to the transitions of the chromophore; similar mode displacements would be activated by electron-transfer reactions since the redox-active electrons are associated with the frontier highest-occupied and lowest-unoccupied molecular orbitals.

1.5 Research Design

In the preceding narrative, we have raised the hypothesis that electron-transfer reactions in condensed phases and in the photosynthetic reaction center are coupled to intermolecular vibrational modes between the redox-active chromophores and the clustered solvent molecules in the first solvation shell. We focus the content of this thesis on understanding the structural origin of the vibrational coherence from the special pair, P, in the photosynthetic reaction center. We test the hypothesis that at least some of the components in the vibrational coherence arise from intermolecular modes between the BChl macrocycles in P and the surrounding protein medium. Our approach is to start with monomeric bacteriochlorophyll in solution, to determine whether the clustered solvent molecules in the first solvation shell contribute to the vibrational coherence. We then progress to a consideration of the vibrational coherence in BChl-containing proteins, B820 and B777. Here, we focus exclusively on how the protein structure of B820 impacts the character of the low-frequency vibrational coherence. We compare the vibrational coherence of the monomeric B777 system, which exposes the BChl macrocycle to the surrounding detergent environment, to that of the B820 system, where the BChl macrocycles are essentially completely protected from the surrounding solvent by the protein structure.

1.6 References

- (1) Parson, W. W. In *Photosynthesis (New Comprehensive Biochemistry, Volume 15)*; Amesz, J., Ed.; Elsevier: New York, 1987, p 43–61.
- (2) Deisenhofer, J.; Epp, O.; Miki, K.; Huber, R.; Michel, H. *J. Mol. Biol.* **1984**, *180*, 385–398.
- (3) Deisenhofer, J.; Epp, O.; Miki, K.; Huber, R.; Michel, H. *Nature* **1985**, *318*, 618–624.
- (4) Allen, J. P.; Feher, G.; Yeates, T. O.; Rees, D. C.; Deisenhofer, J.; Michel, H.; Huber, R. *Proc. Natl. Acad. Sci. USA* **1986**, *83*, 8589–8593.
- (5) Allen, J. P.; Feher, G.; Yeates, T. O.; Komiya, H.; Rees, D. C. *Proc. Natl. Acad. Sci. USA* **1987**, *84*, 5730–5734.
- (6) Rhee, K.-H.; Morris, E. P.; Barber, J.; Kühlbrandt, W. *Nature* **1998**, *396*, 283–286.
- (7) Zouni, A.; Witt, H.-T.; Kern, J.; Fromme, P.; Krauß, N.; Saenger, W.; Orth, P. *Nature* **2001**, *409*, 739–742.
- (8) Jordan, P.; Fromme, P.; Witt, H. T.; Klukas, O.; Saenger, W.; Krauß, N. *Nature* **2001**, *411*, 909–917.
- (9) Boxer, S. G.; Goldstein, R. A.; Lockhart, D. J.; Middendorf, T. R.; Takiff, L. *J. Phys. Chem.* **1989**, *93*, 8280–8294.
- (10) Friesner, R. A.; Won, Y. *Biochim. Biophys. Acta* **1989**, *977*, 99–122.
- (11) Wasielewski, M. R. *Chem. Rev.* **1992**, *92*, 436–461.
- (12) Wasielewski, M. R.; Wiederrecht, G. P.; Svec, W. a.; Niemczyk, M. P. *Solar Energy Mat. Solar Cells* **1995**, *38*, 127–134.
- (13) Redmore, N. P.; Rubtsov, I. V.; Therien, M. J. *J. Am. Chem. Soc.* **2003**, *125*, 8769–8778.
- (14) Splan, K. E.; Stern, C. L.; Hupp, J. T. *Inorg. Chim. Acta* **2004**, *357*, 4005–4014.
- (15) Gust, D.; Moore, T. A.; Makings, L. R.; Liddell, P. A.; Nemeth, G. A.; Moore, A. L. *J. Am. Chem. Soc.* **1986**, *108*, 8028–8031.

- (16) Gust, D.; Moore, T. A. *Science* **1989**, *244*, 35–141.
- (17) Gust, D.; Moore, T. A.; Moore, A. L.; Lee, S.-J.; Bittersmann, E.; Luttrull, D. K.; Rehms, A. A.; DeGaraziano, J. M.; Ma, X. C.; Gao, F.; Belford, R. E.; Trier, T. T. *Science* **1990**, *248*, 199–201.
- (18) Prathapan, S.; Johnson, T. E.; Lindsey, J. S. *J. Am. Chem. Soc.* **1993**, *115*, 7519–7520.
- (19) Hsiao, J.-S.; Krueger, B. P.; Wagner, R. W.; Johnson, T. E.; Delayen, J. K.; Mauzerall, D. C.; Fleming, G. R.; Lindsey, J. S.; Bocian, D. F.; Donohoe, R. J. *J. Am. Chem. Soc.* **1996**, *118*, 11181–11193.
- (20) Loewe, R. S.; Lammi, R. K.; Diers, J. R.; Kirmaier, C.; Bocian, D. F.; Holten, D.; Lindsey, J. S. *J. Mater. Chem.* **2002**, *12*, 1530–1552.
- (21) Stenberg-Yfrach, G.; Rigaud, J.-L.; Durantini, E. N.; Moore, A. L.; Gust, D.; Moore, T. A. *Nature* **1998**, *392*, 479–482.
- (22) Gust, D.; Moore, T. A.; Moore, A. L. *Acc. Chem. Res* **2001**, *34*, 40–48.
- (23) Bixon, M.; Jortner, J. *J. Phys. Chem.* **1986**, *90*, 3795–3800.
- (24) Maroncelli, M.; MacInnis, J.; Fleming, G. R. *Science* **1989**, *243*, 1674–1681.
- (25) Simon, J. D. *Pure Appl. Chem.* **1990**, *62*, 2243–2250.
- (26) Barbara, P. F.; Walker, G. C.; Smith, T. P. *Science* **1992**, *256*, 975–981.
- (27) Stratt, R. M.; Maroncelli, M. *J. Phys. Chem.* **1996**, *100*, 12981–12996.
- (28) Lampa-Pastirk, S.; Beck, W. F. *J. Phys. Chem. B* **2004**, *108*, 16288–16294.
- (29) Berman, H. M.; Westbrook, J.; Feng, Z.; Gilliland, G.; Bhat, T. N.; Weissig, H.; Shindyalov, I. N.; Bourne, P. E. *Nucl. Acids Res.* **2000**, *28*, 235–242.
- (30) Marcus, R. A. *J. Chem. Phys.* **1956**, *24*, 966–989.
- (31) Marcus, R. A. *J. Chem. Phys.* **1965**, *43*, 679–701.
- (32) Marcus, R. A.; Sutin, N. *Biochim. Biophys. Acta* **1985**, *811*, 265–322.
- (33) Marcus, R. A. *Isr. J. Chem.* **1988**, *28*, 205–213.
- (34) Walker, G. C.; Beratan, D. N. In *Encyclopedia of Chemical Physics and Physical Chemistry*; Moore, J. H., Spencer, N. D., Eds.; Institute of Physics

Publishing: Bristol, England, 2001, p 2657–2680.

- (35) Cohen, B. E.; McAnaney, T. B.; Park, E. S.; Jan, Y. N.; Boxer, S. G.; Jan, L. Y. *Science* **2002**, *296*, 1700–1703.
- (36) Beratan, D. N.; Onuchic, J. N.; Hopfield, J. J. *J. Chem. Phys.* **1987**, *86*, 4488–4498.
- (37) Onuchic, J. N.; Beratan, D. N. *J. Chem. Phys.* **1990**, *92*, 722–733.
- (38) Beratan, D. N.; Onuchic, J. N.; Betts, J. N.; Bowler, B. E.; Gray, H. B. *J. Am. Chem. Soc.* **1990**, *112*, 7915–7921.
- (39) Onuchic, J. N.; de Andrade, P. C. P.; Beratan, D. N. *J. Chem. Phys.* **1991**, *95*, 1131.
- (40) Betts, J. N.; Beratan, D. N.; Onuchic, J. N. *J. Am. Chem. Soc.* **1992**, *114*, 4043–4046.
- (41) Beratan, D. N.; Betts, J. N.; Onuchic, J. N. *J. Am. Chem. Soc.* **1992**, *96*, 2852–2855.
- (42) Schulten, K. *Science* **2000**, *290*, 61–62.
- (43) Balabin, I. A.; Onuchic, J. N. *Science* **2000**, *290*, 114–117.
- (44) Moser, C. C.; Keske, J. M.; Warncke, K.; Farid, R. S.; Dutton, P. L. *Nature* **1992**, *355*, 796–802.
- (45) Page, C. C.; Moser, C. C.; Chen, X.; Dutton, P. L. *Nature* **1999**, *402*, 47–52.
- (46) Wenger, O. S.; Leigh, B. S.; Villahermosa, R. M.; Gray, H. B.; Winkler, J. R. *Science* **2005**, *307*, 99–102.
- (47) Closs, G. L.; Miller, J. R. *Science* **1988**, *240*, 440–447.
- (48) Bixon, M.; Jortner, J. *Chem. Phys. Lett.* **1989**, *159*, 17–20.
- (49) Kirmaier, C.; Holten, D.; Parson, W. W. *Biochim. Biophys. Acta* **1985**, *810*, 33–48.
- (50) Fleming, G. R.; Martin, J.-L.; Breton, J. *Nature* **1988**, *333*, 190–192.
- (51) Breton, J.; Martin, J.-L.; Fleming, G. R.; Lambry, J.-C. *Biochemistry* **1988**, *27*, 8276.

- (52) Hopfield, J. J. *Proc Natl Acad Sci U S A* **1974**, *71*, 3640.
- (53) Johnson, S. G.; Tang, D.; Jankowiak, R.; Hayes, J. M.; Small, G. J.; Tiede, D. *M. J. Phys. Chem.* **1990**, *94*, 5849–5855.
- (54) Johnson, S. G.; Tang, D.; Jankowiak, R.; Hayes, J. M.; Small, G. H. *J. Phys. Chem.* **1989**, *93*, 5953–5957.
- (55) Lin, S.; Taguchi, A. K. W.; Woodbury, N. W. *J. Phys. Chem.* **1996**, *100*, 17067–17078.
- (56) Haffa, A. L. M.; Lin, S.; Katilius, E.; Williams, J. C.; Taguchi, A. K. W.; Allen, J. P.; Woodbury, N. W. *J. Phys. Chem. B.* **2002**, *106*, 7376–7384.
- (57) Gunner, M. R.; Robertson, D. E.; Dutton, P. L. *J. Phys. Chem.* **1986**, *90*, 3783–3795.
- (58) Gunner, M. R.; Dutton, P. L. *J. Am. Chem. Soc.* **1989**, *111*, 3400–3412.
- (59) Feher, G.; Okamura, M.; Kleinfeld, D. In *Protein Structure: Molecular and Electronic Reactivity*; Austin, R., Buhks, E., Chance, B., De Vault, D., Dutton, P. L., Frauenfelder, H., Gol'danskii, V., Eds.; Springer-Verlag: New York, 1987, p 399–421.
- (60) Vos, M. H.; Rappaport, F.; Lambry, J.-C.; Breton, J.; Martin, J.-L. *Nature* **1993**, *363*, 320–325.
- (61) Vos, M. H.; Jones, M. R.; Breton, J.; Lambry, J.-C.; Martin, J.-L. *Biochemistry* **1996**, *35*, 2687–2692.
- (62) Vos, M. H.; Jones, M. R.; Hunter, C. N.; Breton, J.; Lambry, J.-C.; Martin, J.-L. *Biochemistry* **1994**, *33*, 6750–6757.
- (63) Vos, M. H.; Jones, M. R.; Hunter, C. N.; Breton, J.; Martin, J.-L. *Proc. Nat. Acad. Sci. USA* **1994**, *91*, 12701–12705.
- (64) Vos, M. H.; Jones, M. R.; McGlynn, P.; Hunter, C. N.; Breton, J.; Martin, J.-L. *Biochim. Biophys. Acta* **1994**, *1186*, 117–122.
- (65) Vos, M. H.; Lambry, J. C.; Robles, S. J.; Youvan, D. C.; Breton, J.; Martin, J. L. *Proc Natl Acad Sci U S A* **1991**, *88*, 8885–8889.
- (66) Vos, M. H.; Lambry, J. C.; Robles, S. J.; Youvan, D. C.; Breton, J.; Martin, J. L. *Proc. Nat. Acad. Sci. USA* **1992**, *89*, 613–617.
- (67) Stanley, R. J.; Boxer, S. G. *J. Phys. Chem.* **1995**, *99*, 859–863.

- (68) Vos, M. H.; Jones, M. R.; Martin, J. L. *Chem. Phys.* **1998**, *233*, 179–190.
- (69) Yakovlev, A.; Shkuropatov, A.; Shuvalov, V. *FEBS Lett.* **2000**, *466*, 209–212.
- (70) Yakovlev, A.; Shkuropatov, A.; Shuvalov, V. *Biochemistry* **2002**, *41*, 2667–2674.
- (71) Yakovlev, A.; Shkuropatov, A.; Shuvalov, V. *Biochemistry* **2002**, *41*, 14019–14027.
- (72) Shuvalov, V.; Yakovlev, A. *FEBS Lett.* **2003**, *540*, 26–34.
- (73) Spörlein, S.; Zinth, W.; Wachtveitl, J. *J. Phys. Chem. B* **1998**, *102*, 7492–7496.
- (74) Huppmann, P.; Spörlein, S.; Bibikova, M.; Oesterhelt, D.; Wachtveitl, J.; Zinth, W. *J. Phys. Chem. A* **2003**, *107*, 8302–8309.
- (75) Vos, M. H.; Martin, J.-L. *Biochim. Biophys. Acta* **1999**, *1411*, 1–20.
- (76) Brooks III, C. L.; Karplus, M.; Pettitt, B. M. *Proteins: a Theoretical Perspective of Dynamics, Structure, and Thermodynamics*; John Wiley and Sons: New York, 1988.
- (77) Peticolas, W. L. *Meth. Enzymol.* **1978**, *61*, 425–458.
- (78) Rischel, C.; Spiedel, D.; Ridge, J. P.; Jones, M. R.; Breton, J.; Lambry, J.-C.; Martin, J.-L.; Vos, M. H. *Proc. Natl. Acad. Sci. USA* **1998**, *95*, 12306–12311.
- (79) Lotshaw, W. T.; McMorrow, D.; Thantu, N.; Melinger, J. S.; Kitchenbaum, R. *J. Raman Spect.* **1995**, *26*, 571–583.
- (80) McMorrow, D.; Lotshaw, W. T. *Chem. Phys. Lett.* **1993**, *201*, 369–376.
- (81) McMorrow, D.; Lotshaw, W. T. *J. Phys. Chem.* **1991**, *95*, 10395–10406.
- (82) Tauber, M. J.; Stuart, C. M.; Mathies, R. A. *J. Am. Chem. Soc.* **2004**, *126*, 3414–3415.
- (83) Tauber, M. J.; Mathies, R. A. *Chem. Phys. Lett.* **2002**, *354*, 518–526.
- (84) Alfano, J. C.; Walhout, P. K.; Kimura, Y.; Barbara, P. F. *J. Chem. Phys.* **1993**, *98*, 5996–5998.
- (85) Kimura, Y.; Alfano, J. C.; Walhout, P. K.; Barbara, P. F. *J. Phys. Chem.* **1994**, *98*, 3450–3458.

- (86) Reid, P. J.; Silva, C.; Walhout, P. K.; Barbara, P. F. *Chem. Phys. Lett.* **1994**, *228*, 658–664.
- (87) Walhout, P. K.; Alfano, J. C.; Kimura, Y.; Silva, C.; Reid, P. J.; Barbara, P. F. *Chem. Phys. Lett.* **1995**, *232*, 135–140.
- (88) Silva, C.; Walhout, P. K.; Reid, P. J.; Barbara, P. F. *J. Phys. Chem. A* **1998**, *102*, 5701–5707.
- (89) Waterland, M.; Myers Kelley, A. *J. Chem. Phys.* **2000**, *113*, 6760–6773.
- (90) Kambhampati, P.; Son, D. H.; Kee, T. W.; Barbara, P. F. *J. Phys. Chem. A* **2000**, *104*, 10637–10644.
- (91) Fragnito, H. L.; Bigot, J.-Y.; Becker, P. C.; Shank, C. V. *Chem. Phys. Lett.* **1989**, *160*, 101–104.
- (92) Pollard, W. T.; Dexheimer, S. L.; Wang, Q.; Peteanu, L. A.; Shank, C. V.; Mathies, R. A. *J. Phys. Chem.* **1992**, *96*, 6147–6158.
- (93) Peteanu, L. A.; Schoenlein, R. W.; Wang, Q.; Mathies, R. A.; Shank, C. V. *Proc. Natl. Acad. Sci. USA* **1993**, *90*, 11762–11766.
- (94) Schoenlein, R. W.; Peteanu, L. A.; Wang, Q.; Mathies, R. A.; Shank, C. V. *J. Phys. Chem.* **1993**, *97*, 12087–12092.
- (95) Wang, Q.; Schoenlein, R. W.; Peteanu, L. A.; Mathies, R. A.; Shank, C. V. *Science* **1994**, *266*, 422–424.

CHAPTER 2

THEORY AND EXPERIMENTAL METHODS FOR THE STUDY OF VIBRATIONAL COHERENCE

2.0 Introduction

As reviewed in Chapter 1, it is likely that low-frequency vibrational modes play an important role in the electron-transfer reactions in photosynthesis.¹⁻² Several groups have employed ultrafast pump-probe methods to characterize vibrational coherence from a variety of systems including the photosynthetic reaction center.²⁻⁶ In the following, we discuss the theory and experimental techniques necessary to test the hypothesis discussed in Chapter 1.

2.1 Theory

2.1.1 Wave Packets

In the following, we describe a classical description, based on the Franck-Condon principle, on vibrational wave packets following the treatment of Lee and Heller.⁸⁻¹⁰ Wave packets have been described quantum mechanically as well as classically; however, the classical description is easier to visualize conceptually.

As introduced in the previous chapter, the BChl-containing target systems exhibit strong absorption bands in the visible and UV that are assigned to a $\pi \rightarrow \pi^*$ transition. The movement of an electron from a bonding orbital to an antibonding orbital results in the lengthening of one or more bonds in the excited state, causing the equilibrium structure of the excited state to be displaced from that of the ground state. This structural change offsets horizontally the excited-state surface from that of the ground-state surface,

as illustrated in figure 2.1.

An excited-state wave packet originates when an ensemble of molecules in the sample interact with the pump field from the incident light. The interaction vertically transfers the equilibrium probability density from the ground-state to the excited-state surface in the form of a localized wave packet ($t=1$ in figure 2.1). The wave packet is acted upon by the forces of the excited-state potential surface. This gives rise to a moving wave-packet ($t=3$); the wave packet moves towards the new equilibrium position in an attempt to minimize its energy with respect to the excited-state geometry.

A second interaction with the pump field transfers part of the excited-state wave packet back to the ground-state potential surface. Because the wave packet was displaced in the excited state, it is no longer at equilibrium with respect to the ground-state geometry. This creates a ground-state wave packet that evolves in time according to the forces arising from the ground-state potential-energy surface ($t=3$). The formation of the ground-state wave packet is also known as resonant impulsive stimulated Raman scattering, or RISRS.⁷

2.1.2 Resonance Raman Spectroscopy

Raman spectroscopy can be used to examine ground-state and excited-state vibrational dynamics of complex systems. The vibrational frequencies give specific information about geometry and electronic structure of the chromophore in the ground state, while the intensities of resonance Raman lines give information about the symmetry, equilibrium geometry, and dynamics of the chromophore in the excited state.¹¹ Work by Mathies and coworkers¹¹ established the use of resonance Raman intensities to obtain information on the reaction dynamics of P in the bacterial reaction center. The Lee

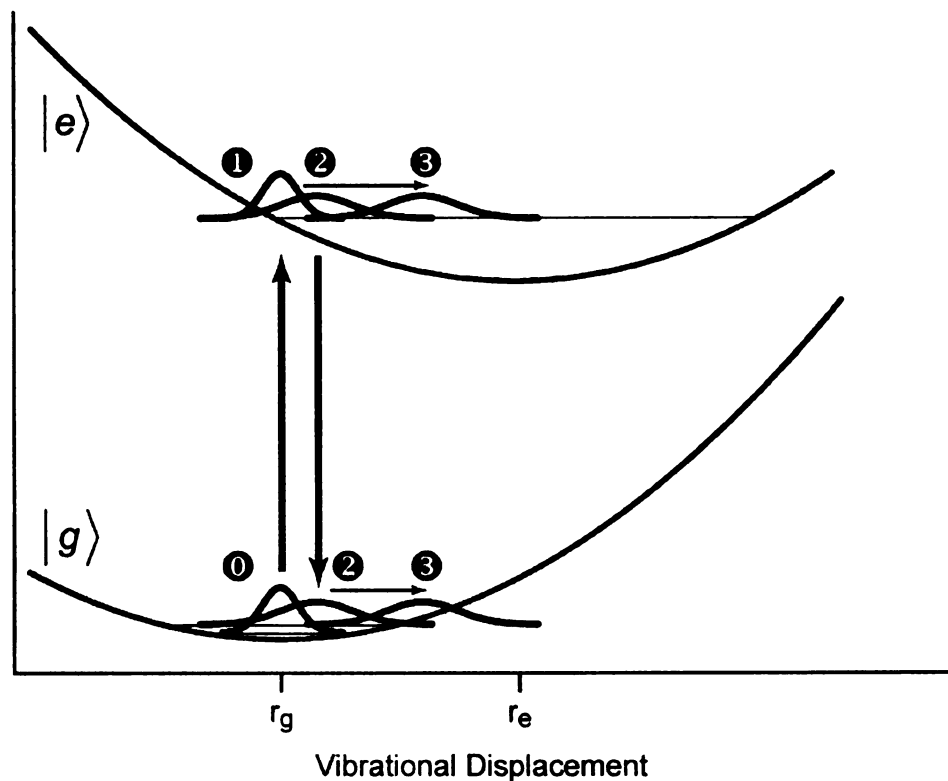


Figure 2.1. Excited-state and ground-state coherent wave-packet motion in the dynamic absorption experiment. The excited-state and ground-state potential-energy surfaces are drawn as parabolas that are displaced with respect to a generalized multimode coordinate; r_g and r_e mark the equilibrium ground-state and excited-state geometries, respectively. Thick arrows represent the resonant pump-laser field; thin arrows show the direction that the wave packets evolve during the first passage on the two surfaces. The numbers indicate event times, starting with ground-state probability density, creation of the excited-state wave packet by the pump field, creation of the ground-state wave packet by the pump field, and evolution during the first vibration.

and Heller wave packet picture discussed above^{9,10,12,13} describes resonance Raman intensity as the time-dependent spatial overlap of the excited-state wave packet prepared by the absorption of a photon with the final wave packet prepared on the ground-state surface following spontaneous emission of a photon. The intensity of the overlap integral is governed by the time evolution of the wave packet on the excited-state surface before the transition to the ground state.¹¹

Ground-state and excited-state vibrational coherences in pump-probe experiments arise from structural displacement of the excited-state and the ground-state surface along normal coordinate modes.¹⁴⁻¹⁷ The same modulation components and frequencies would be expected from the excited-state and ground-state wave packets for a bound electronic state with a comparable surface shape as the ground-state. If an excited-state wave packet moves away from the Franck-Condon region and crosses to a product state surface, new modulation frequencies might be observed. In this case, the Franck-Condon active modes can promote a crossing to the product-state surface.¹⁸

2.1.3 Dynamic-Absorption Spectroscopy

Shank, Mathies and co-workers^{1,19-26} showed more than ten years ago that resonant impulsive excitation of large electronic chromophores in condensed phases and in proteins results in a nonstationary absorption/stimulated-emission spectrum. When monitored with a short, delayed probe pulse that is resonant with the ground-state absorption spectrum, the intensity of the transmitted probe light is modulated at the normal-mode frequencies that would appear in the resonance Raman spectrum. If the probe pulse is resonant with the stimulated-emission spectrum, the modulation frequencies are those of the excited electronic state. This so-called *dynamic-absorption*

spectroscopy was described by Pollard and Mathies¹⁴⁻¹⁷ in terms of coherent motion of vibronic wave packets (vibrational coherence) on the resonant electronic excited-state and ground-state potential-energy surfaces, the latter produced by stimulated-Raman transitions.

As discussed by Pollard and Mathies,¹⁷ most of the prior literature on the pump-probe absorption technique treated the probe pulse as being monochromatic. The absorbance of the sample at the probe wavelength is measured in terms of the loss of energy of the transmitted probe pulse. Since the absorbance of the sample is averaged over the actual probe pulse spectrum, the measured spectra are broadened by the spectral width of the pulses. Alternatively, dynamic-absorption spectroscopy directly monitors the spectrum of the probe pulse resulting in high resolution in both the time and frequency domains.^{16,17} The transmitted probe beam is spectrally dispersed onto a detector after passing through the sample. The transient absorption spectrum of a sample is obtained by measuring how the spectrum of the probe pulse is changed by transmission through the sample.¹⁷ The pump-probe signal is displayed as the ratio of the intensity of the probe pulse in the presence and absence of the pump pulse.

2.1.4 Frequency Domain vs. Time Domain

The main limitation of resonance Raman spectroscopy is that low-frequency modes are difficult to detect due to Rayleigh scattering at the excitation wavelength. Whereas dynamic-absorption spectroscopy is not affected by Rayleigh scattering, low-frequency vibrational modes can easily be detected, as long as the time record of the data is of sufficient length. Higher frequency modes are obtained easier through resonance Raman

spectroscopy. The frequency information returned from dynamic-absorption spectroscopy is affected by the pulse duration. In order to observe wave-packet motion at a given frequency, the excitation pulse has to be much shorter than the vibrational period. This means that the duration of the pulses used can be adjusted to prevent the observation of higher frequency modes, if one is only interested in the low-frequency vibrational modes of a system.

2.2 Experimental: Femtosecond Pump-Probe Spectrometer Design and Characterization

Dynamic-absorption experiments were performed with the femtosecond pump-probe spectrometer described in the following sections. The spectrometer consists of a femtosecond ti:sapphire oscillator, a prism pair pulse compressor, and a rapid-scanning Mach-Zehnder interferometer. The construction of the ti:sapphire oscillator and the design of the rapid-scanning Mach-Zehnder interferometer will be discussed in sequence. An early version of the spectrometer was discussed previously,^{27,28} and the current version was described in more recent manuscripts.^{29,30}

2.2.1 Ti:Sapphire Oscillator

The oscillator shown in figure 2.2 is a Mira Optima 900-F obtained from Coherent. The oscillator utilizes titanium sapphire as the gain medium and is equipped with X-wave broad-tuning-range cavity optics, allowing for wide tunability from 700 nm to 980 nm. The oscillator is pumped by a Verdi (Coherent) 5-W laser. The output pulses were used at the natural pulse-repetition rate (75 MHz). Figure 2.3 shows the output spectrum obtained from the mode-locked oscillator. This spectral bandwidth results in 60-fs (sech^2) pulses shown in figure 2.4.

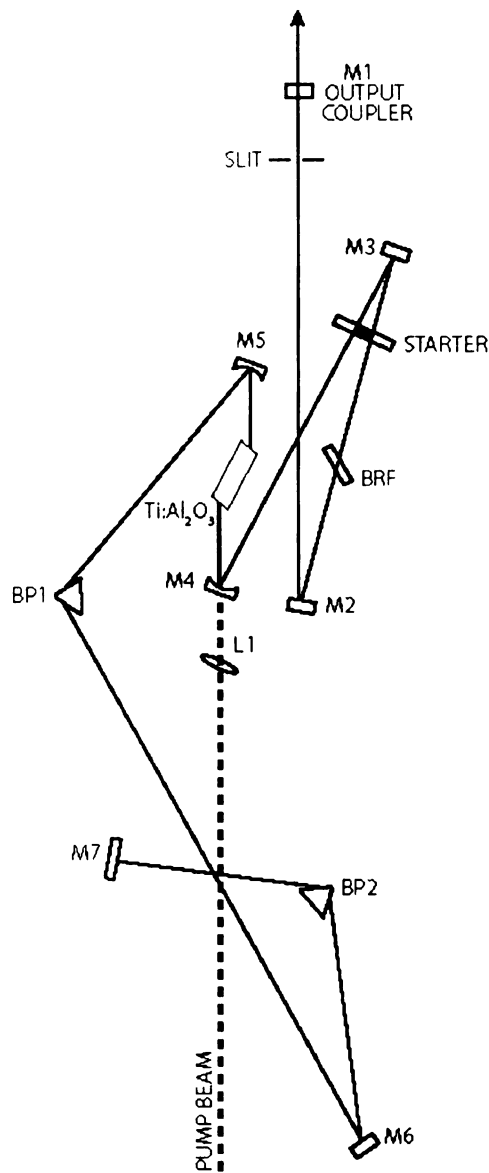


Figure 2.2. The Mira 900-F ti:sapphire laser oscillator and pulse compressor employed in the dynamic-absorption spectroscopy experiments. *Symbols:* M1, output coupler; BP1-BP2, Brewster prisms; M2-M3, flat cavity mirrors; BRF, birefringent filter; L1, focusing lens; M4-M5, curved mirrors; TiAl_2O_3 , titanium: sapphire crystal; M6, flat mirror; M7, flat end mirrors; p1-p2, SF10 prisms.

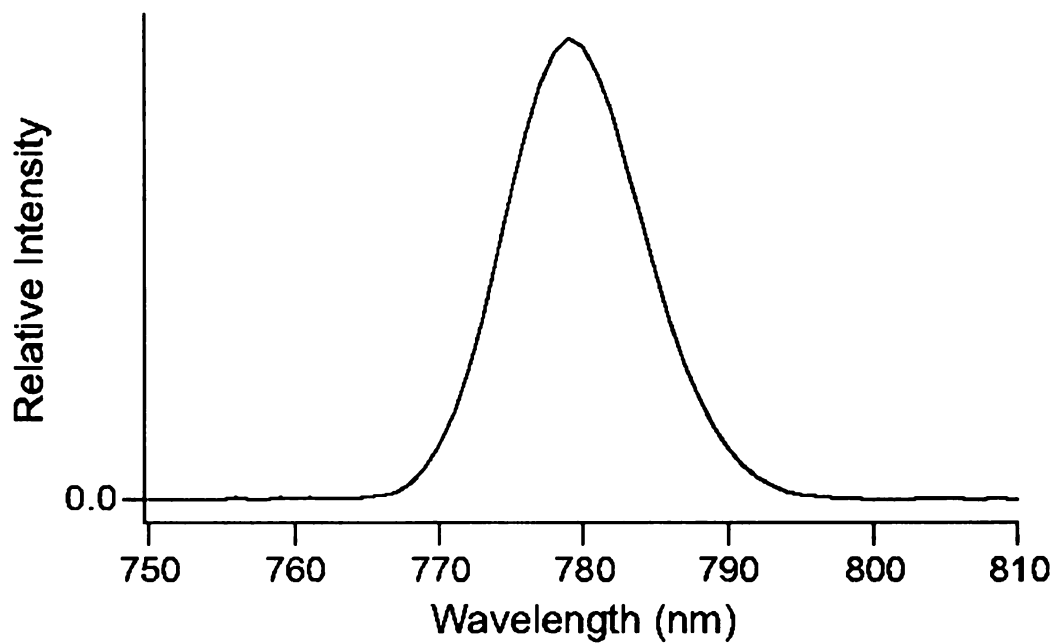


Figure 2.3. Output intensity spectrum of 60-fs (sech^2 ; 12-nm (fwhm) spectral width) pulses from the ti:sapphire oscillator.

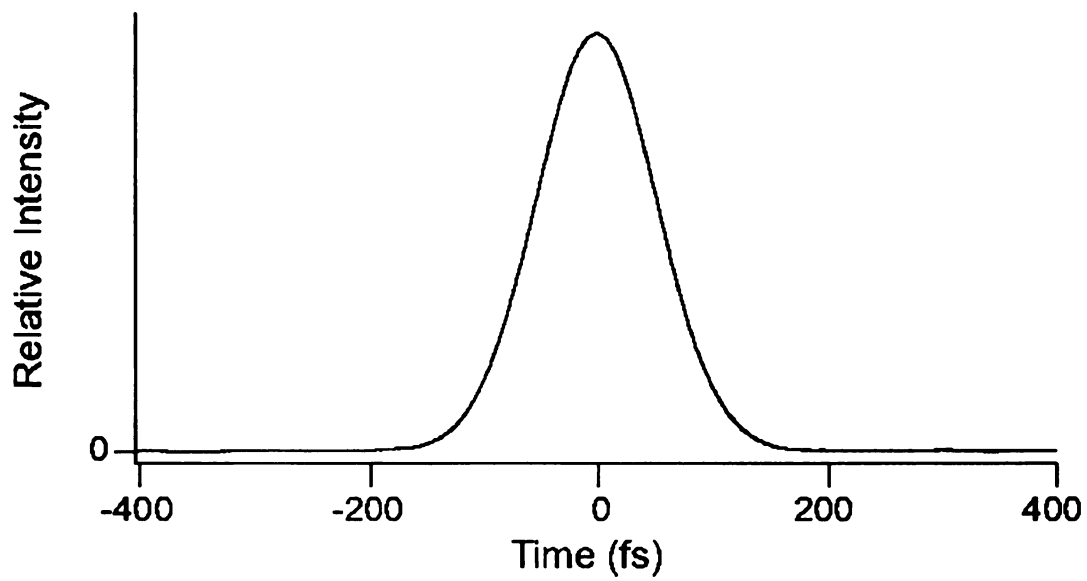


Figure 2.4. Zero-background autocorrelation trace of a 60-fs (sech^2) pulse obtained from the ti:sapphire oscillator.

2.2.2 Extracavity Pulse Compression

Extracavity pulse compression and group-velocity-dispersion precompensation was accomplished with a double-passed pair of SF10 prisms. The prism separation was adjusted to minimize the pump–probe autocorrelation width at the position of the reference nonlinear crystal (*vide infra*), which was confocal with the sample position. The design of the extracavity compressor is shown in figure 2.5.

2.2.3 Rapid-Scanning Modified Mach–Zehnder Interferometer

Femtosecond spectroscopy experiments employing multiple pulses require one arm of the interferometer to be scanned slowly. This motion is typically obtained step-wise with a delay stage. This technique can take seconds to acquire a single data point. A single scan can take minutes to obtain, resulting in large errors due to laser instability. Substituting a rapid scanning translation stage and retroreflector into the design increases signal-to-noise ratios without broadening the instrument response function.³¹ The interferometer also uses a $\lambda/2$ -retarding photoelastic modulator as a 100-kHz amplitude modulator. The design of the interferometer has been described by previous group members,^{27,28} but some significant changes have been made to improve sensitivity and reproducibility. Figures 2.6 and 2.7 show the design of the rapid-scanning modified Mach–Zehnder interferometer.

2.2.3.1 Layout of Interferometer

The horizontal polarization of the incident pulse train is rotated to vertical using a periscope arrangement with mirrors of *s* and *p* polarizations oriented for 45° reflections.

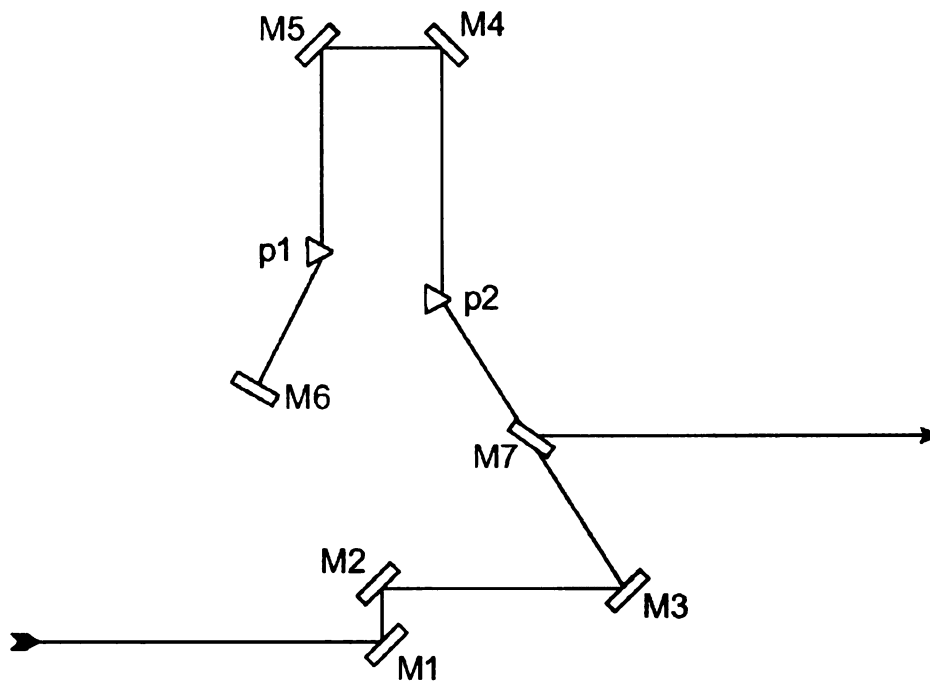


Figure 2.5. Extracavity compressor employed in the dynamic-absorption spectroscopy experiments. *Symbols:* M1-M6, silver mirrors; M7, half silver mirror; p1-p2, SF10 Brewster-angled prisms.

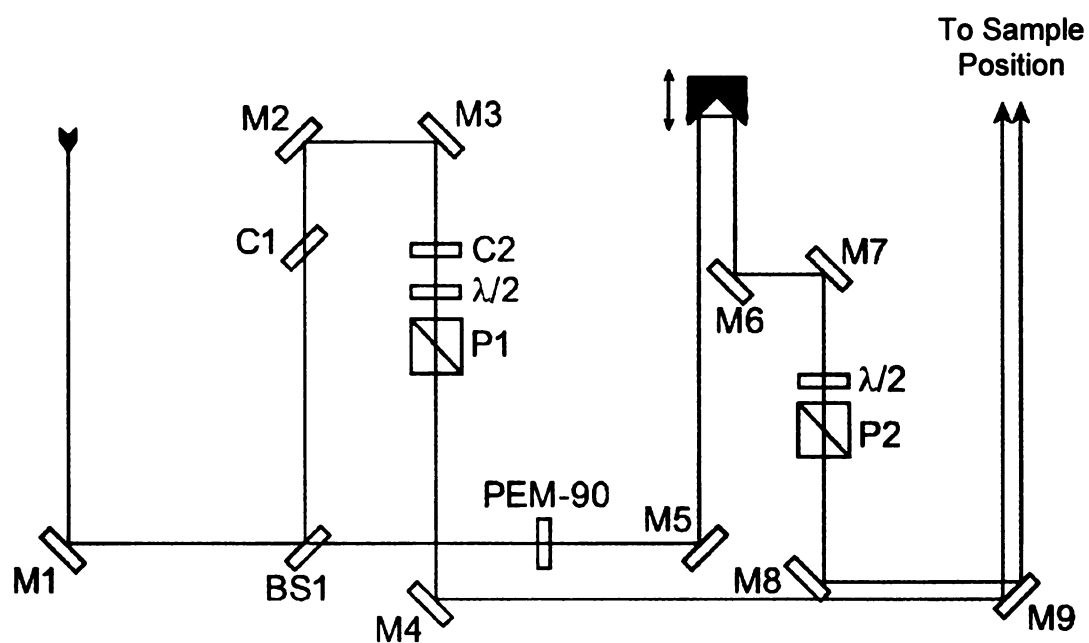


Figure 2.6. Modified Mach-Zehnder rapid-scanning interferometer employed in the dynamic-absorption spectroscopy experiments. *Symbols:* M1-M9, silver mirrors; BS1-BS2, beam splitters; C1-C2, compensation optics; $\lambda/2$, half-wave plates; P1-P2, Glan-laser calcite polarizers; PEM-90, photoelastic modulator.

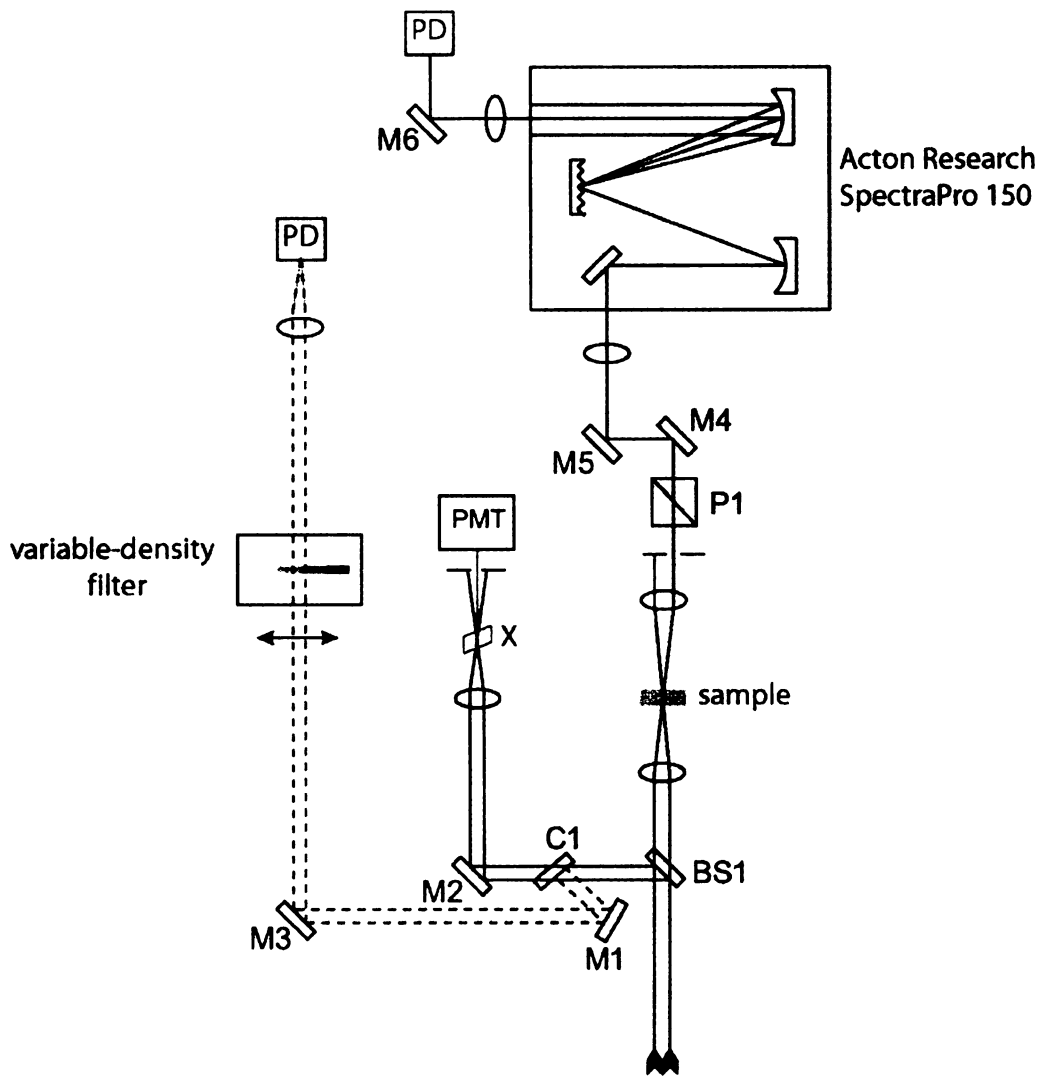


Figure 2.7. Sample and detection portion of the Modified Mach-Zehnder rapid-scanning interferometer employed in the dynamic-absorption spectroscopy experiments. *Symbols:* M1-M6, silver mirrors; BS1, beam splitters; C1, compensation optics; P1, Glan-laser calcite polarizers; x, β -barium borate crystal; PMT, photomultiplier tube; PD, photodiode.

The beam is split into pump and probe arms by a 50% beamsplitter. The probe arm employs a manually adjusted translation stage (Newport) and two silver mirrors (New Focus 5013) to balance the path length of the pump and probe arms of the interferometer.

A galvanometer-driven translation stage and retroreflector (Clark-MXR ODL-150) is used to scan the pump-pulse time-of-flight delay at a 1.3-Hz repetition rate over a 12-ps range. The pump beam is amplitude modulated at 100 kHz by a $\lambda/2$ -retarding fused-silica photoelastic modulator (Hinds Instruments) and a Glan-laser calcite polarizer (Karl Lambrecht). The fused silica plate in the photoelastic modulator is normal to the pulse train and 45° with respect to the optical table. The polarizer allows only vertically polarized light to pass. A mica zero-order $\lambda/2$ plate (Karl Lambrecht) prior to the polarizer is used to adjust the pulse train for 100% depth modulation.

The probe beam's plane of polarization is analyzed at 45° with respect to the pump beam's plane of polarization by a Glan-laser calcite polarizer; a mica zero-order $\lambda/2$ plate (Karl Lambrecht) is used to control the probe intensity. The polarizers were rotated to obtain a 4:1 pump-probe power ratio. The probe arm contains two compensation optics, one matching the beam splitter, the other matching the quartz plate in the photoelastic modulator, to exactly equate the material passed by the beam in both the pump and probe arms. This allows a single pair of prisms to compensate for group-delay dispersion.

A 10-cm focal-length BK7 lens was used to focus the pump (125 pJ/pulse, 10 mW) and probe beam (30 pJ/pulse, 2.5 mW) onto the sample's position. A 25- μm pinhole was used initially to ensure spatial overlap of the pump and probe beams. After transmitting through the sample and after recollimation, the probe beam was analyzed at 63.44° with respect to the pump polarization by another Glan-laser calcite polarizer in order to obtain

dichroism-free signals.⁵ The transmitted probe beam was then passed through a monochromator (Acton Research SpectraPro 150, 2-nm spectral band pass) and detected by an amplified silicon photodiode (Thorlabs PDA520). The photodiode signal was demodulated by a digital lock-in amplifier (SRS 750, Stanford Research Systems), which was referenced to the 100-kHz pump modulation frequency.

The lock-in amplifier was operated in a differential detection mode, with the transmitted-probe photodiode signal balanced by that from a second, reference photodiode. The reference photodiode was used to detect a variable sum of a portion of the pump and probe beams, both of which were split from the main beams prior to the sample-focusing lens. The intensity of the pump-beam fraction on the reference photodiode was adjusted with a variable-density neutral-density filter to cancel the post-time-zero bleaching signal at a closer point in the probe-delay scan; the unmodulated probe beam was used to bias the reference photodiode into the operating intensity regime used by the sample-beam's photodiode. This practice improved the signal/noise ratio significantly by allowing a partial nulling of the noise arising from the oscillator and pump laser.

The pump and probe beams were sampled prior to the focusing lens to provide a pair of reference pulses for autocorrelation analysis during data acquisition. A β -barium borate crystal (Cleveland Crystals, 100- μ m thickness, cut for type I sum-frequency generation with 800-nm input) was placed at the focus of a 10-cm focal-length BK7 lens; the second-harmonic beam was detected by a photomultiplier tube and lock-in amplifier (LIA-MV-200-H, Femto Messtechnik). The group-delay dispersion in the autocorrelation arm of the interferometer was the same as in the sample arm; identical beam

splitters, compensator plates, and focusing optics were employed. A sample/hold amplifier and digitizer (National Instruments SC-2040 S/H and PCI-6024E, respectively) simultaneously acquired at a 17-kHz sampling rate the analog output of the pump-probe and autocorrelation lock-in amplifiers, the photodiode intensity, and the galvanometer's position signal, resulting in 7000 points per scan; the effective dwell time per acquired data point was 1.8 fs. The signal-averaging system and monochromator were controlled by LabVIEW (National Instruments) routines. We eliminated scan-to-scan delay drift by employing the autocorrelation signal as a zero-delay time reference pulse for each scan; in previously reported rapid-scanning experiments, a modest broadening of the instrument-response function was observed in long averaging runs.^{27,32}

2.3 Data Acquisition

A sample/hold amplifier and digitizer (National Instruments, SC-2040S/H and PCI-6024E) was used to record the analog outputs of the two lock-in amplifiers (for the pump-probe signal and autocorrelation signal), the transmitted-probe photodiode signal, and the position of the galvanometer (delay reference) signal. Figure 2.8 shows the multiple traces that are obtained during dynamic-absorption experiments. Two complete scans of the rapid-scanning delay stage are shown as a function of real (laboratory) time.

The pump-probe delay is calculated from the position of the rapid-scanning delay stage. The position of the stage is calibrated by adjusting the distance the probe pulse must travel and measuring the movement of the zero-background autocorrelation signal relative to the position of the delay stage. The change in distance traveled by the probe pulse is converted to time and delay-stage position is measured in volts. A conversion

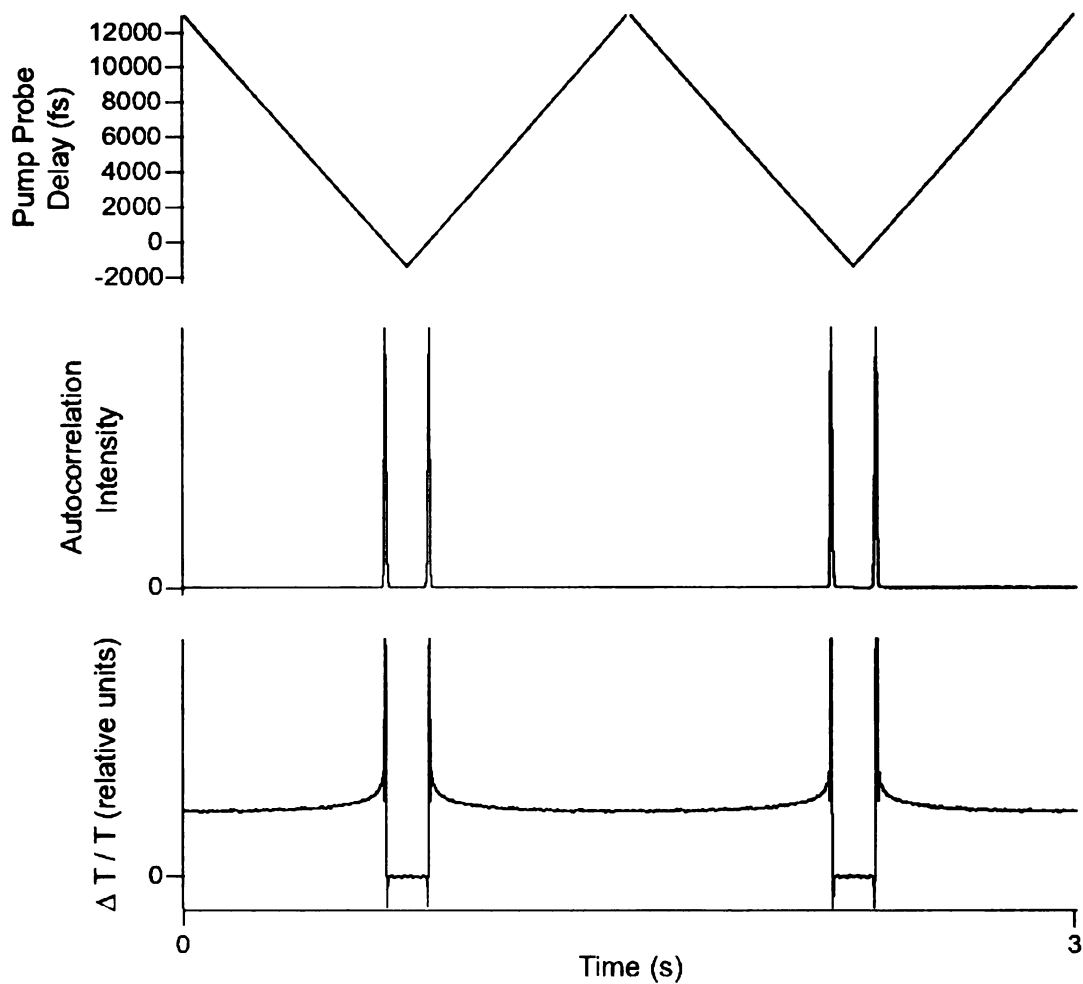


Figure 2.8. Multiple traces obtained simultaneously during dynamic-absorption experiments of bacteriochlorophyll *a* in pyridine. The probe beam was detected at 757 nm. Two complete scans of the rapid-scanning delay stage are shown as a function of real time. *Top:* Pump-probe delay determined from the position of the rapid-scanning delay stage. *Middle:* Zero-background autocorrelation. *Bottom:* Single-wavelength dynamic-absorption transient.

factor, with the units of fs/V, can be calculated and used to convert the position of the delay stage to pump-probe delay. In most experiments, the conversion factor was 19300 fs/V.

For each scan of the delay stage, the pump and probe pulses interact twice. As observed in figure 2.8, two scans of the delay stage give four zero-background autocorrelation and dynamic-absorption signals. Only data from one half of a complete scan is digitized in practice.

The scan range is adjusted to visualize only one pump-probe interaction, as shown in figure 2.9. The delay axis is scanned at 1.3 Hz over a 12-ps delay range and 7000 data points are acquired with a dwell time of 1.8 fs. The digitization frequency is 17 kHz. LabVIEW routines control the signal-averaging system and the monochromator. Multiple scans are averaged for a single-wavelength measurement. The autocorrelation signal is used as a zero-delay-time reference to eliminate scan-to-scan delay drift. Figure 2.10 shows a scan-averaged single-wavelength dynamic-absorption transient as a function of increasing probe delay.

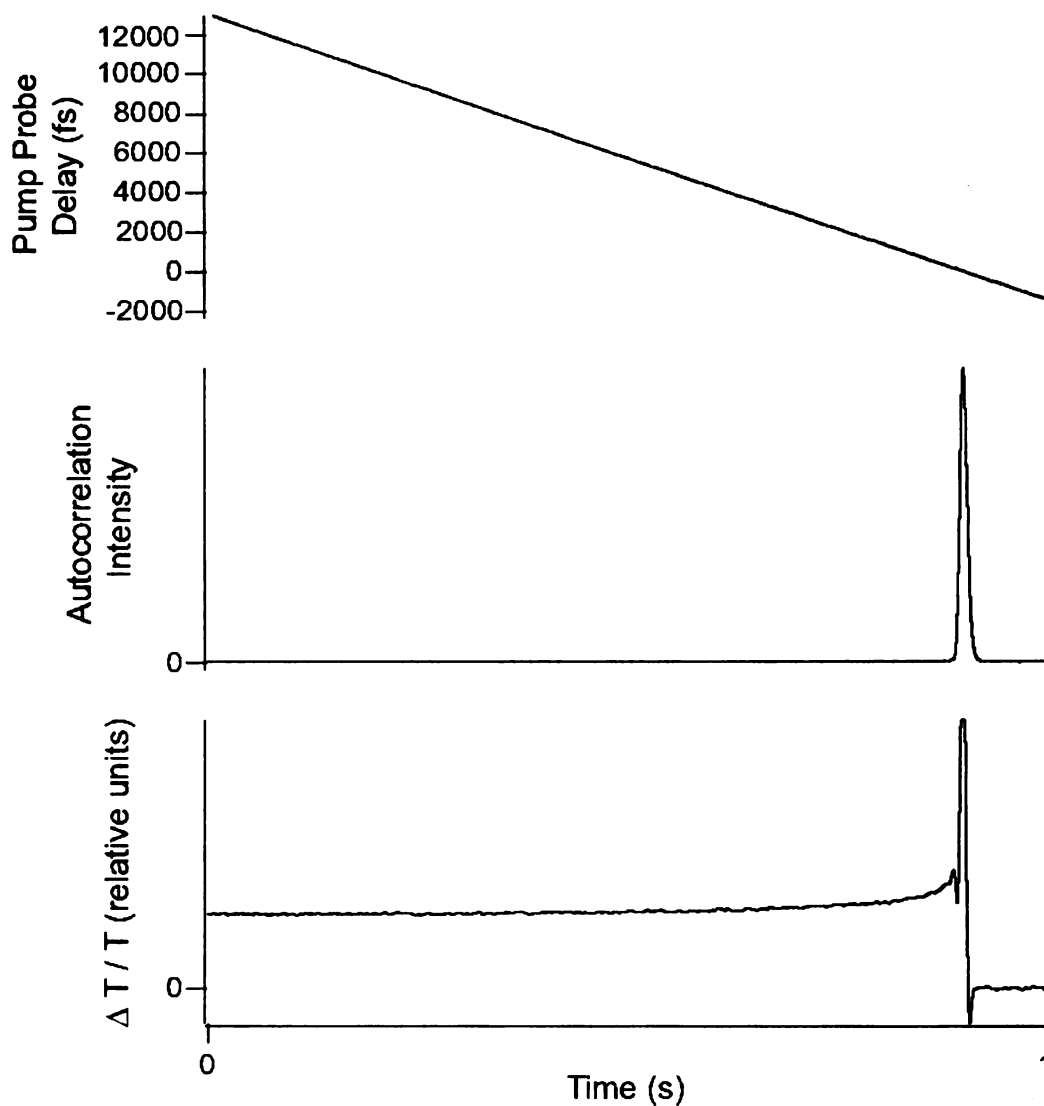


Figure 2.9. Zoomed traces from figure 2.8. obtained from bacteriochlorophyll *a* in pyridine. The probe beam was detected at 757 nm. A portion of one scan of the pump-probe delay is shown as a function of real time. *Top:* Probe delay as determined from the position of the rapid-scanning delay stage. *Middle:* Zero-background autocorrelation. *Bottom:* Single-wavelength dynamic-absorption transient.

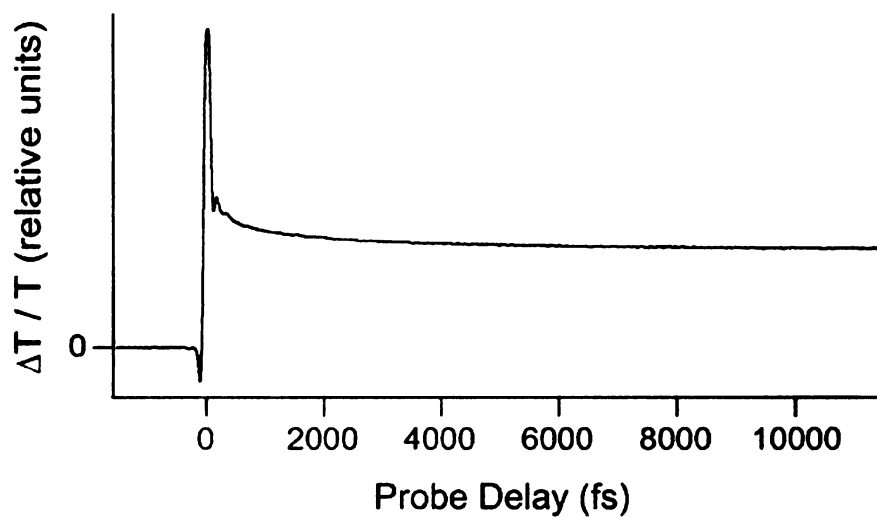


Figure 2.10. Single-wavelength dynamic-absorption transient of bacteriochlorophyll *a* in pyridine solvent displayed as a function of probe delay. The probe beam was detected at 757 nm.

2.4 References

- (1) Wang, Q.; Schoenlein, R. W.; Peteanu, L. A.; Mathies, R. A.; Shank, C. V. *Science* **1994**, *266*, 422–424.
- (2) Vos, M. H.; Rappaport, F.; Lambry, J.-C.; Breton, J.; Martin, J.-L. *Nature* **1993**, *363*, 320–325.
- (3) Vos, M. H.; Jones, M. R.; Hunter, C. N.; Breton, J.; Lambry, J.-C.; Martin, J.-L. *Biochemistry* **1994**, *33*, 6750–6757.
- (4) Vos, M. H.; Jones, M. R.; Hunter, C. N.; Breton, J.; Martin, J.-L. *Proc. Nat. Acad. Sci. USA* **1994**, *91*, 12701–12705.
- (5) Vos, M. H.; Jones, M. R.; McGlynn, P.; Hunter, C. N.; Breton, J.; Martin, J.-L. *Biochim. Biophys. Acta* **1994**, *1186*, 117–122.
- (6) Arnett, D. C.; Moser, C. C.; Dutton, P. L.; Scherer, N. F. *J. Phys. Chem. B* **1999**, *103*, 2014–2032.
- (7) Jonas, D. M.; Bradforth, S. E.; Passino, S. A.; Fleming, G. R. *J. Phys. Chem.* **1995**, *99*, 2594–2608.
- (8) Heller, E. J. *Acc. Chem. Res.* **1981**, *14*, 368–375.
- (9) Heller, E. J.; Sundberg, R. L.; Tannor, D. *J. Phys. Chem.* **1982**, *86*, 1822–1833.
- (10) Lee, S.-Y.; Heller, E. J. *J. Chem. Phys.* **1979**, *71*, 4777–4788.
- (11) Myers, A. B.; Mathies, R. A. In *Biological Applications of Raman Spectroscopy*; Spiro, T. G., Ed.; Wiley–Interscience: New York, 1987; Vol. 2, *Resonance Raman Spectra of Polyenes and Aromatics*, p 1–58.
- (12) Tannor, D. J.; Heller, E. J. *J. Chem. Phys.* **1982**, *77*, 202–218.
- (13) Williams, S. O.; Imre, D. G. *J. Phys. Chem.* **1988**, *92*, 3363–3374.

- (14) Pollard, W. T.; Fragnito, H. L.; Bigot, J.-Y.; Shank, C. V.; Mathies, R. A. *Chem. Phys. Letters* **1990**, *168*, 239–245.
- (15) Pollard, W. T.; Lee, S.-Y.; Mathies, R. A. *J. Chem. Phys.* **1990**, *92*, 4012–4029.
- (16) Pollard, W. T.; Dexheimer, S. L.; Wang, Q.; Peteanu, L. A.; Shank, C. V.; Mathies, R. A. *J. Phys. Chem.* **1992**, *96*, 6147–6158.
- (17) Pollard, W. T.; Mathies, R. A. *Annu. Rev. Phys. Chem.* **1992**, *43*, 497–523.
- (18) Zhu, L.; Sage, J. T.; Champion, P. M. *Science* **1994**, *266*, 629–632.
- (19) Peteanu, L. A.; Schoenlein, R. W.; Wang, Q.; Mathies, R. A.; Shank, C. V. *Proc. Natl. Acad. Sci. USA* **1993**, *90*, 11762–11766.
- (20) Schoenlein, R. W.; Peteanu, L. A.; Mathies, R. A.; Shank, C. V. *Science* **1991**, *254*, 412–415.
- (21) Fragnito, H. L.; Bigot, J.-Y.; Becker, P. C.; Shank, C. V. *Chem. Phys. Lett.* **1989**, *160*, 101–104.
- (22) Brito Cruz, C. H.; Fork, R. L.; Knox, W. H.; Shank, C. V. *Chem. Phys. Lett.* **1986**, *132*, 341–345.
- (23) Brito Cruz, C. H.; Gordon, J. P.; Becker, P. C.; Fork, R. L.; Shank, C. V. *IEEE J. Quant. Elect.* **1988**, *24*, 261–266.
- (24) Mathies, R. A.; Brito Cruz, C. H.; Pollard, W. T.; Shank, C. V. *Science* **1988**, *240*, 777–779.
- (25) Pollard, W. T.; Brito Cruz, C. H.; Shank, C. V.; Mathies, R. A. *J. Chem. Phys.* **1989**, *90*, 199–208.
- (26) Dexheimer, S. L.; Wang, Q.; Peteanu, L. A.; Pollard, W. T.; Mathies, R. A.; Shank, C. V. *Chem. Phys. Lett.* **1992**, *188*, 61–66.
- (27) Diffey, W. M.; Beck, W. F. *Rev. Sci. Instrum.* **1997**, *68*, 3296–3300.

- (28) Diffey, W. M.; Homoelle, B. J.; Edington, M. D.; Beck, W. F. *J. Phys. Chem. B* **1998**, *102*, 2776–2786.
- (29) Carson, E. A.; Diffey, W. M.; Shelly, K. R.; Lampa-Pastirk, S.; Dillman, K. L.; Schleicher, J. M.; Beck, W. F. *J. Phys. Chem. A* **2004**, *108*, 1489–1500.
- (30) Shelly, K. R.; Carson, E. A.; Beck, W. F. *J. Am. Chem. Soc.* **2003**, *125*, 11810–11811.
- (31) Edelstein, D. C.; Romney, R. B.; Scheuermann, M. *Rev. Sci. Instrum.* **1991**, *62*, 579–583.
- (32) Feldstein, M. J.; Vöhringer, P.; Scherer, N. F. *J. Opt. Soc. Am. B* **1995**, *12*, 1500–1510.

CHAPTER 3

VIBRATIONAL COHERENCE FROM THE DIPYRIDINE COMPLEX OF BACTERIOCHLOROPHYLL *a*: INTRAMOLECULAR MODES IN THE 10–220-cm⁻¹ REGIME, INTERMOLECULAR SOLVENT MODES, AND RELEVANCE TO PHOTOSYNTHESIS¹

3.0 Introduction

When impulsive (sub-vibrational-period) pump pulses are employed in experiments with reaction centers from purple bacteria, the stimulated emission and fluorescence signals from P exhibit intensity modulations at several frequencies over the 10–200-cm⁻¹ regime that persist as long as the 3-ps time scale for electron transfer to the bacteriopheophytin acceptor, BPh_L.^{1,2} The modulations arise from coherent wave-packet motions (vibrational coherence) on the excited-state potential-energy surface of P, but the nature of the normal modes that contribute to the signal is still debated. Because previous attempts to observe underdamped vibrational coherence from monomeric BChl in solution were unsuccessful,^{3,4} and because changes in the observed modulation frequencies occur in mutants,⁵ an assignment to BChl–protein intermolecular modes or to protein-derived modes was suggested.^{5,6} Resonance-Raman spectra obtained from reaction centers with isotopically labeled cofactors and normal-coordinate analyses suggest, in contrast, that intramolecular BChl modes are involved.^{7,8} Several of these modes have an out-of-plane character that would modulate the strong electronic coupling and intramolecular charge-transfer properties of P.⁷⁻¹³ There is the additional possibility that P exhibits a collective, intrapair mode that does not occur in BChl monomers.^{14,15}

¹ The material in this chapter has been published in another form: Shelly, K. R.; Carson, E. A.; Beck, W. F. *J. Am. Chem. Soc.* **2003**, *125*, 11810–11811.

The first observations of vibrational coherence in the 10-220-cm⁻¹ region from bacteriochlorophyll *a* (BChl) in solution are presented in the following sections. A distinction can be made for the first time between BChl's intramolecular normal modes and intermolecular modes between BChl and solvent. The results discussed in this chapter show that the low-frequency vibrations that accompany the initial electron-transfer reaction from the paired-BChl primary electron donor, P, in photosynthetic reaction centers¹⁶⁻¹⁸ arise predominantly from intramolecular modes of histidine-ligated BChl macrocycles. The results also suggest that polar solvent interactions can significantly perturb the electronic properties of BChl in a manner that might have important functional consequences.

3.1 Experimental

3.1.1 Sample Preparation

Synthetically prepared bacteriochlorophyll *a* (Frontier Scientific) was dissolved in anhydrous pyridine (spectrophotometric grade, acquired from Jade Scientific) to obtain an absorbance of 0.6 at 780 nm for a 1-mm path length. The sample was manipulated under a dry nitrogen atmosphere. It was held at room temperature (22 °C) in a fused-silica flow cuvette; the path length was 1 mm. The bacteriochlorophyll *a* solution was passed through a 0.22- μ m filter prior to use. BChl samples for femtosecond spectroscopy were held in a 1-mm, fused-silica flow cuvette. Samples were circulated using a peristaltic pump through the cuvette at a rate of 6 mL/min. The absorption spectrum of the sample was monitored throughout the duration of the experiment for changes arising from photochemistry or permanent photobleaching.

3.1.2 Continuous-Wave Spectroscopy

Continuous-wave absorption spectra for all samples were obtained with a Hitachi U-2000 spectrometer at 22 °C with 2-nm spectral band pass. Fluorescence spectra were acquired at room temperature with a Hitachi F-4500 fluorescence spectrophotometer (5-nm excitation and emission band pass). The fluorescence intensities were corrected using a calibration curve obtained from a standard lamp. When presented as a function of wavenumber, the fluorescence intensities are multiplied by the square of the wavelength in order to compensate for the fixed (in wavelength units) spectral band pass of the emission spectrometer.^{20,21}

3.1.3 Femtosecond Spectroscopy

Dynamic-absorption spectroscopy was performed with the femtosecond pump-probe spectrometer described in Chapter 2, figures 2.2 and 2.5-2.7. In the experiments described in this chapter, the output spectrum emitted by the oscillator exhibited a bandwidth of 12 nm, 250 cm⁻¹ (fwhm), centered at 780 nm. The extracavity SF10 prisms were adjusted to produce 50-fs pulses (sech²). The transmitted probe light was detected at 787 nm (2-nm band pass).

3.2 Results

3.2.1 Continuous-Wave Spectroscopy

Figure 3.1 shows the absorption and fluorescence spectra exhibited by BChl in pyridine solvent at room temperature. The spectra are plotted as $A(\nu)/\nu$ and $F(\nu)/\nu^3$, respectively, with normalization to unit area. The integrals of these quantities report the

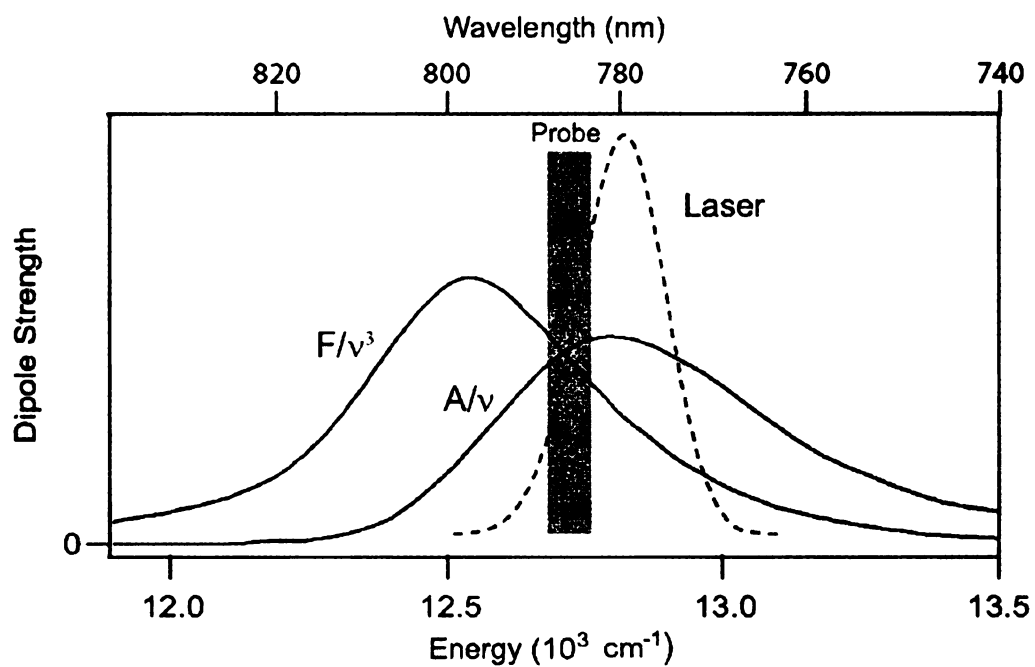


Figure 3.1. Continuous-wave absorption and fluorescence spectra from bacteriochlorophyll *a* in pyridine plotted as relative dipole strengths, $A(\nu)/\nu$ and $F(\nu)/\nu^3$, respectively. The spectra are normalized to unit area. The fluorescence spectrum was excited at 790 nm (12700 cm^{-1}).

dipole strength; the square of the transition-dipole moment, which is proportional to the Einstein coefficients for absorption and stimulated emission, B_{ab} and B_{ba} , respectively.^{20,26} As plotted, the sum of the spectra can be compared to the time-integrated dynamic-absorption spectrum in the weak-field limit.²⁷ The 0–0 vibronic transition is found in the vicinity of 12700 cm^{-1} (790 nm), where the two normalized spectra cross. Also shown in figure 3.1 is the intensity spectrum from the ti:sapphire laser that was the source of pump and probe pulses in the dynamic-absorption experiments. The shaded region in figure 3.1 coincides with the portion of the transmitted probe spectrum that was passed by the monochromator to the photodiode.

In the dynamic-absorption experiments, the titanium sapphire laser's spectrum ($12600\text{--}13000\text{ cm}^{-1}$, with peak intensity at 12800 cm^{-1}) excites BChl over a spectral range that starts just to the red of the absorption maximum, passes through the 0–0 transition, and proceeds on to cover the entire peak of the absorption band. The laser spectrum also spans a large fraction of the blue tail of the fluorescence spectrum. Accordingly, as used in the dynamic-absorption experiments as the probe beam, the laser spectrum covers some of the stimulated emission spectrum and the ground-state depletion spectrum, allowing for detection of both ground-state and excited-state vibrational coherence.

3.2.2 Dynamic-Absorption Experiments

The dynamic-absorption transient obtained from BChl in pyridine is shown in figure 3.2. Following an intense coherence spike near the zero of time, the transient exhibits two regions of vibrational coherence. These regions are more easily discernible in the oscillatory portion of the pump–probe signal. The oscillatory signal is isolated by subtracting a fitted triple-exponential function from the signal starting at 200 fs and

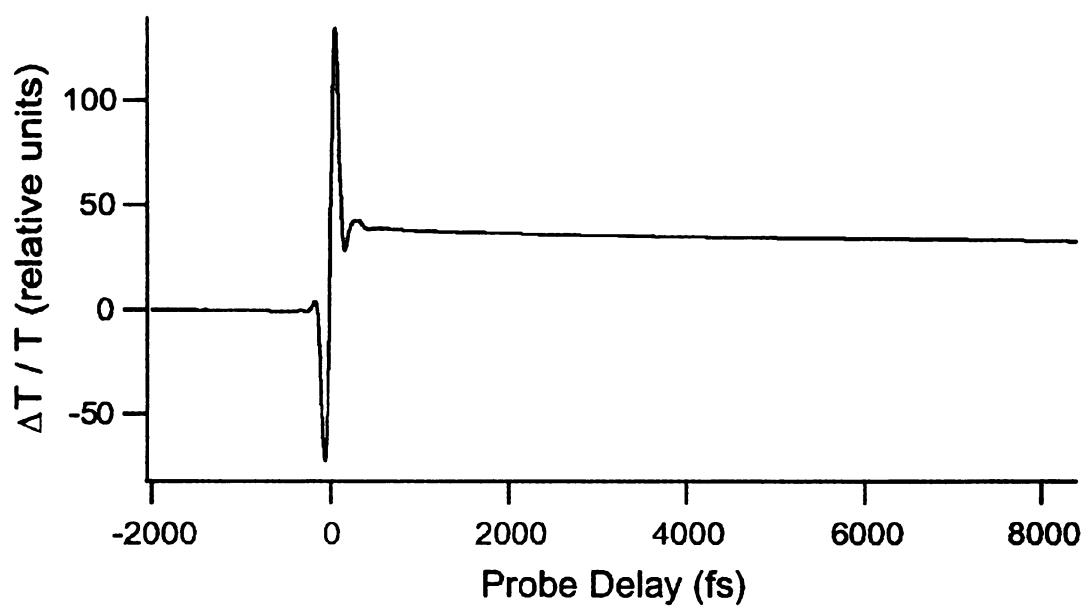


Figure 3.2. Pump-probe signal obtained from BChl in pyridine solvent.

extending to the end of the recorded range at 8 ps. The triple exponential fit and corresponding residual oscillatory fraction can be seen in the top and bottom panels, respectively, of figure 3.3.

Figure 3.3 shows the 200–7000-fs delay range of the oscillatory portion of the pump–probe signal obtained from BChl in pyridine with excitation of the Q_y transition. The first region of vibrational coherence is a relatively intense, rapidly damped feature in the 200–600-fs regime. Following the rapidly damped section, a second region of weaker underdamped cosinusoidal modulations is observed that persists even to the 8-ps delay point. Because the probe wavelength lies just to the blue of the fluorescence spectrum, the modulations mostly arise from the excited-state wave packet in the near-turning-point region.²⁴

The Fourier-magnitude spectrum corresponding to the slowly-damped modulations is shown in figure 3.4. The spectrum reports at least twelve reproducible modulation components, with center frequencies ranging from 11 to 206 cm^{-1} . Above 30 cm^{-1} , the spectrum strongly resembles the resonance-Raman spectra from P and/or the monomeric species BChl_L and BChl_M in the reaction center^{7,29-31} in having significant peaks at 138 cm^{-1} and 183 cm^{-1} , respectively.

3.2.3 Rapidly-Damped Vibration Coherence from Bacteriochlorophyll *a* and Pyridine

In this section, we consider in more detail how much the pyridine solvent contributes to the BChl pump–probe signal in the region of time where the strong, rapidly-damped oscillation is observed. Figure 3.5 compares the pump–probe signal obtained at room temperature from BChl in pyridine solvent with the signal obtained under the same ex-

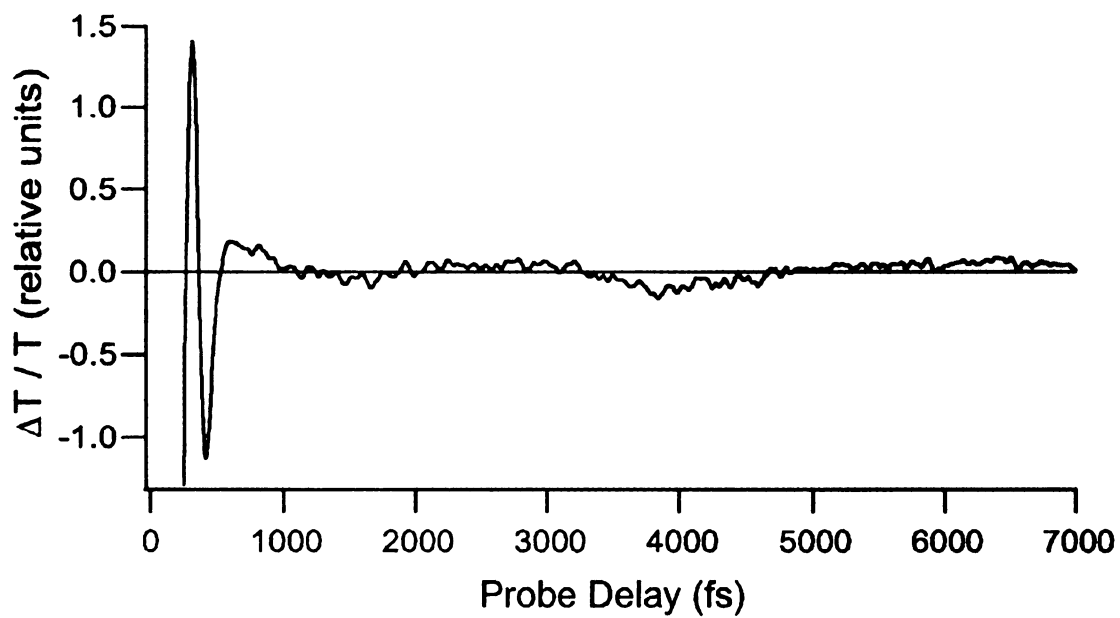
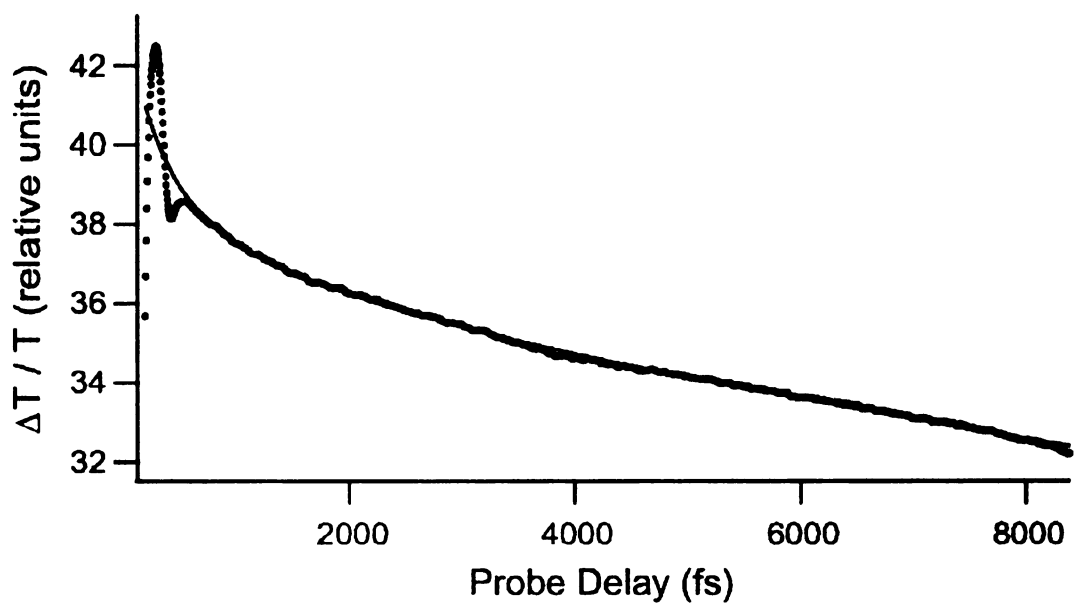


Figure 3.3. Triple exponential fit (top) and corresponding residual oscillatory portion of the pump-probe signal from BChl in pyridine (bottom).

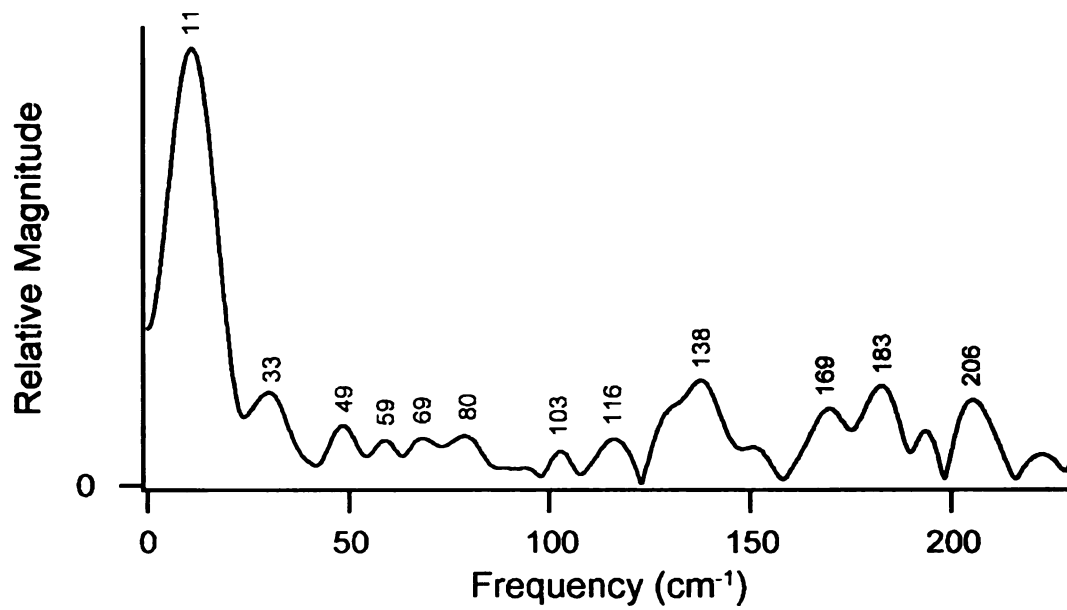


Figure 3.4. Hanning-windowed Fourier-magnitude spectrum of the 200-8000-fs range.

perimental conditions from neat pyridine solvent. Note that the y axes of the two graphs are set up so that the relative intensities of the two signals can be determined by inspection. The discussion that follows shows that we can neglect any contribution of the nonresonant oscillatory signal from pyridine to the signals shown in figures 3.2-3.3 and 3.7.

The BChl pump–probe signal shown in figure 3.5 is the same one used in figures 3.2-3.3 and 3.7. The most intense feature is the bipolar pump–probe coherence spike near the zero of time. This spike is superimposed on the pump-induced change in transmittance that can be attributed to the change in ground-state population arising from the $\pi \rightarrow \pi^*$ transition; the intensity change from the baseline prior to time zero and nondecaying ($\gamma > 1$ ns) fraction corresponds to a $\Delta T/T$ of 10^{-4} . As stated in the caption to figure 3.5, the full range of the oscillatory signal used in figure 3.2 and in the subsequent analysis of the components of the vibrational coherence is perhaps ten percent as large, a $\Delta T/T$ of 10^{-5} . In terms of the relative-intensity units used in figures 3.2 and 3.5, there is a full-scale modulation of about 2.5 units.

The pump–probe signal observed in neat pyridine arises from the optical-Kerr effect (OKE). It exhibits a spike near the zero of time that arises from the nonresonant electric hyperpolarizability, a weak beating modulation near the 150-fs time point, and a subsequent exponential decay that arises from diffusive reorientational relaxation. The signal is very similar in shape to that reported in the past by McMorrow and Lotshaw,³³ but the laser pulses used in our experiment are shorter in duration. The signal/noise ratio of our signal is poor compared to that of the McMorrow and Lotshaw signal, even after many hours of signal averaging, because we detect the signal against a large transmitted-

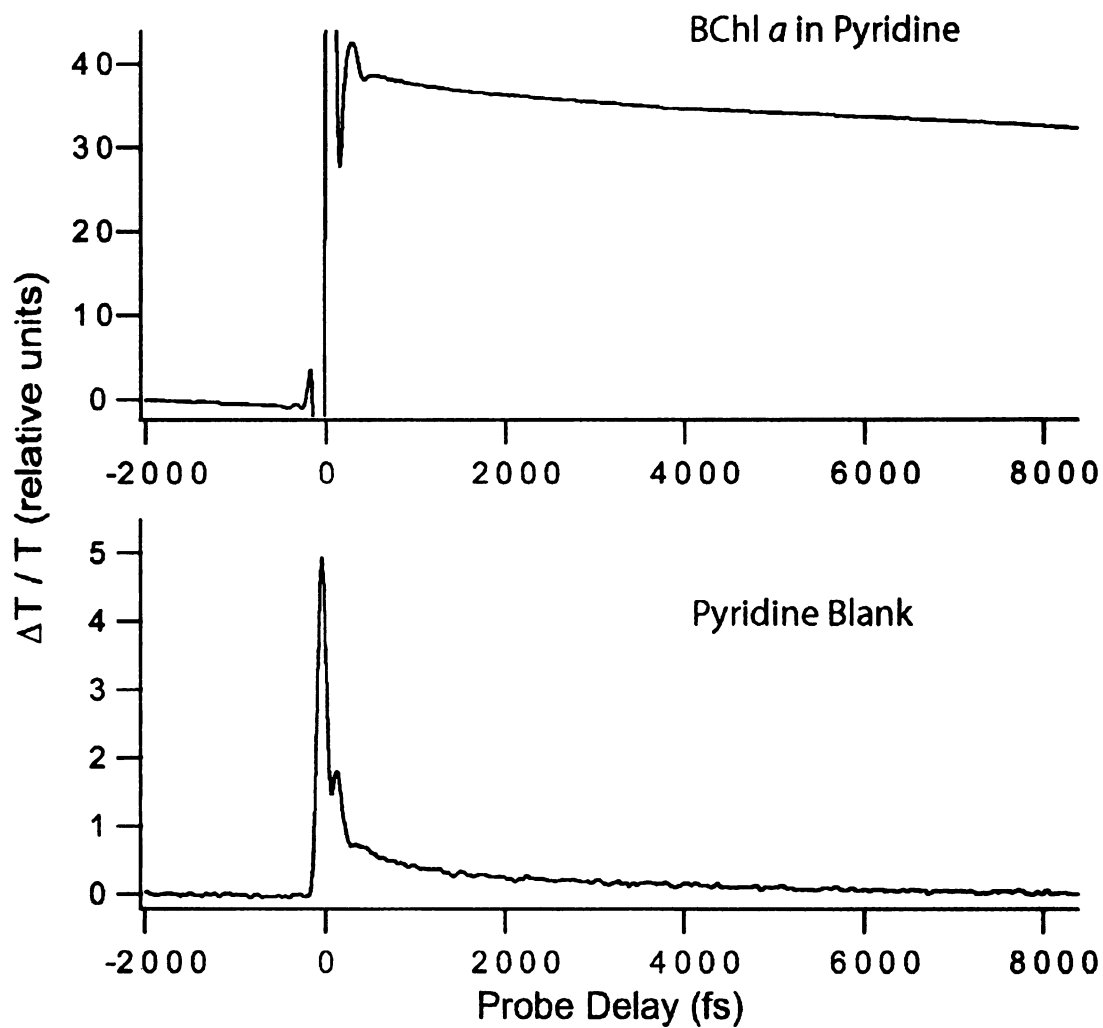


Figure 3.5. Pump-probe signal obtained under the same optical conditions from BChl in pyridine solvent and in neat pyridine. The top graph shows the range corresponding to the population change in the BChl ground state. The y axes employ a consistent relative-intensity scaling.

probe background. (The best technique for detection of nonresonant OKE signals is to rotate the probe-analyzing polarizer so that it is crossed (obtaining maximum extinction) against the probe's plane of polarization; then, by a small rotation of a $\lambda/4$ retarder plate or of the analysis polarizer, a small leakage signal from the probe is admitted to obtain optical-heterodyne detection (OHD) conditions. So, the OHD-OKE signal is detected essentially against a zero background, and the signal/noise ratio is appropriately much better than that obtained under our conditions. In effect, our analysis polarizer is rotated way beyond the limit needed to obtain full heterodyning.) Our intention, here, of course, is not to record the OHD-OKE signal but to obtain a valid estimate of how much the pyridine solvent itself contributes a nonresonant background signal in the pump-probe experiment with BChl present, under the same optical conditions.

Over the time range from 150 fs to 7 ps shown in figure 3.3, the pyridine blank exhibits a full-range modulation of much less than 1 relative-intensity unit. Figure 3.5 shows that the significant OKE modulations observed in pyridine occur at shorter delay times and exhibit a different intensity profile than those observed in the BChl/pyridine sample. Further, the BChl and pyridine-OKE modulation spectra are not the same. The pyridine OKE spectrum (not shown), obtained using the methods of the next section, exhibits a peak in the $60\text{--}90\text{-cm}^{-1}$ regime and substantial intensity in the $0\text{--}60\text{-cm}^{-1}$ region; considering the effects of our shorter laser pulses, the spectrum is consistent with that reported previously by McMorrow and Lotshaw.³³

A direct comparison of intensities between the BChl and pyridine-blank sample is not appropriate because it does not account for the attenuation of the laser intensity in the BChl sample. In the BChl pump-probe experiment, the absorbance was 0.6 at the center

of the laser spectrum. With respect to the background pyridine OKE signal, the presence of BChl contributes an attenuation of the laser fluence for the pump and probe beams and it attenuates the exiting third-order polarization signal (the OKE signal) beam to the same degree. Accordingly, in the presence of BChl, the background pyridine OKE signal is approximately $1/(10^{-0.6})^3 = 1.6 \times 10^{-2} = 1/163$ as large as that observed in neat pyridine. Given the very small amplitude of this signal over the range of the BChl signal that is shown in figure 3.5, it is certainly safe to ignore the presence of the OKE signal in the analysis.

3.3 Data Analysis

3.3.1 Fourier-Magnitude Spectrum Estimation

The oscillatory fraction of the pump–probe signal (see figure 3.3) was obtained by subtracting a fitted triple-exponential function from the signal segment starting well beyond the pump–probe coherence spike, at the 150-fs delay point, and extending to the end of the acquired signal. It was then multiplied by a Hanning (or raised cosine) window function,³⁸

$$w(k) = 0.5 \left(1 - \cos \left(\frac{2\pi k}{n+1} \right) \right) \quad (3.1)$$

defined for the point index k in the data segment in terms of the number of data points n . The window function gradually forces the intensity at the beginning and end of the signal segment to zero amplitude. This procedure is required to suppress satellite ripples in the Fourier-magnitude spectra, which arise from leakage of signal frequencies into adjacent channels owing to truncation of the time-domain signal at the beginning and end. The window function also causes a broadening of the observed signal line shape at a given

frequency, but this same broadening can be applied in simulation of the frequency-domain spectrum to return accurate damping constants. Next, the windowed signals were zero-padded by a factor of 32 in order to enhance the point density along the frequency axis in the Fourier-magnitude spectra. Lastly, the spectrum was compensated for the finite width of the instrument-response function by deconvolution in the frequency domain: the raw magnitude was scaled by the reciprocal of the Fourier magnitude at frequency ω , obtained from the pump-probe autocorrelation signal.³⁹ This analysis is shown in detail in figure 3.6. The top panel shows an oscillatory signal with a frequency of 200 cm^{-1} and a damping time of 100 fs. The middle panel shows the signal after multiplication by the Hanning window function described by equation 3.1, where the intensity at the beginning and end of the signal go to zero amplitude. The resulting Fourier magnitude spectrum is shown in the bottom panel of figure 3.6.

The reader should take note that the deconvolution step mentioned above causes the signal/noise to deteriorate as the frequency increases. This effect arises from the need to have the laser pulses be much shorter than the period of a given mode's vibrational period. With our 50-fs pulses, we find that we cannot reproduce features in the Fourier-magnitude spectrum above 220 cm^{-1} . At that point, the power in the pump-probe autocorrelation function is about 50 percent of that at 0 cm^{-1} . The resolution of the Fourier-magnitude spectrum is determined by the length of the analyzed time-domain data segment and the windowing function. Using the modulated portion of the BChl signal shown in figure 3.3, the effective resolution in the calculated Fourier-magnitude spectrum is 10 cm^{-1} .

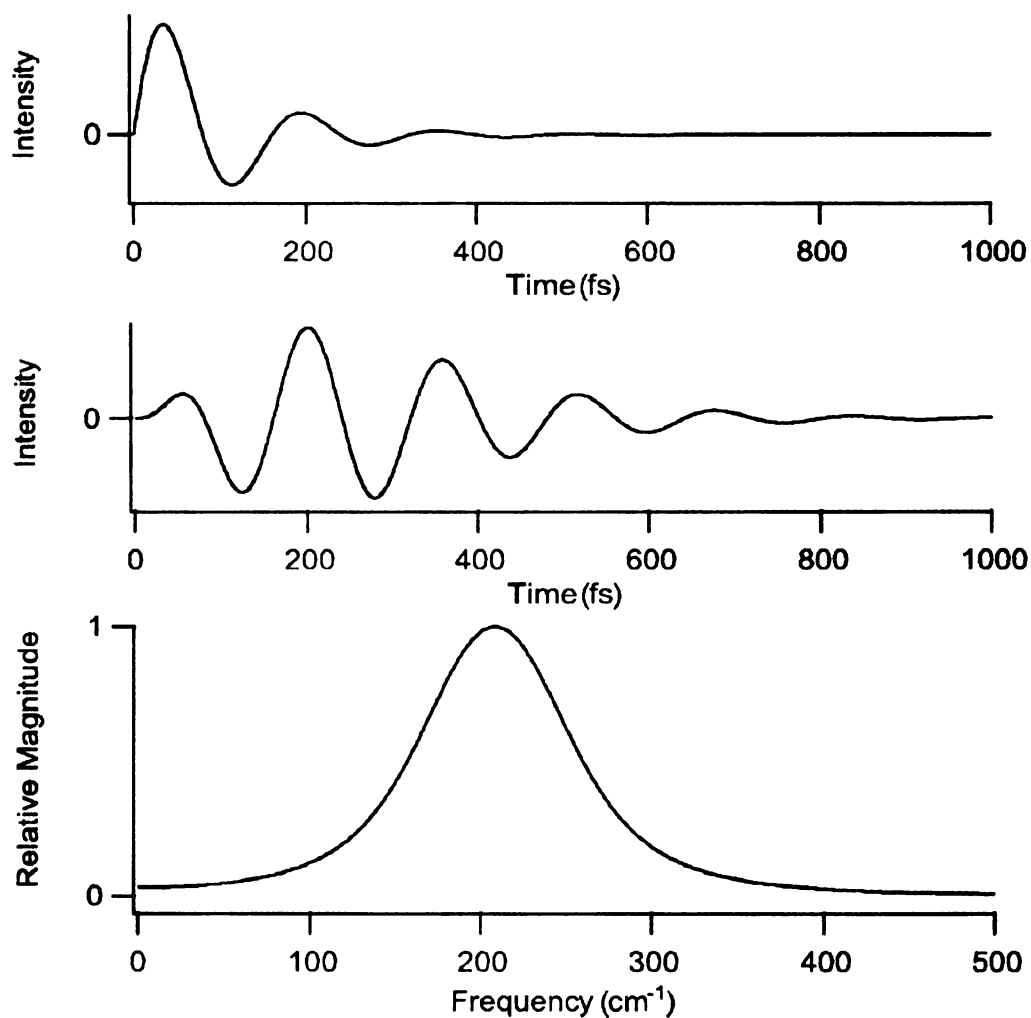


Figure 3.6. Oscillatory signal with a frequency of 200 cm^{-1} and a damping time of 100 fs (top panel). Oscillatory signal from top panel multiplied by a Hanning window function described by equation 3.1 (middle panel). Hanning-windowed Fourier-magnitude spectrum of the 200-cm^{-1} oscillation (bottom panel).

3.3.2 Modeling of the Slowly Damped Components.

The parameters listed in table 3.1 were obtained by a robust frequency-domain modeling procedure.²⁴ The experimental Fourier-magnitude spectrum (figure 3.4) was modeled using a sum of damped cosines,

$$I(t) = \sum_i A_i e^{-t/\gamma_i} \cos(\omega_i t + \phi_i) \quad (3.2)$$

The model signal was sampled using the delay times t and segment lengths obtained from the experimental signal (see figure 3.2); it was processed by the same sequence of windowing, zeropadding, and Fourier-magnitude spectrum calculation. The intensities A_i , frequencies ν_i , and damping times γ_i were adjusted iteratively to reproduce the intensity, position, and width of each significant feature in the experimental Fourier-magnitude spectrum. Note that the phases ϕ_i are optionally obtained by optimization of the model in the time domain. The components that were included in the model are those that were reproduced in frequency and relative intensity in a set of replicate experiments.

3.3.3 Modeling of the Rapidly Damped Component

The broad line shapes that would be expected from the rapidly-damped region are not observed in the frequency domain due to the Hanning window function used to obtain the Fourier-magnitude spectra. The Hanning window greatly reduces the intensity of this time region, so the Fourier-magnitude spectra are dominated by the vibrational coherence observed on a longer timescale ($\tau > 1000$ fs). Accordingly, the rapidly damped modulation component observed over the 200–600-fs time region (see figures 3.2 and 3.3) was modeled using a distribution of sinusoidal components defined by the sum of

Table 3.1. Frequencies, normalized deconvolved intensities,^a and damping constants for the underdamped oscillatory components^b observed in the pump-probe signal from bacteriochlorophyll *a* in pyridine solvent

frequency (cm ⁻¹)	intensity ^a	γ (fs)
11	1.00	800
33	0.09	1100
49	0.03	1500
59	0.02	1700
68	0.03	1500
80	0.03	1500
103	0.02	1700
116	0.04	1500
138	0.26	1000
169	0.12	1200
182	0.18	1200
206	0.16	1300

^arelative to the magnitude of the 11-cm⁻¹ component after deconvolution in the frequency domain

^bmodeled by a sum of damped cosinusoids, $\sum_i A_i e^{-t/\gamma_i} \cos(\omega_i t)$

two lognormal (asymmetric Gaussian)⁴⁰ distribution functions, resulting in a model signal that closely approximates the time-domain signal (see figure 3.3). (This model will be discussed in more detail in Chapter 4.) The distribution was sampled at 5-cm⁻¹ intervals from 1 cm⁻¹ to 1000 cm⁻¹. The intensity of the distribution at each sampling point was used as the scaling factor for a damped cosinusoid, as in equation 3.2, above. The damping factor for each component was arbitrarily fixed at 1 ps; changing this parameter (say, to 2 ps) had little effect on the time-domain signal obtained by summing over the entire distribution.

The parameters for the two lognormal components were iteratively adjusted until a close facsimile of the observed signal was obtained (see the top panel of figure 3.7). The final parameters are listed in table 3.2.

3.4 Discussion

3.4.1 Observation of Two Damping Time Scales

Two damping time scales are observed in the ground-state vibrational coherence from BChl in pyridine. The difference in line shape for the two regions of vibrational coherence indicates that they arise from two distinct classes of vibrational modes.

We suggest that the rapidly-damped vibrational components arise from intermolecular modes between the BChl macrocycle and the surrounding solvent. The rapidly-damped modes have inhomogeneously broadened line shapes that can be described by a distribution of damped cosinusoids. The distribution arises from the disordered ensemble of solvated bacteriochlorophyll structures.

Similar broad spectra are observed in *nonresonant* optical-Kerr-effect (OKE) signals

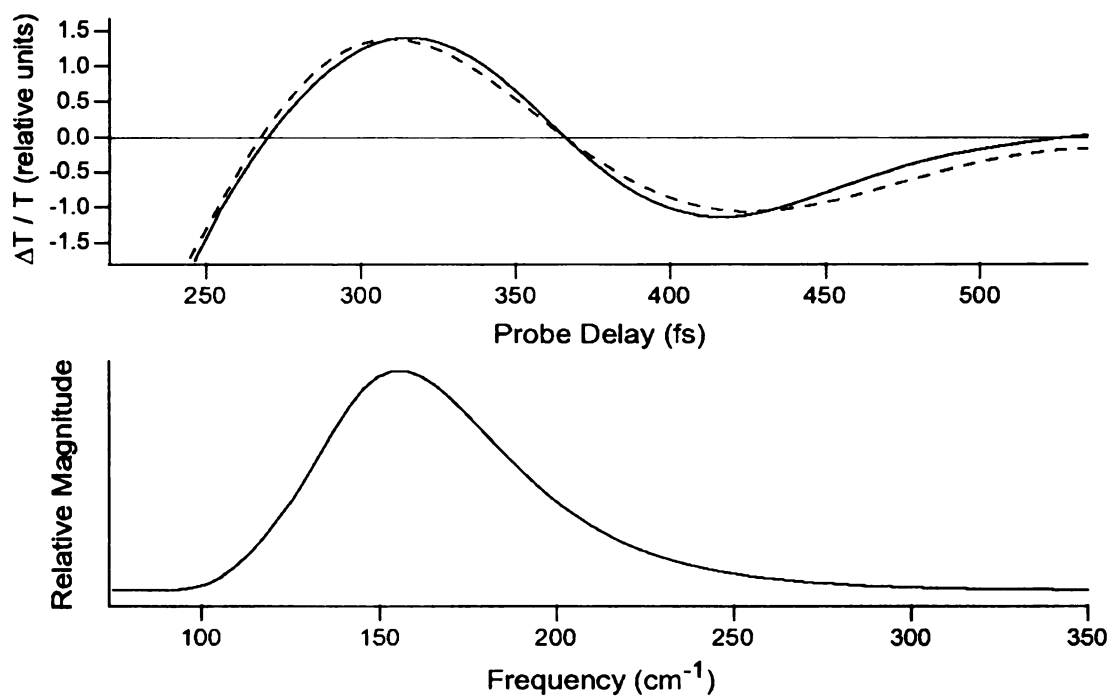


Figure 3.7. Expanded view of the rapidly damped oscillation from BChl in pyridine solvent (see figure 3.5.) superimposed with a model (dashed curve) arising from a distribution of mode frequencies, as shown in the bottom panel.

Table 3.2. Log-normal line shape parameters for the solvent-mode distribution^a

component	amplitude	frequency (cm ⁻¹)	width (cm ⁻¹)	skew
1	0.68	145	35	1.2
2	1	175	47	1.2

^amodeled using a distribution of cosinusoidal components defined by the sum of two lognormal (asymmetric Gaussian)⁴⁰ distribution functions

from liquids, which carry modulations arising from librational (hindered reorientational) motions.³² But the OKE spectrum from pyridine liquid is observed at a lower frequency, 60 cm⁻¹, with collective modes making a contribution at 15 cm⁻¹.³³ The *resonant* origin of the present signal requires the involvement of a BChl–solvent-pyridine intermolecular mode that is displaced by the BChl $\pi \rightarrow \pi^*$ transition. The relatively high frequency favors an assignment to a perpendicular hydrogen-bonding interaction like that present in pyrrole,^{34,35} with protons of non-ligated pyridines in the first solvent shell attacking the BChl π -electron density.

In addition to the rapidly-damped components, slowly-damped vibrational components are observed arising from intramolecular motions from the BChl macrocycle itself. The intramolecular modes exhibit comparable intensities over the 30–200-cm⁻¹ region, but the 11-cm⁻¹ mode and the pyridine-solvent mode yield much stronger signals. As indicated in table 3.2, the relatively intense 11-cm⁻¹ component (3-ps period) exhibits the broadest line shape (damping constant $\gamma = 800$ fs); the higher-frequency components exhibit sharper line shapes ($\gamma = 1.2$ – 1.7 ps). The observation of the sharp line shapes supports the suggestion⁷ that the very lowest-frequency components are affected by the nature of the axial ligand to the Mg(II) ion. Owing to the long damping times, in the range of those observed for intramolecular modes of organic molecules in solution,^{24,28} we know that these features arise from intramolecular modes belonging to the BChl–dipyridine complex.

These observations prompt the following conclusions about the role that BChl–protein “solvent” interactions might play in the reaction center:

1. Owing to its low frequency, the 11-cm⁻¹ mode involves motion of a large reduced

mass along a coordinate with a weak force constant, such as an out-of-plane distortion of the BChl macrocycle. We suggest that resonance enhancement of this mode involves coupling to the pyridine-solvent mode, but it is not obvious why the other low-frequency modes, several of which have some degree of out-of-plane character,^{7,8} are not as strongly enhanced. The low-frequency intramolecular modes of BChls in the reaction center might be comparably affected by mode-specific and highly directional BChl–protein interactions. In fact, the resonance-Raman spectra from BChl_{L,M} and P exhibit distinct low-frequency intensity patterns^{7,8,29-31} that probably arise from the details of the binding sites.

2. The broad line shape for the solvent mode in pyridine liquid arises from the disordered ensemble of solvated BChl structures. The strength of this signal suggests that some of the changes in the vibrational coherence from P in mutant reaction-center preparations⁵ might arise from an *ordered* solvent interaction, which would exhibit a *narrow* line shape, between P and the surrounding protein.

The observation of polar-solvent effects on the resonance-Raman intensities from the BChl-dipyridine complex imply that significant changes in the *electronic structure* of the BChl macrocycle should arise from protein-derived solvent perturbations in the reaction center. These interactions might contribute to the protein's control over the reactivity of a BChl site despite not necessarily causing a large change in the geometry. Some larger effects on the resonance-Raman spectra and charge-transfer properties of BChl_L and BPh_L owing to an introduction of neighboring charges have already been reported.^{36,37}

3.5 References

- (1) Vos, M. H.; Rappaport, F.; Lambry, J.-C.; Breton, J.; Martin, J.-L. *Nature* **1993**, *363*, 320–325.
- (2) Stanley, R. J.; Boxer, S. G. *J. Phys. Chem.* **1995**, *99*, 859–863.
- (3) Savikhin, S.; Zhu, Y.; Lin, S.; Blankenship, R. E.; Struve, W. S. In *Ultrafast Phenomena IX*; Barbara, P. F., Knox, W. H., Mourou, G. A., Zewail, A. H., Eds.; Springer-Verlag: Berlin, 1994, p in press.
- (4) Chachisvilis, M.; Fidler, H.; Pullerits, T.; Sundström, V. *J. Raman Spect.* **1995**, *26*, 513–522.
- (5) Rischel, C.; Spiedel, D.; Ridge, J. P.; Jones, M. R.; Breton, J.; Lambry, J.-C.; Martin, J.-L.; Vos, M. H. *Proc. Natl. Acad. Sci. USA* **1998**, *95*, 12306–12311.
- (6) Vos, M. H.; Martin, J.-L. *Biochim. Biophys. Acta* **1999**, *1411*, 1–20.
- (7) Czarniecki, K.; Diers, J. R.; Chynwat, V.; Erickson, J. P.; Frank, H. A.; Bocian, D. F. *J. Am. Chem. Soc.* **1997**, *119*, 415–426.
- (8) Palaniappan, V.; Aldema, M. A.; Frank, H. A.; Bocian, D. F. *Biochemistry* **1992**, *31*, 11050–11058.
- (9) Warshel, A.; Parson, W. W. *J. Am. Chem. Soc.* **1987**, *109*, 6152–6163.
- (10) Warshel, A.; Parson, W. W. *J. Am. Chem. Soc.* **1987**, *109*, 6143–6152.
- (11) Thompson, M. A.; Zerner, M. C.; Fajer, J. J. *J. Phys. Chem.* **1991**, *95*, 5693--5700.
- (12) Thompson, M. A.; Zerner, M. C.; Fajer, J. J. *J. Phys. Chem.* **1990**, *94*, 3820–3828.
- (13) Lathrop, E. J. P.; Friesner, R. A. *J. Phys. Chem.* **1994**, *98*, 3056–3066.
- (14) Warshel, A. *Proc. Natl. Acad. Sci. USA* **1980**, *77*, 3105–3109.
- (15) Hayes, J. M.; Small, G. J. *J. Phys. Chem.* **1986**, *90*, 4928–4931.
- (16) Parson, W. W. In *Photosynthesis (New Comprehensive Biochemistry, Volume 15)*; Amesz, J., Ed.; Elsevier: New York, 1987, p 43–61.
- (17) Boxer, S. G.; Goldstein, R. A.; Lockhart, D. J.; Middendorf, T. R.; Takiff, L. *J. Phys. Chem.* **1989**, *93*, 8280–8294.
- (18) Friesner, R. A.; Won, Y. *Biochim. Biophys. Acta* **1989**, *977*, 99–122.
- (19) Alden, R. G.; Cheng, W. D.; Lin, S. H. *Chem. Phys. Lett.* **1992**, *194*, 318–326.

- (20) Lakowicz, J. R. *Principles of Fluorescence Spectroscopy*; Second ed.; Kluwer Academic/Plenum Publishers: New York, 1999.
- (21) Lampa-Pastirk, S.; Lafuente, R. C.; Beck, W. F. *J. Phys. Chem. B* **2004**, *108*, 12602–12607.
- (22) Diffey, W. M.; Beck, W. F. *Rev. Sci. Instrum.* **1997**, *68*, 3296–3300.
- (23) Diffey, W. M.; Homoelle, B. J.; Edington, M. D.; Beck, W. F. *J. Phys. Chem. B* **1998**, *102*, 2776–2786.
- (24) Carson, E. A.; Diffey, W. M.; Shelly, K. R.; Lampa-Pastirk, S.; Dillman, K. L.; Schleicher, J. M.; Beck, W. F. *J. Phys. Chem. A* **2004**, *108*, 1489–1500.
- (25) Shelly, K. R.; Carson, E. A.; Beck, W. F. *J. Am. Chem. Soc.* **2003**, *125*, 11810–11811.
- (26) Cantor, C. R.; Schimmel, P. R. *Biophysical Chemistry. Part II: Techniques for the Study of Biological Structure and Function*; W. H. Freeman and Company: San Francisco, 1980.
- (27) Pollard, W. T.; Mathies, R. A. *Annu. Rev. Phys. Chem.* **1992**, *43*, 497–523.
- (28) Bardeen, C. J.; Shank, C. V. *Chem. Phys. Lett.* **1994**, *226*, 310–316.
- (29) Shreve, A. P.; Cherepy, N. J.; Franzen, S.; Boxer, S. G.; Mathies, R. A. *Proc. Natl. Acad. Sci. USA* **1991**, *88*, 11207–11211.
- (30) Cherepy, N. J.; Shreve, A. P.; Moore, L. J.; Franzen, S.; Boxer, S. G.; Mathies, R. A. *J. Phys. Chem.* **1994**, *98*, 6023–6029.
- (31) Cherepy, N. J.; Shreve, A. P.; Moore, L. J.; Boxer, S. G.; Mathies, R. A. *J. Phys. Chem. B* **1997**, *101*, 3250–3260.
- (32) Lotshaw, W. T.; McMorrow, D.; Thantu, N.; Melinger, J. S.; Kitchenbaum, R. *J. Raman Spect.* **1995**, *26*, 571–583.
- (33) McMorrow, D.; Lotshaw, W. T. *Chem. Phys. Lett.* **1993**, *201*, 369–376.
- (34) Gamba, Z.; Klein, M. L. *J. Chem. Phys.* **1990**, *92*, 6973–6974.
- (35) Wynne, K.; Galli, C.; Hochstrasser, R. M. *Chem. Phys. Lett.* **1992**, *193*, 17–22.
- (36) Cua, A.; Kirmaier, C.; Holten, D.; Bocian, D. F. *Biochemistry* **1998**, *37*, 6394–6401.
- (37) Czarnecki, K.; Kirmaier, C.; Holten, D.; Bocian, D. F. *J. Phys. Chem. A* **1999**, *103*, 2235–2246.

- (38) Press, W. H.; Flannery, B. P.; Teukolsky, S. A.; Vetterline, W. T. *Numerical Recipes: the Art of Scientific Computing*; Cambridge University Press: Cambridge, 1986.
- (39) McMorrow, D.; Lotshaw, W. T. *Chem. Phys. Lett.* **1990**, *174*, 85–94.
- (40) Siano, D. B.; Metzler, D. E. *J. Chem. Phys.* **1969**, *51*, 1856–1861.

CHAPTER 4

INTERMOLECULAR VIBRATIONAL COHERENCE BETWEEN BACTERIOCHLOROPHYLL *a* AND POLAR AND NONPOLAR SOLVENTS

4.0 Introduction

We focus in this chapter on the structural origin of the rapidly damped components of the vibrational coherence that can be observed in BChl solutions as discussed in chapter 3. The intention of this work is to test our assignment of the rapidly damped signals to modes involving the solvent molecules. We compare the rapidly damped vibrational coherence observed at room temperature in BChl *a* solutions in pyridine, acetone, and 1-propanol. We also present the rapidly damped vibrational coherence observed in BChl *a* in a nonpolar solvent, cyclohexane. The results support an assignment of the vibrational coherence to intermolecular modes between BChl and clustered solvent molecules in the first solvation shell because the mode frequency scales with the dipole moment of the polar solvent. The evidence of vibrational coherence in BChl *a* solutions in cyclohexane suggests that the intermolecular binding potential also depends on the polarizability of the solvent. This work shows for the first time that intermolecular modes between large electronic chromophores and the surrounding solvent can be resonance Raman active.

4.1 Experimental Procedures

4.1.1 Sample Preparation

4.1.1.1 Bacteriochlorophyll *a* in polar solvents

Synthetically prepared bacteriochlorophyll *a* was used as received from Frontier Scientific. Samples for femtosecond spectroscopy were prepared in a glove bag under a

dry N₂ atmosphere and in minimal light. Pyridine (spectrophotometric grade) was obtained from Jade Scientific; acetone was obtained from J. T. Baker; 1-propanol was obtained from CCI. The dry BChl powder was dissolved in enough solvent to obtain an absorbance of 0.6–0.7 at 750 nm for a 1-mm path length. The samples were passed through a 0.22- μ m filter prior to use.

4.1.1.2 Bacteriochlorophyll *a* in cyclohexane

Bacteriochlorophyll *a* was used as received from Frontier Scientific. Samples were prepared under the same conditions as described above. Pyridine (spectrophotometric grade) was obtained from Jade Scientific; cyclohexane (spectrophotometric grade) was obtained from Spectrum. To the calculated volume of cyclohexane required to dissolve 1 mg of dry BChl powder at an absorbance of 0.6-0.7 at 750 nm for a 1-mm path length, a certain number of equivalents of pyridine was added to establish a chosen BChl:pyridine ratio. The samples were passed through a 0.22- μ m filter prior to use.

4.1.2 Continuous-Wave Spectroscopy

Continuous-wave absorption and fluorescence spectra for all samples were acquired at room temperature with Hitachi U-2000 and Hitachi F-4500 spectrometers, respectively. The fluorescence intensities were corrected as described in chapter 3.

4.1.3 Femtosecond Spectroscopy

Dynamic-absorption spectroscopy was performed with a self-mode-locked ti:sapphire oscillator and a rapid-scanning, modified Mach-Zehnder interferometer. The spectrometer's main features have been described in Chapter 2. For these experiments,

the ti:sapphire oscillator was pumped by a Verdi (Coherent) ND-YVO₄ 5-W laser. The oscillator was tuned to obtain a spectrum centered at 750 nm; the bandwidth was 11.5 nm (fwhm). The width of the zero-background autocorrelation function at the sample position was 60-fs fwhm (sech²) in these experiments. Probe light was detected at 757 nm (2-nm band pass). The differential probe detection scheme, as described in Chapter 2, was employed in these experiments to partially cancel laser noise.

BChl samples for femtosecond spectroscopy were held at room temperature (22 °C) in a fused-silica flow cuvette; the path length was 1 mm. Samples were circulated using a peristaltic pump through the cuvette at a rate of 6 mL/min. The absorption spectrum of the sample was monitored throughout the duration of the experiment for changes arising from photochemistry or permanent photobleaching.

4.2 Results

4.2.1 Continuous-Wave Spectroscopy

Figures 4.1 and 4.2 show the continuous-wave absorption spectra from BChl *a* in cyclohexane solvent at various BChl:pyridine ratios and in the three polar solvents; pyridine, 1-propanol and acetone. The spectra span the three absorption bands arising from $\pi \rightarrow \pi^*$ transitions: with increasing wavelength, the Soret or *B* band (~420-nm, from $S_0 \rightarrow S_n$ transitions), and the Q_x and Q_y bands (~600 nm and ~750 nm, from $S_0 \rightarrow S_1$ transitions).

The spectra from BChl in cyclohexane show the effects of the binding of pyridine to an axial ligation site on the central Mg(II) ion. The spectra from the 1:0.6 BChl:pyridine ratio shows a red shoulder in the 820-nm range that evidences the presence of BChl-BChl aggregates in the sample. This red shoulder has largely disappeared in the 1:1.2 sample,

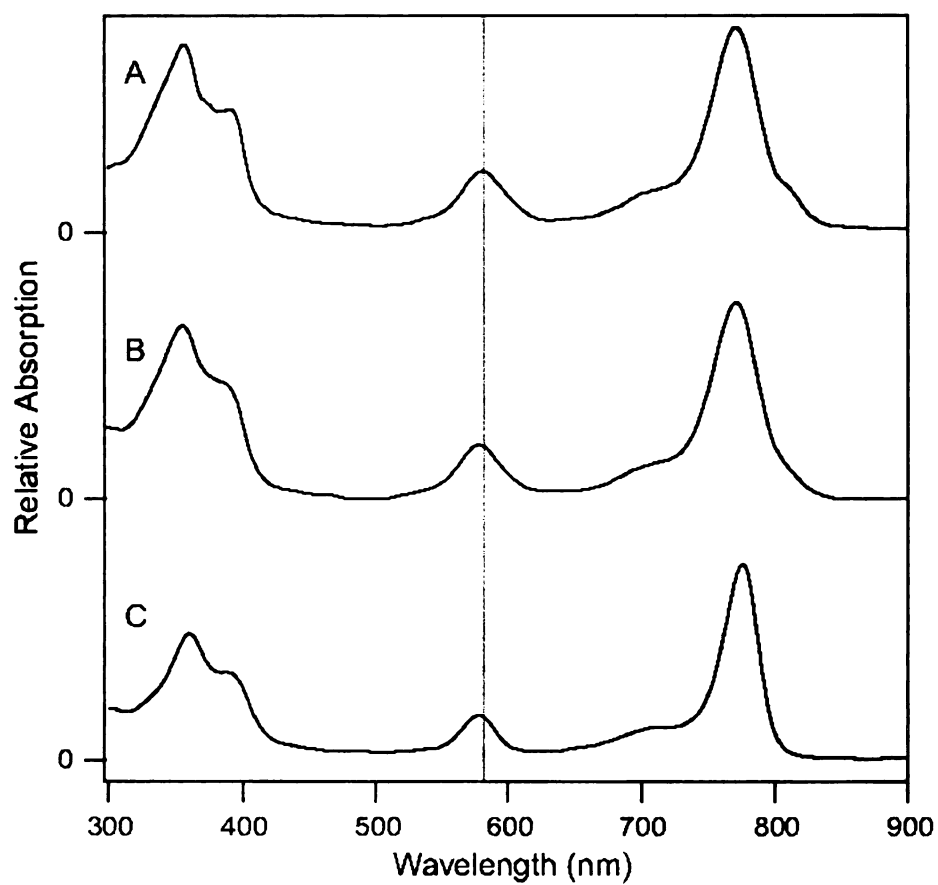


Figure 4.1. Continuous-wave absorption spectra at 22 °C from BChl *a* in cyclohexane solvent at BChl:pyridine ratios of (a)1:0.6, (b)1:1.2, and (c)1:100. The vertical line is at 580 nm.

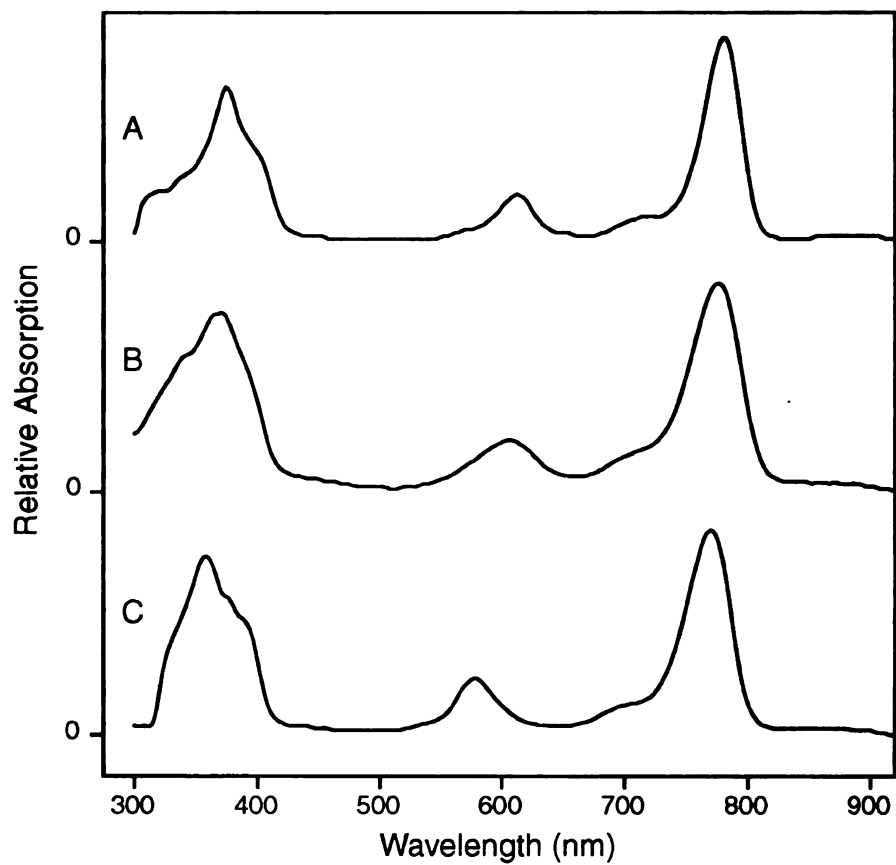


Figure 4.2. Continuous-wave absorption spectra at 22 °C from BChl *a* in three neat solvents: (a) pyridine, (b) 1-propanol, and (c) acetone.

so this sample mostly contains BChl monomers. The 1:100 sample is red-shifted and narrowed somewhat due to the presence of excess pyridine in the bulk solvent. All three samples show a Q_x absorption in the 580-nm range, which shows that the central Mg(II) ion in the BChl macrocycle (see figure 4.3) ligates at most a single pyridine. The presence of an axially ligated pyridine is necessary to avoid the formation of aggregates because the peripheral ketone functional groups tend to find the axial binding sites.

Figure 4.2 shows that the Q_y bands observed in 1-propanol and acetone are shifted to the blue from that in pyridine, by 4 and 7 nm, respectively, owing to bulk solvatochromism. Similar small shifts would be anticipated for the Q_x bands, but the Q_x band observed in acetone is shifted to the blue farther than would be expected by solvatochromism alone from the Q_x bands observed in pyridine and 1-propanol. Katz and coworkers¹⁻³ showed that this shift arises from a change in axial coordination for the Mg(II) ion bound by the BChl macrocycle. Observation of the Q_x band for BChl *a* in the 610-nm region indicates the presence of two axially ligated solvent molecules, so the Mg(II) ion is six-coordinate in pyridine and 1-propanol, with two solvent molecules bound axially in each case.² The 580-nm Q_x band observed in acetone, however, indicates that the Mg(II) ion coordinates only a single acetone ligand.

The pump-probe experiments reported in this chapter were conducted with excitation of the Q_y absorption band. Figure 4.4 shows the Q_y -band absorption and fluorescence spectra of BChl *a* in pyridine at 22 °C. The spectra are plotted with respect to wavenumber as $A(\nu)/\nu$ and $F(\nu)/\nu^3$, respectively, with normalization to unit area. Also shown in figure 4.4 is the output spectrum from the ti:sapphire oscillator that was employed in the dynamic-absorption, one-color pump-probe experiments. The shaded

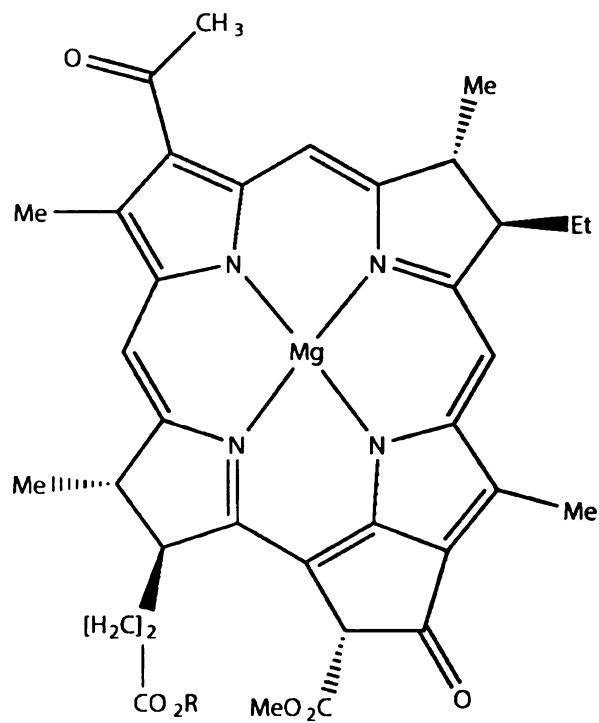


Figure 4.3. Structure of bacteriochlorophyll *a* molecule, the dominant chromophore in purple non-sulfur photosynthetic light-harvesting proteins.²

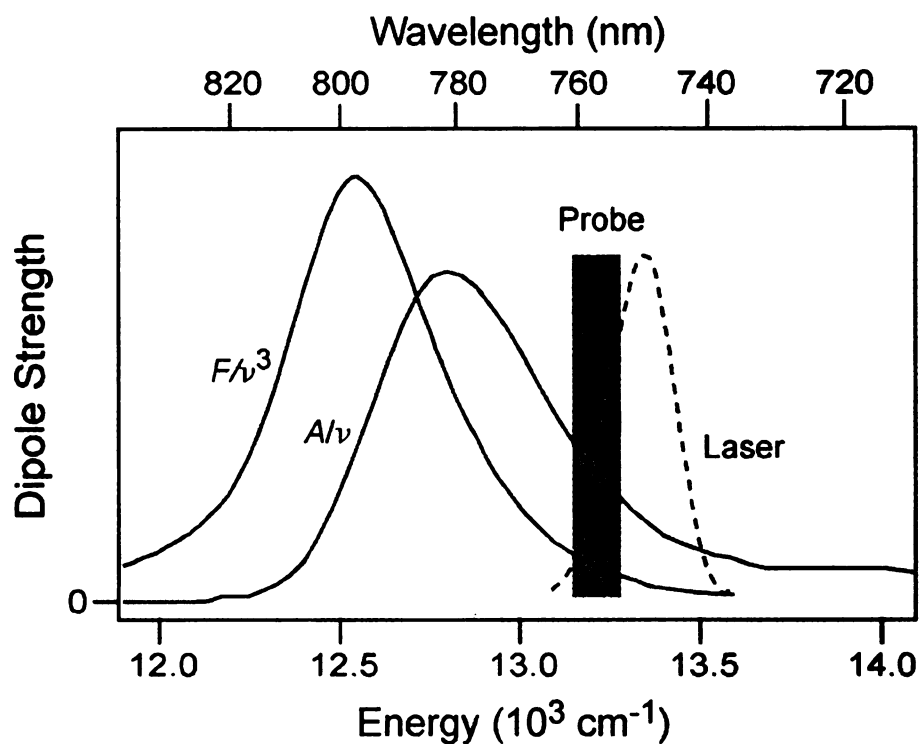


Figure 4.4. Continuous-wave absorption and fluorescence spectra from BChl in pyridine solvent plotted as the dipole strength, $A(\nu)/\nu$ and $F(\nu)/\nu^3$, respectively, and normalized to unit area. The dashed curve shows the intensity spectrum emitted by the ti:sapphire oscillator. The shaded region shows the range of the transmitted probe light that was passed by the monochromator to the detector in the dynamic-absorption experiment.

region marks the 4-nm band pass of the transmitted probe spectrum that was passed by the monochromator to the photodiode. The oscillator was tuned to obtain a spectrum that was centered at 757 nm in order to move the probe spectrum as far off resonance from the BChl *a* stimulated-emission spectrum as possible and yet still have the pump spectrum on resonance with the ground-state absorption spectrum. The absorption and fluorescence dipole-strength spectra shown in figure 4.4 can be used to judge the relative contributions of signals from wave packets on the ground state and excited state, respectively, in the detected probe band width. The pump spectrum and detected probe band width specified in figure 4.4 favors detection of ground-state vibrational coherence prepared by resonant impulsive stimulated Raman scattering (RISRS).⁴

4.2.2 Dynamic-Absorption Experiments

The dynamic-absorption transient obtained from BChl *a* in pyridine is shown in figure 4.5. Following an intense coherence spike⁵⁻⁸ near the zero of time, the transient exhibits a short series of damped oscillations, with two strong recurrences prior to the 500-fs delay point. The first intense beat, at 200 fs, corresponds to the rapidly damped feature that we reported previously; a weaker and more slowly damped set of oscillations is observed out at least to the 8-ps delay point. The modulations arise from resonant vibronic excitation of the BChl *a* molecules; far weaker modulations arising from non-resonant optical-Kerr-effect (OKE) excitations are observed in neat pyridine solutions under the same excitation and detection optical conditions, as was pointed out in chapter 3.⁹

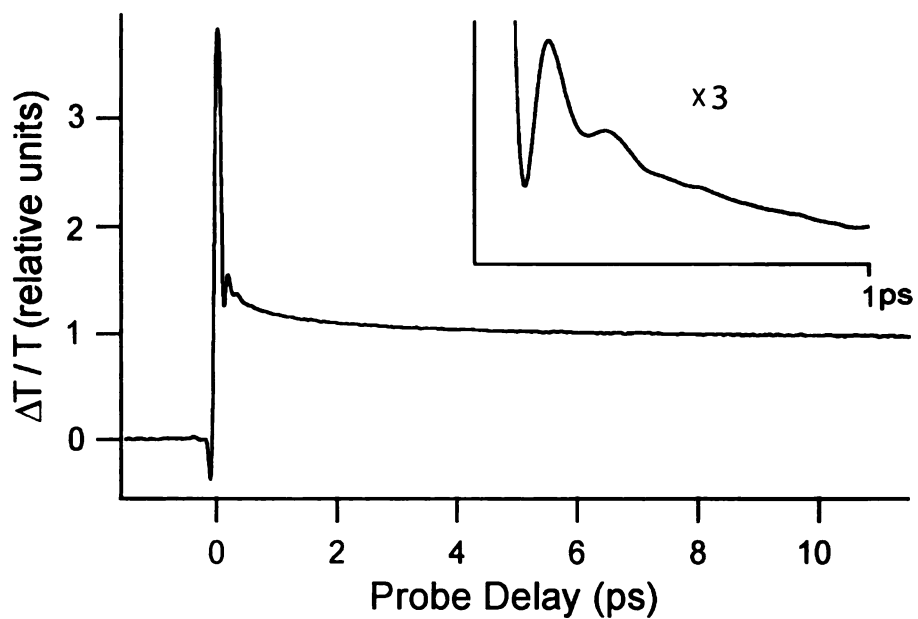


Figure 4.5. Dynamic-absorption transient from BChl in pyridine. The inset shows an expanded view of the 0–1-ps portion of the signal. The ordinate is scaled relative to the magnitude of the pump-induced change in transmission that follows the initial (0–5 ps) exponential decay arising from solvation dynamics.

In the following, we present a time-domain modeling of the rapidly damped oscillatory signals from BChl *a* in pyridine (figures 4.6 and 4.8), acetone (figure 4.9), and 1-propanol (figure 4.10). In each case, the oscillatory signal was isolated from the overall signal (such as that in figure 4.5) by subtracting a fitted triple-exponential decay function from the signal starting at 150 fs and extending to the end of the recorded range at 12 ps.

Figure 4.6 shows a series of preliminary models that attempt to describe the oscillatory signal obtained with BChl *a* in pyridine with a single modulation component.

Figure 4.6a shows that a damped 225-cm⁻¹ cosinusoid,

$$I(t) = I_0 \cos(\omega t - \phi) e^{-t/\gamma} \quad (4.1)$$

is capable of roughly describing only the first beat in the signal; the damping time ($\gamma = 92$ fs) defines a very broad Lorentzian line shape in the frequency domain ($\Delta\omega = 362$ cm⁻¹).¹⁰ The second beat in the model is significantly phase shifted with respect to that of the experimental signal, and a large deviation of the model and signal is observed at delays >400 fs.

A better description of the oscillatory signal from BChl *a* in pyridine is obtained from a distribution of damped cosinusoids,

$$I(t) = \int_0^\infty d\omega \mathcal{L}(\omega, A, \omega_0, \Delta\omega, \rho) \cos(\omega t - \phi) e^{-t/\gamma} \quad (4.2)$$

which can be implemented computationally as a sum of discrete cosinusoids (equation 4.1), as shown in figure 4.7. The intensity \mathcal{L} for a cosinusoid of frequency ω is determined here by a log-normal distribution, as parameterized by the area (A), center frequency (ω), width ($\Delta\omega$), and asymmetry ($\rho \geq 1$).¹¹ These parameters were specified as adjustable parameters in a nonlinear regression routine for the pro Fit 6.0 program; the

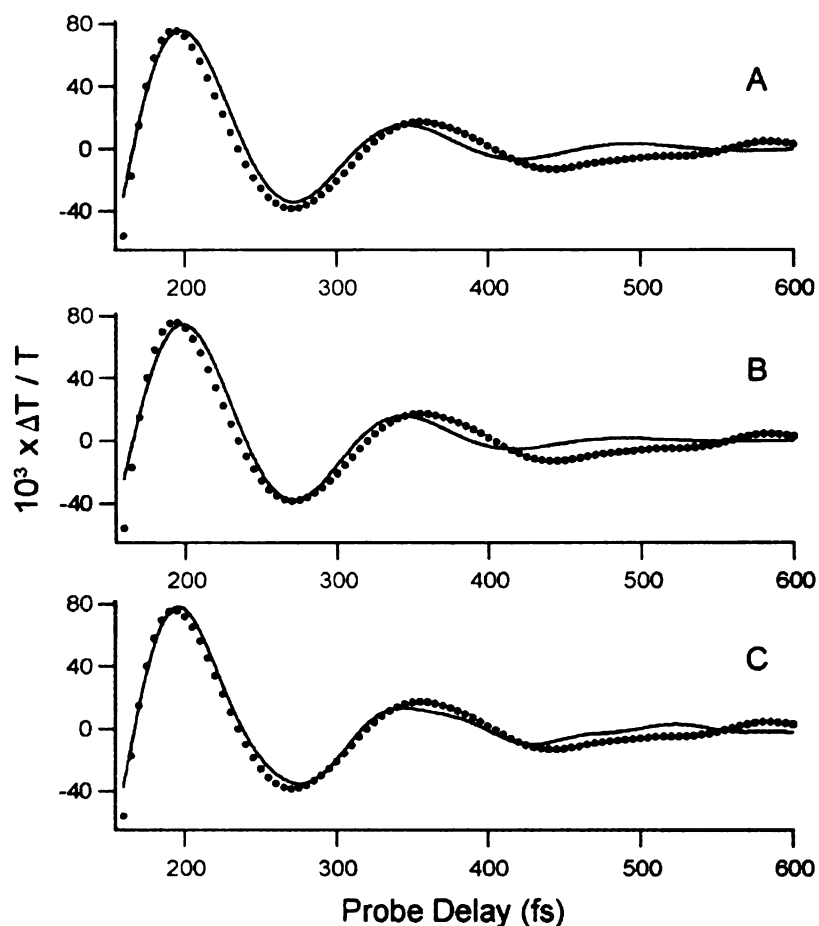


Figure 4.6. Expanded view of the rapidly damped oscillation observed in the dynamic-absorption transient from BChl *a* in pyridine (see figure 4.5) and three optimized single-modulation-component models employing different line shapes: (a) a discrete 225-cm^{-1} cosinusoid (equation 4.1) with the damping time $\gamma = 92$ fs, (b) a Gaussian distribution of damped cosinusoids with a center frequency of 225 cm^{-1} and a width (fwhm) of 50 cm^{-1} , and (c) a log-normal distribution of damped cosinusoids with a center frequency of 285 cm^{-1} and a width (fwhm) of 97 cm^{-1} . The models for (b) and (c) were defined by equation 4.2, with the distributions $\mathcal{L}(\omega)$ set as a Gaussian and as a log-normal, respectively. The scaling of the ordinate is relative to the magnitude of the pump-probe ground-state depletion signal, as indicated in figure 4.5.

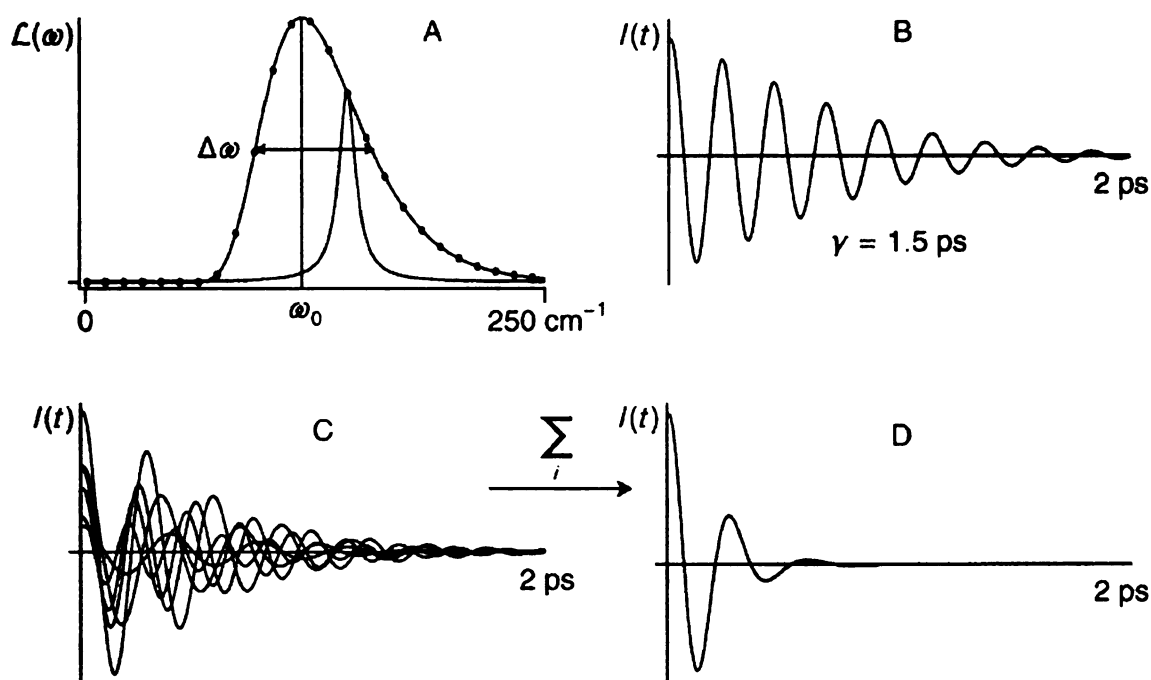


Figure 4.7. Modeling the rapidly damped vibrational coherence observed in BChl *a* solutions with a distribution of slowly damped cosinusoids, $\mathcal{L}(\omega)$, as defined by equation 4.2. A log-normal distribution $\mathcal{L}(\omega)$, (a), defined by its center frequency, ω_0 , width, $\Delta\omega$, and asymmetry (or skew), ρ , is sampled over its full width. Each sample defines the intensity of a Lorentzian line shape that corresponds in the time domain, (b), to a cosinusoid at the sampled frequency ω with a homogeneous (or intrinsic) damping time, γ , here set arbitrarily to 1.5 ps. Summing of the cosinusoids obtained by sampling over the full width of the distribution $\mathcal{L}(\omega)$, (c), results in a rapidly damped waveform, (d), that resembles the vibrational coherence observed in BChl solutions.

robust (gradient-search) optimization algorithm was employed in this work.¹² For figure 4.6b, ρ was fixed to unity in order to obtain a Gaussian line shape. In figure 4.6c, an asymmetric line shape was obtained by allowing ρ to float; in table 4.1, we use the sign of ρ to indicate whether the broader side of the optimized line shape is directed to high ($\rho > 1$) or low frequency ($\rho < 1$). The tabulated values for the area A report the integral over the distribution $\mathcal{L}(\omega)$.

$$A = \int_0^{\infty} d\omega \mathcal{L}(\omega) \quad (4.3)$$

For multicomponent models, as used below, the A values are normalized so that they sum to unity for the signal in pyridine; the A values reported for the signals in the other two solvents are normalized by the same scaling factor used for pyridine, so they report the relative modulation intensity compared to that of the signal in pyridine.

In the models shown in figure 4.6b and c, and in subsequent models employing equation 4.2 in a multicomponent model, the *intrinsic* (or *homogeneous*) damping time γ was arbitrarily fixed to 1.5 ps, in the range of the damping times for the slowly damped modulation features we observed for BChl *a* in pyridine⁹ and for the carbocyanine dye DTTCI in polar solution.⁴ The optimized fit to the oscillatory signal is not strongly dependent on the choice of γ in any case. Similar line shapes \mathcal{L} are obtained when longer damping times are specified; \mathcal{L} gets narrower as γ is shortened. The sum of discrete cosinusoids (equation 4.2) converges satisfactorily with $\gamma = 1.5$ ps when $A(\omega)$ is sampled at 5-cm⁻¹ intervals over the 1–500-cm⁻¹ range. Modulation frequencies $\omega > 500$ cm⁻¹ are not impulsively excited to a significant degree by the 60-fs pump pulses employed in the

present experiments, so the sum can be truncated at that point without any discernible impact on the fit.

While the fit obtained from the Gaussian distribution (figure 4.6b) is not clearly distinguishable from that provided by the Lorentzian line shape of the discrete cosinusoid used in figure 4.6a, the fit obtained from the asymmetric distribution (figure 4.6c) represents a significant improvement. It does a much better job of describing the first and second beats in the signal than the model employing a Gaussian distribution (figure 4.6b), but both models fail to provide an adequate description of the signal's rising trend before the first beat, at delays <200 fs. Further, all three models shown in figure 4.6 exhibit a weaker third beat, centered at the 480-fs delay point, that the experimental signal lacks. This analysis suggests that a more elaborate model, with at least two independent components and asymmetric line shapes, is required to describe the signal satisfactorily. Figure 4.8 shows that an excellent description of the oscillatory signal from BChl *a* in pyridine can be obtained from a sum of two distributions of damped cosinusoids. Both distributions were defined by equation 4.2; each was allowed to have an independent phase ϕ and asymmetry ρ . The optimized log-normal components are centered at 121 cm^{-1} and 205 cm^{-1} .

A similar analysis was performed with the oscillatory signals obtained from BChl *a* in acetone and 1-propanol solutions. Preliminary models (not shown) were obtained with single damped cosinusoids; a 251-cm^{-1} cosinusoid ($\gamma = 65$ fs; $\Delta\omega = 513\text{ cm}^{-1}$) provided the best fit to the signal in acetone while a 208-cm^{-1} cosinusoid ($\gamma = 144$ fs; $\Delta\omega = 231\text{ cm}^{-1}$) was the best fit for the signal in 1-propanol. As in pyridine, these models deviate from the observed signals beyond the first beat. Figure 4.9 shows that a sum of two

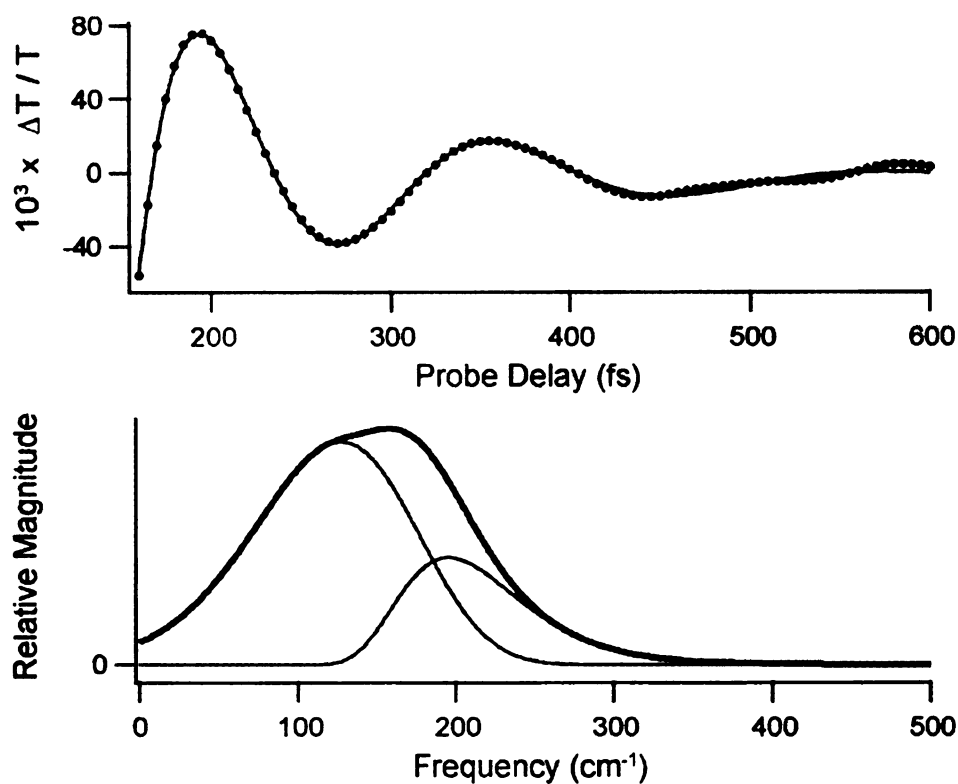


Figure 4.8. Expanded view of the rapidly damped oscillation observed in the dynamic-absorption transient from BChl *a* in pyridine (see figures 4.5 and 4.6) superimposed with a model defined by the sum of two independent log-normal distributions $\mathcal{L}(\omega)$ of damped cosinusoids, each defined by equation 4.2. The scaling of the ordinate is relative to the magnitude of the pump-probe ground-state depletion signal, as in figure 4.5. *Bottom:* Plots of $\mathcal{L}(\omega)$ for the two components observed in pyridine and their sum, $\mathcal{M}(\omega)$ (thick curve). The model parameters are provided in table 4.1.

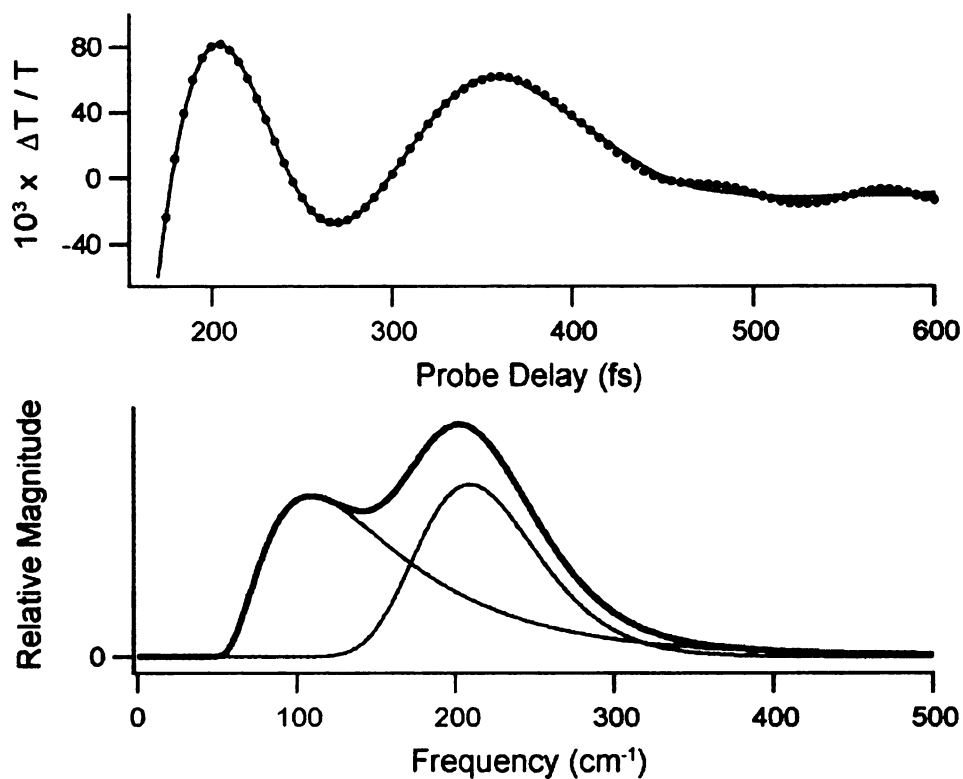


Figure 4.9. Expanded view of the rapidly damped oscillation observed in the dynamic-absorption transient from BChl *a* in acetone superimposed with a model defined by the sum of two independent log-normal distributions $\mathcal{L}(\omega)$ of damped cosinusoids, each defined by equation 4.2. The scaling of the ordinate is relative to the magnitude of the pump–probe ground-state depletion signal, as in figure 4.5. *Bottom:* Plots of $\mathcal{L}(\omega)$ for the two components observed in acetone and their sum, $\mathcal{M}(\omega)$ (thick curve). The model parameters are provided in table 4.1.

distributions of damped cosinusoids, one centered at 108 cm^{-1} and the other at 210 cm^{-1} provides a very good description of the signal from BChl *a* in acetone. This signal differs from the one observed in pyridine most obviously in having a more intense and wider second beat. The oscillatory signal observed from BChl *a* in 1-propanol can be distinguished from the ones observed in the other solvents in having four relatively strong beats on the $<800\text{-fs}$ time scale; the signals observed in pyridine and acetone have only two strong beats that are confined to the $<500\text{-fs}$ regime. Figure 4.10 shows that a sum of three distributions of damped cosinusoids is required to obtain an adequate description of the signal from BChl *a* in 1-propanol; a model with only two components (not shown) describes only the first two beats. Two of the modulation components, with distributions centered at 66 cm^{-1} and 171 cm^{-1} , are comparable to the pair observed in the other solvents. The third, a very broad distribution centered at 165 cm^{-1} , is the most intense component of the three. It is distinct in having significant intensity extending down to 0 cm^{-1} , and it exhibits almost a π shift of phase with respect to that of the other components.

The signal observed from BChl *a* in cyclohexane differs from the signals obtained in polar solvents in that there is only one strong, reproducible beat present on the $<300\text{ fs}$ time scale. Figure 4.11 shows that a sum of two distributions of damped cosinusoids is needed to describe the signal from BChl *a* in cyclohexane. The model signal arises predominantly from a broad, very low frequency component, centered at 30 cm^{-1} , that extends to 0 cm^{-1} . The weaker, second modulation component is centered at 235 cm^{-1} .

The model parameters for the rapidly damped vibrational coherence from BChl *a* observed in the four solvents are compared in table 4.1. A better sense of how the

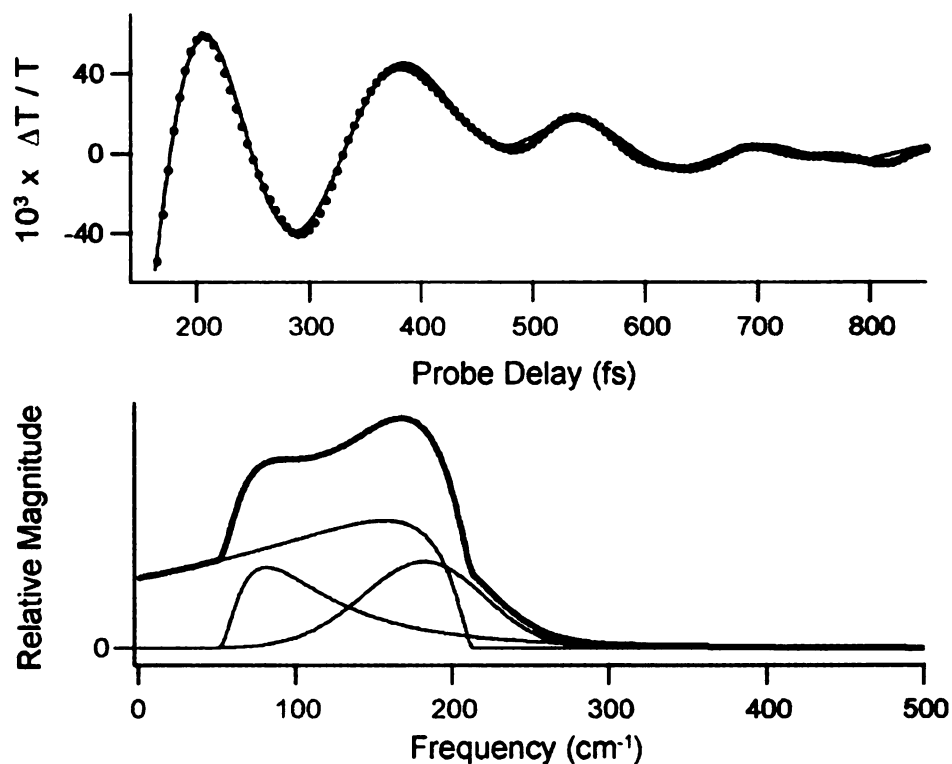


Figure 4.10. Expanded view of the rapidly damped oscillation observed in the dynamic-absorption transient from BChl *a* in 1-propanol superimposed with a model defined by the sum of three independent log-normal distributions $\mathcal{L}(\omega)$ of damped cosinusoids, each defined by equation 4.2. The scaling of the ordinate is relative to the magnitude of the pump–probe ground-state depletion signal, as in figure 4.5. *Bottom:* Plots of $\mathcal{L}(\omega)$ for the three components observed in 1-propanol and their sum, $\mathcal{M}(\omega)$ (thick curve). The model parameters are provided in table 4.1.

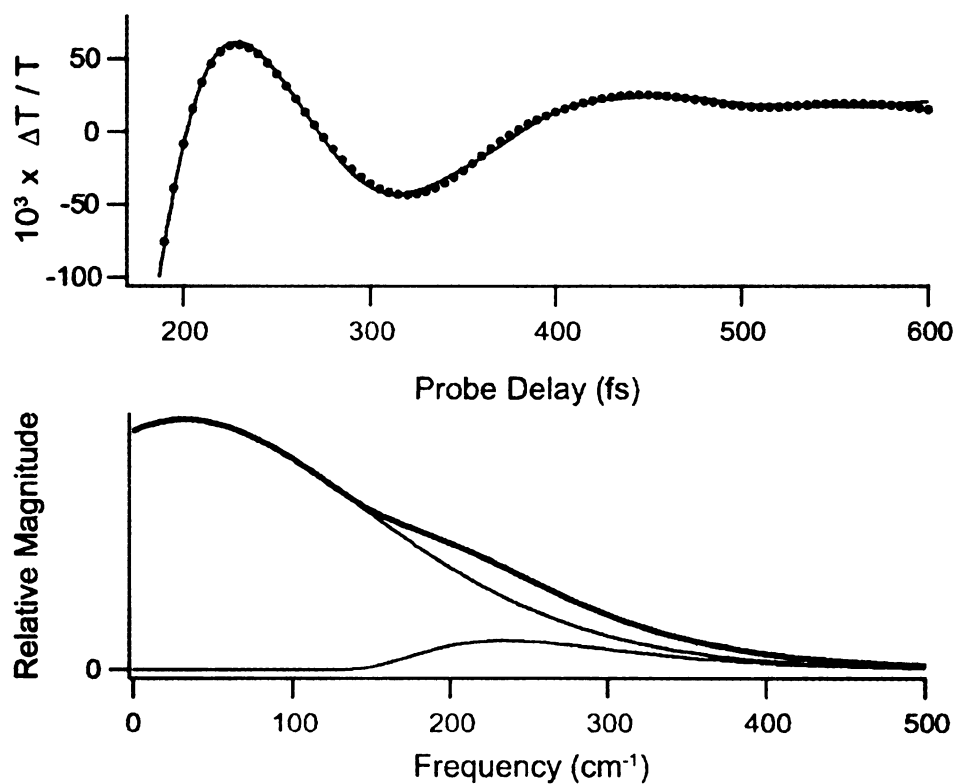


Figure 4.11. Expanded view of the rapidly damped oscillation observed in the dynamic-absorption transient from BChl *a* with a single pyridine axial ligand in cyclohexane superimposed with a model defined by the sum of two independent log-normal distributions $\mathcal{L}(\omega)$ of damped cosinusoids, each defined by equation 4.2. The scaling of the ordinate is relative to the magnitude of the pump-probe ground-state depletion signal, as in figure 4.5. *Bottom:* Plots of $\mathcal{L}(\omega)$ for the two components observed in cyclohexane and their sum, $\mathcal{M}(\omega)$ (thick curve).

Table 4.1. Model parameters for the rapidly damped vibrational coherence observed in BChl *a* solutions^a

Component	Parameter ^b	Solvent			
		Pyridine	Acetone	1-Propanol	Cyclohexane
1	ω_0 , cm ⁻¹	127	108	81	30
	$\Delta\omega$, cm ⁻¹	120	109	25	180
	ρ	-1.1	1.7	1.2	1.2
	ϕ , rad	-0.178	0.329	0.398	0.012
	A	0.725	0.326	0.095	3.027
2	ω_0 , cm ⁻¹	195	210	182	235
	$\Delta\omega$, cm ⁻¹	91	92	63	160
	ρ	1.3	1.2	-1.1	1.4
	ϕ , rad	-0.041	1.713	0.194	0.156
	A	0.275	0.0406	0.106	75.46
3	ω_0 , cm ⁻¹	—	—	165	—
	$\Delta\omega$, cm ⁻¹	—	—	426	—
	ρ	—	—	-2.4	—
	ϕ , rad	—	—	3.036	—
	A	—	—	0.263	—
Sum	$\langle\omega\rangle$, cm ⁻¹	146	189	131	123
	$\sum_i A_i$	1.000	0.732	0.465	22.94
Dipole moment ^c	μ , Debye	2.19	2.88	1.68	~0

^a Figures 4.8–4.11

^b See equations 4.2–4.5 and the text.

^c gas phase dipole moment¹⁸

vibrational coherence depends on the choice of solvent can be obtained from an analysis of the mean frequency of the fitted distributions,

$$\langle \omega \rangle = \frac{\int_0^{\infty} d\omega \mathcal{M}(\omega) \omega}{\int_0^{\infty} d\omega \mathcal{M}(\omega)} \quad (4.4)$$

with the integral calculated over the ω axis with the sum of the distributions $\mathcal{L}_i(\omega)$ from the two or three components.

$$\mathcal{M}(\omega) = \sum_i \mathcal{L}_i(\omega) \quad (4.5)$$

Table 4.1 also shows that the dipole moment of the solvent scales with the mean frequency of the fitted distribution. The trend shows that part of the $\langle \omega \rangle$ dependence is on the dipole moment. However, the large amplitudes of the individual components as well as the sum of the distributions for BChl in cyclohexane, compared to those from the other three solvents, suggest that a large part is apparently independent of the dipole moment and indicates some dependency on the polarizability of the solvent.

4.3 Discussion

The results presented in this chapter show that resonant impulsive excitation of the lowest $\pi \rightarrow \pi^*$ transition of BChl *a* is followed by a rapidly damped coherent vibrational motion of the surrounding solvent molecules. As shown in figure 4.4, the tuning of the pump-laser spectrum and the transmitted probe band width favors detection of coherent wave-packet motion on the ground-state potential-energy surface. The wave packets are prepared and launched on the ground-state surface by the resonant impulsive stimulated Raman scattering (RISRS) mechanism,¹³ so we know that the vibrational modes that contribute to the modulated signal are those with coordinates that are displaced from the

ground-state equilibrium geometry in the BChl a π^* electronic excited state.¹⁴ In short, we conclude that the rapidly damped vibrational coherence arises from solvent–BChl *intermolecular* modes that are coupled to the BChl $\pi \rightarrow \pi^*$ transition. To our knowledge, this work represents the first direct observation of resonance-Raman activity involving intermolecular vibrational modes between solvent molecules and large electronic chromophores. The assignment of the vibrational coherence to intermolecular modes between BChl and clustered solvent molecules in the first solvation shell is supported by the fact that the mode frequency scales with the dipole moment of the polar solvent, as shown in table 4.1.

4.3.1 Structural Assignments

We are aware of only a few attempts to detect intermolecular modes in condensed phases using resonance-Raman spectroscopy in the frequency domain. Mathies and coworkers observed resonance-Raman active modes from alcohol¹⁵ and water¹⁶ solutions of the solvated electron. The solvated electron is a diffuse structure that makes a significant ground-to-excited-state change in size and shape;¹⁷⁻²¹ it apparently interacts strongly enough with a number of molecules in its first solvation shell that the absorption transition is vibronically coupled to a number of solvent intramolecular modes.^{15,16} The lowest frequency Raman-active modes observed in water, at 110 cm^{-1} , are assigned to the intermolecular hindered translational modes between the electron and molecules in the first solvation shell.¹⁶ In contrast, Waterland and Kelley²² did not observe features from intermolecular modes in their UV resonance-Raman studies of the nitrate ion in several solvents, but the π -electron density of the nitrate ion is highly localized. A similar

localization is probably responsible for the lack of detection of intermolecular modes in the femtosecond pump-probe studies of the cyanide-bridged Ru(II,III) mixed-valence complex by Barbara and coworkers.²³ Significant solvent dependences were noted in the intervalence charge-transfer rate and in the damping of the ground-state vibrational coherence, but no solvent-dependent modulation components were directly observed.

A consideration of this background makes it seem reasonable to suggest that $\pi \rightarrow \pi^*$ transitions in chromophores with delocalized π -electron density, such as the chlorophylls and porphyrins, might exhibit vibronic coupling to intermolecular modes with the small number of first-shell solvent molecules that are *clustered*^{24,25} with it owing to specific structural interactions. Displacement of the intermolecular mode would be mediated by a change in the shape and extent of the π -electron density owing to the $\pi \rightarrow \pi^*$ change in electron configuration. Note that similar mode displacements might be driven by electron-transfer reactions since the redox-active electrons are usually associated with the frontier molecular orbitals. The semicontinuum theory for electron transfer reactions described by Mikkelsen and Ratner²⁶⁻²⁸ involves a comparable structural picture: a small number of clustered solvent molecules in the first solvation shell surrounded by a dielectric continuum.

We suggest that the resonance-Raman active solvent-mode interactions with BChl *a* involve an attack by a solvent dipole on the π -electron density above and below the plane of the macrocycle. These interactions might resemble those in liquid pyrrole, where the protons of one pyrrole molecule make a perpendicular attack on the π -electron density of an adjacent molecule,²⁹ yielding intermolecular modes in the 100-cm⁻¹ region.³⁰ Evidence for this configuration in the BChl-solvent interaction is obtained from

molecular mechanics calculations.

Figure 4.12 presents a possible model for the interaction between two non-ligated pyridine solvent molecules and the π -electron density of the BChl macrocycle in the dipyrindine complex. The model was obtained using a molecular mechanics calculation with the PCModel³¹ program and the MMX force field. The MMX force field³¹ adds parameters to the well known MM2 force field^{32,33} to permit modeling of inorganic complexes such as those containing first-row transition metals. The calculation began with an optimized structure for a single, isolated BChl molecule. Then, two pyridine molecules were coordinated to axial binding sites on the central Mg(II) ion. The energy of the resulting structure was then minimized. Lastly, two additional non-ligated pyridines were then added at a distant position relative to the BChl macrocycle. Figure 4.12 shows the typical result of minimizing the energy of the resulting system. The non-ligated pyridines attack the π -electron density on either face of the macrocycle and apparently π -stack with the axially ligated pyridines. Similar configurations were obtained with a wide range of starting configurations for the non-ligated pyridines. The final T-shaped configuration of the non-ligated pyridines resemble configurations in neat pyridine,²⁹ and there is a similar motif in benzene crystals.^{34,35}

Figure 4.13 illustrates the possible interaction between acetone solvent dipoles and the π -electron density of the BChl macrocycle. The interaction was modeled using the same sequence of molecular mechanics calculations as described above.

The observation of more than just a single mode distribution, however, evidences two (or three, in 1-propanol) configurations or sites for the solvent molecules clustered around the BChl macrocycle. Owing to doming of the axially coordinated Mg(II) ion out

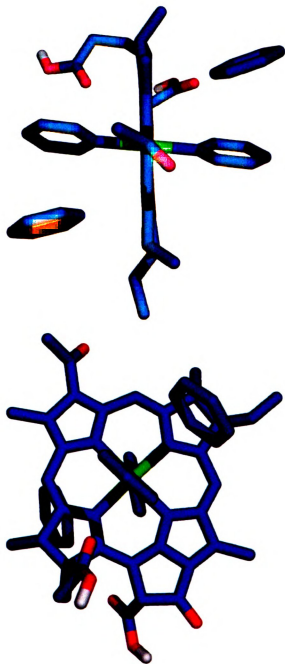


Figure 4.12. A possible model obtained using a molecular mechanics calculation with the MMX force field and the PCModel³¹ program for the interaction between two non-ligated pyridine solvent molecules and the π -electron density of the BChl macrocycle in the dipyrindine complex.

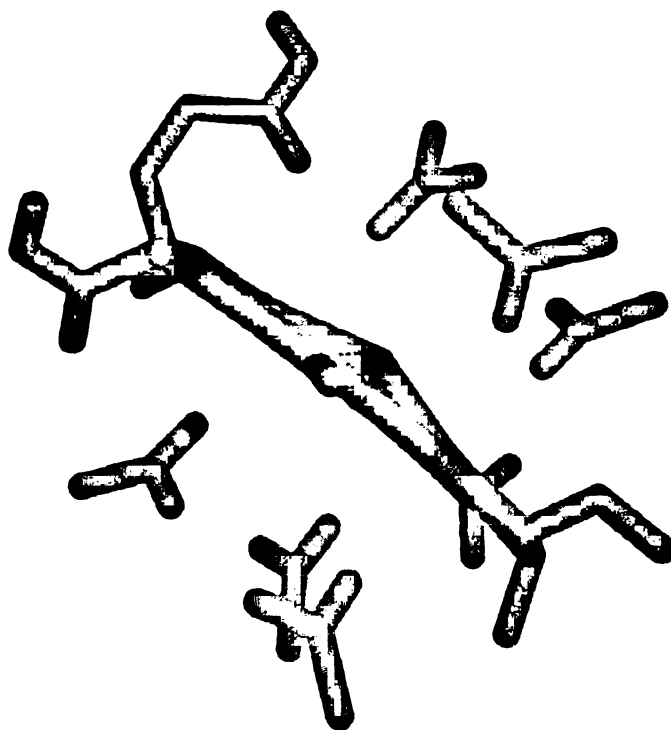


Figure 4.13. A possible model obtained using a molecular mechanics calculation with the MMX force field and the PCModel³¹ program for the interaction between acetone solvent dipoles and the π -electron density of the BChl macrocycle.

of the plane of the coordinating pyrrolic nitrogens, the two faces of the BChl macrocycle present distinct π -electron surfaces that might be assigned to the two solvent-binding sites. Even in the six-coordinate BChl *a* complexes observed in pyridine and 1-propanol, it is likely that the Mg(II) ion is still domed so that it favors the attack of one of its two solvent-derived axial ligands. Consider that the back-side attack of the sixth solvent-derived axial ligand involves a longer reach to the Mg(II) ion, so two well-resolved binding equilibria for the axial ligands are observed.² A consequence of the doming that is certainly relevant to the interaction of the *non-ligated* solvent molecules with the π -electron density is the resulting tilting of the dipole moment out of the plane of the BChl macrocycle.

The model for the signal in 1-propanol (see figure 4.10) is dominated by a very broad feature that extends all the way to 0 cm^{-1} that is not observed in the other two solvents (see figures 4.8 and 4.9). We suggest that this very low-frequency character arises from hydrogen-bonded chains³⁶⁻³⁹ of 1-propanol molecules that are coupled to a given BChl macrocycle. This assignment is made in analogy to the *collective* modes in certain liquids that contribute to OKE signals in the $< 20 \text{ cm}^{-1}$ regime.^{40,41} As in the other solvents, clustered 1-propanol molecules in the first solvation shell interact directly with the π -electron density of the BChl macrocycle, but the extended tail of the line shape down to 0 cm^{-1} reflects the presence of hydrogen-bonded chains of various lengths that are linked to the attacking molecules. It follows that the vibrational coherence observed in pyridine and acetone solvents lacks such an ultra-low-frequency character because these solvents lack the ability to form intermolecular hydrogen bonds that would promote formation of chains of molecules.

4.3.2 Line Shapes For Intermolecular and Intramolecular Modes in Solution and Proteins

The time domain resonance-Raman methods used in the present work are uniquely capable of detecting intermolecular modes in delocalized π -electron systems because the line shapes would be expected to be broad owing to structural disorder in the chromophore–solvent interaction. Similar line shapes are observed in *nonresonant* OKE experiments in neat liquids,^{40,42,43} but we stress again that the Raman-active modes detected in the present experiments arise from *resonant* excitation of the electronic chromophore. In the frequency domain, broad low-frequency Raman line shapes arising from inhomogeneously broadened features are not easily discerned from the baseline. In the time domain, however, the same line shapes result in sharp, rapidly damped features in the vibrational coherence, and the broad line shapes can be resolved into components on the basis of their distinct *phases*. A time-domain analysis, such as the one based on distribution functions used in the present work, is essential if reasonable models for the vibrational coherence are sought. A conventional Fourier-transform analysis of the rapidly damped modulations returns line shapes in the frequency domain that are usually distorted owing to the truncation of the waveform at zero time, the individual components are resolved spectrally, so it is difficult to obtain reliable information on the phases of the individual components. Further, the demonstration in this work that the line shapes for the intermolecular modes are asymmetric argues against the use of conventional linear-prediction, singular-value decomposition methods, which are usually based on an assumption that the signal can be described by a discrete sum of a small number of damped cosinusoids.

As noted in chapter 3, the rapidly damped vibrational coherence observed in BChl *a*

in pyridine exhibits a much stronger signal in the time domain than is associated with the slowly damped vibrational coherence that extends to the 8-ps delay point. We assign the slowly damped signals to vibrational modes that are predominantly *intramolecular* in character, involving mostly motions of the BChl macrocycle only. These modes are essentially homogeneously broadened or less strongly inhomogeneously broadened. The damping time of these signals is relatively long because the line shape is narrow in the frequency domain, which reflects a relatively narrow range of geometries for the associated oscillator. We report here that the slowly damped vibrational coherence was too weak to be observed in the acetone and 1-propanol solutions. The most likely explanation for this observation involves axial coordination of pyridine molecules to the Mg(II) ion and an associated distortion of the BChl macrocycle. This distortion apparently mixes some of the strong Raman activity in the plane of the macrocycle into the low-frequency, out-of-plane modes that are visible in the $<300\text{-cm}^{-1}$ regime. Bocian and coworkers have previously reported that the axial coordination of the Mg(II) ion is related to the activity of the out-of-plane deformation modes that are observed in the $< 200\text{ cm}^{-1}$ -regime.⁴⁴⁻⁴⁷ It is likely that the axially-ligated acetone and 1-propanol molecules cause a much smaller distortion of the BChl macrocycle and a much lower degree of mixing of activity into the out-of-plane deformations, rendering the slowly damped vibrational coherence associated with these modes too weak to be observed under our conditions.

4.4 References

- (1) Katz, J.; Strain, H.; Leussing, D.; Dougherty, R. *J. Am. Chem. Soc.* **1968**, *90*, 784–791.
- (2) Evans, T.; Katz, J. *Biochim. Biophys. Acta* **1975**, *396*, 414–426.
- (3) Shipman, L.; Cotton, T. M.; Norris, J. R.; Katz, J. *J. Am. Chem. Soc.* **1976**, *98*, 8222–8230.
- (4) Carson, E. A.; Diffey, W. M.; Shelly, K. R.; Lampa-Pastirk, S.; Dillman, K. L.; Schleicher, J. M.; Beck, W. F. *J. Phys. Chem. A* **2004**, *108*, 1489–1500.
- (5) Balk, M. W.; Fleming, G. R. *J. Chem. Phys.* **1985**, *83*, 4300–4307.
- (6) Engh, R. A.; Petrich, J. W.; Fleming, G. R. *J. Phys. Chem.* **1985**, *89*, 618–621.
- (7) Joo, T.; Jia, Y.; Yu, J.-Y.; Lang, M. J.; Fleming, G. R. *J. Chem. Phys.* **1996**, *104*, 6089–6108.
- (8) Cong, P.; Deuhl, H. P.; Simon, J. D. *Chem. Phys. Lett.* **1993**, *211*, 367–373.
- (9) Shelly, K. R.; Carson, E. A.; Beck, W. F. *J. Am. Chem. Soc.* **2003**, *125*, 11810–11811.
- (10) McHale, J. L. *Molecular Spectroscopy*; Prentice Hall: Upper Saddle River, New Jersey, 1999.
- (11) Siano, D. B.; Metzler, D. E. *J. Chem. Phys.* **1969**, *51*, 1856–1861.
- (12) *pro Fit 6.0*; QuantumSoft: Uetikon am See, Switzerland.
- (13) Yan, Y.-X.; Cheng, L.-T.; Nelson, K. A. In *Advances in Non-linear Spectroscopy*; Clark, R. J. H., Hester, R. E., Eds.; John Wiley & Sons: Chichester, England, 1988, p 299–355.
- (14) Myers, A. B.; Mathies, R. A. In *Biological Applications of Raman Spectroscopy*; Spiro, T. G., Ed.; Wiley-Interscience: New York, 1987; Vol. 2, *Resonance Raman Spectra of Polyenes and Aromatics*, p 1–58.
- (15) Tauber, M. J.; Stuart, C. M.; Mathies, R. A. *J. Am. Chem. Soc.* **2004**, *126*, 3414–3415.
- (16) Tauber, M. J.; Mathies, R. A. *Chem. Phys. Lett.* **2002**, *354*, 518–526.

- (17) Alfano, J. C.; Walhout, P. K.; Kimura, Y.; Barbara, P. F. *J. Chem. Phys.* **1993**, *98*, 5996-5998.
- (18) Kimura, Y.; Alfano, J. C.; Walhout, P. K.; Barbara, P. F. *J. Phys. Chem.* **1994**, *98*, 3450-3458.
- (19) Reid, P. J.; Silva, C.; Walhout, P. K.; Barbara, P. F. *Chem. Phys. Lett.* **1994**, *228*, 658-664.
- (20) Walhout, P. K.; Alfano, J. C.; Kimura, Y.; Silva, C.; Reid, P. J.; Barbara, P. F. *Chem. Phys. Lett.* **1995**, *232*, 135-140.
- (21) Silva, C.; Walhout, P. K.; Reid, P. J.; Barbara, P. F. *J. Phys. Chem. A* **1998**, *102*, 5701-5707.
- (22) Waterland, M.; Myers Kelley, A. *J. Chem. Phys.* **2000**, *113*, 6760-6773.
- (23) Kambhampati, P.; Son, D. H.; Kee, T. W.; Barbara, P. F. *J. Phys. Chem. A* **2000**, *104*, 10637-10644.
- (24) Jortner, J. Z. *Phys. D – Atoms, Molecules, and Clusters* **1992**, *24*, 247-275.
- (25) Spence, T. G.; Trotter, B. T.; Burns, T. D.; Posey, L. A. *J. Phys. Chem. A* **1998**, *102*, 6101-6106.
- (26) Mikkelsen, K. V.; Ratner, M. A. *J. Chem. Phys.* **1989**, *90*, 4237-4247.
- (27) Mikkelsen, K. V.; Ratner, M. A. *J. Phys. Chem.* **1989**, *93*, 1759-1770.
- (28) Billing, G. D.; Mikkelsen, K. V. *Advanced Molecular Dynamics and Chemical Kinetics*; John Wiley & Sons: New York, 1997.
- (29) Gamba, Z.; Klein, M. L. *J. Chem. Phys.* **1990**, *92*, 6973-6974.
- (30) Wynne, K.; Galli, C.; Hochstrasser, R. M. *Chem. Phys. Lett.* **1992**, *193*, 17-22.
- (31) *PCMODEL 8.0*; Serena Software: Bloomington, IN.
- (32) Allinger, N. J. *J. Am. Chem. Soc.* **1977**, *99*, 8127-8134.
- (33) Allinger, N. J.; Kok, R. A.; Imam, M. R. *J. Comp. Chem.* **1988**, *9*, 591-595.
- (34) Cox, E.; Cruickshank, D.; Smith, J. *Proc. R. Soc. A* **1958**, *247*, 1-21.
- (35) Bacon, G.; Curry, N.; Wilson, S. *Proc. R. Soc. A* **1964**, *279*, 98-110.

- (36) Garg, S. K.; Smyth, C. P. *J. Phys. Chem.* **1965**, *69*, 1294–1301.
- (37) Jorgensen, W. L. *J. Am. Chem. Soc.* **1980**, *102*, 543–549.
- (38) Bertolini, D.; Cassettari, M.; Salvetti, G. *J. Chem. Phys.* **1983**, *78*, 365–372.
- (39) Sumi, H.; Marcus, R. A. *J. Chem. Phys.* **1986**, *84*, 4272–4276.
- (40) Lotshaw, W. T.; McMorro, D.; Thantu, N.; Melinger, J. S.; Kitchenbaum, R. *J. Raman Spect.* **1995**, *26*, 571–583.
- (41) Lotshaw, W. T.; Staver, P. R.; McMorro, D.; Thantu, N.; Melinger, J. S. In *Ultrafast Phenomena IX*; Barbara, P. F., Knox, W. H., Mourou, G. A., Zewail, A. H., Eds.; Springer-Verlag: Berlin, 1994, pp 91–92.
- (42) McMorro, D.; Lotshaw, W. T. *Chem. Phys. Lett.* **1993**, *201*, 369–376.
- (43) McMorro, D.; Lotshaw, W. T. *J. Phys. Chem.* **1991**, *95*, 10395–10406.
- (44) Palaniappan, V.; Aldema, M. A.; Frank, H. A.; Bocian, D. F. *Biochemistry* **1992**, *31*, 11050–11058.
- (45) Czarnecki, K.; Diers, J. R.; Chynwat, V.; Erickson, J. P.; Frank, H. A.; Bocian, D. F. *J. Am. Chem. Soc.* **1997**, *119*, 415–426.
- (46) Thompson, M. A.; Zerner, M. C.; Fajer, J. *J. Phys. Chem.* **1990**, *94*, 3820–3828.
- (47) Thompson, M. A.; Zerner, M. C.; Fajer, J. *J. Phys. Chem.* **1991**, *95*, 5693–5700.

CHAPTER 5

VIBRATIONAL COHERENCE FROM BACTERIOCHLOROPHYLL IN THE LIGHT HARVESTING SUBUNITS B777 AND B820

5.0 Introduction

The photosynthetic purple non-sulfur bacteria usually contain two types of integral membrane complexes, a core light harvesting complex and a peripheral light harvesting complex.¹ The light-harvesting complex 1 (LH1) is known as the core complex that surrounds a single reaction center. A model of LH1 is shown in figure 5.1.^{2,3} LH1 is surrounded by several copies of a ring-shaped peripheral complex known as light-harvesting complex 2 (LH2), figure 5.2.^{2,3} Energy absorbed by LH2 is transferred to the adjacent LH1 complex and then to the reaction center. Loach *et al.*^{4,5} and van Grondelle and coworkers^{6,7-11} have shown that LH1 can be reversibly dissociated into its subunits by detergent solubilization. The B820 subunit consists of a pair of α helices sandwiching a strongly coupled pair of histidine-ligated BChl molecules^{12,13} Van Grondelle and coworkers⁶⁻¹¹ have provided evidence that the strongly coupled pair of BChl *a* molecules held by the B820 subunit are arranged analogously to the pair of BChl in the LH2 structure.¹⁴

In this work, we employ B820 as a limited model for the primary electron donor, P, in the photosynthetic reaction center. B820 allows us to study the electronic properties of a bacteriochlorophyll dimer in the absence of energy transfer to or from adjacent subunits or electron transfer to adjacent acceptors, as in the photosynthetic reaction center. A model for B820, as shown in figure 5.3, was obtained by Hu and Schulten¹⁵ using

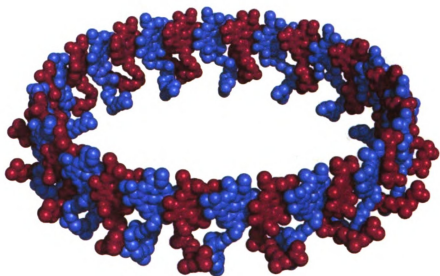


Figure 5.1. Model of the LHI light-harvesting complex from the calculations of Schulten and coworkers.¹⁵ Only the chromophores are shown here. (Refer to figure 5.3 for the details of how each pair of BChl are organized by a pair of membrane-separating α helices.)





Figure 5.2. Crystal structure of the LH2 complex from *Rhodospseudomonas acidophila* as reported by Caffrey and coworkers.¹⁶ The α and β units are shown in red and blue, respectively, the B800 pigments in purple, the B850 pigments in green, and the carotenoids in yellow. The structure can be found under the accession number 2FKW in the RCSB Protein Data Bank.

parameters from the LH1 projection map obtained from electron microscopy¹⁷ and from the LH2 crystal structure. The distance between the Mg(II) ions is 9.2 Å; the plane-to-plane distance between the two macrocycles is 3.6 Å.¹⁸ In comparison, the pair of BChl in P is more closely spaced; the distance the Mg(II) ions is 7.6 Å; the plane-to-plane distance between the two macrocycles is 3.3 Å.¹⁹

Van Grondelle and coworkers⁶⁻¹¹ have extensively characterized the spectroscopic properties of the pair of BChl *a* molecules held by the B820 subunit. At high detergent concentrations, the B820 complex reversibly falls apart and produces the subunit B777, shown in figure 5.4.^{5,14} B777 consists of one α helix ligated to a single BChl molecule. We used B777 to study the protein-bound monomeric chlorophyll system in order to discern effects from the formation of the BChl dimer in B820.

5.1 Experimental Procedures

5.1.1 Sample Preparation

Rhodospirillum rubrum G9 was obtained as a lyophilized pellet from the American Type Culture Collection. It was grown in three-liter carboys under low-intensity incandescent light (one 60 W bulb at a distance of 1 foot) in the presence of 5% CO₂/95% N₂ in modified Hutner's medium, as described by Cohen-Bazire *et al.*²⁰ Cells were harvested by centrifugation at 5000 x g for 5 min in a Sorvall GSA rotor; the cells were stored at -10° C in the dark as pellets in the growth medium. Chromatophores were isolated from whole cells by a series of steps involving sonication and ultracentrifugation as described by Loach and coworkers,^{4,21} the benzene extraction step was not required because G9 is a carotenoidless mutant. The chromatophores were

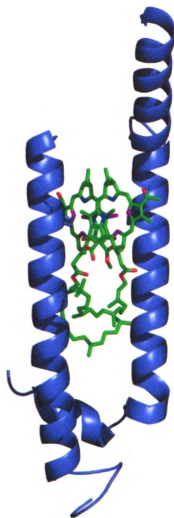


Figure 5.3. Model of the B820 subunit from LH1 from the calculations of Schulten and coworkers.¹⁵

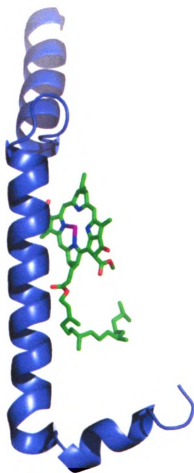


Figure 5.4. Possible model for the B777 subunit formed by solubilization of the B820 subunit of LH1. LH1 is the result of dissociating B820 into two polypeptides, each with a single ligated BChl macrocycle, so there are two possible B777 structures in a given sample.

stored in 0.1 M HEPES (4-(2-hydroxyethyl)-1-piperazineethanesulfonic acid) buffer solution at pH 7.5 at -20° C for up to 1 week prior to use.

5.1.1.1 Isolation and Preparation of B820 Subunits

Initial experiments were performed with B820 subunits prepared using the detergent *n*-octyl-*rac*-2,3-dipropyl sulfoxide (ODPS, Bachem) as described by Visschers and coworkers.⁷ However, as shown in figure 5.5, the isolation of B820 using ODPS was somewhat unsuccessful in this laboratory. Figure 5.5 shows the absorption spectra of chromatophores isolated from *R. rubrum* G9 following the addition of various ODPS detergent concentrations. A 1.0% (w/v) solution of ODPS was added to a suspension of chromatophores in order to prepare B820 subunits. Figure 5.6 shows that, while a large amount of B820 is present, as judged from the absorption band at 820 nm, but there is still a substantial amount of undissociated chromatophores present, which exhibit an absorption maximum at 873 nm. In addition to the formation of B820, a small shoulder can be observed at 777 nm due to the initial formation of B777 subunits.

Subsequent experiments employed preparations of B820 that were prepared according to the procedure of Miller *et al.*⁴ B820 subunits were isolated from the chromatophore preparations by solubilization with the detergent octyl β -D-glucopyranoside (OG, Bachem). To a suspension of chromatophores, OG was added to establish a ~0.75% (w/v) solution while monitoring the absorbance at 820 nm. Figure 5.6 shows the gradual shift of the absorbance maximum from 873 nm to 820 nm that occurs over a period of 17 hours. Small additions of OG solution were then added to ensure that no further change in absorbance at 820 nm was detected. Unlike

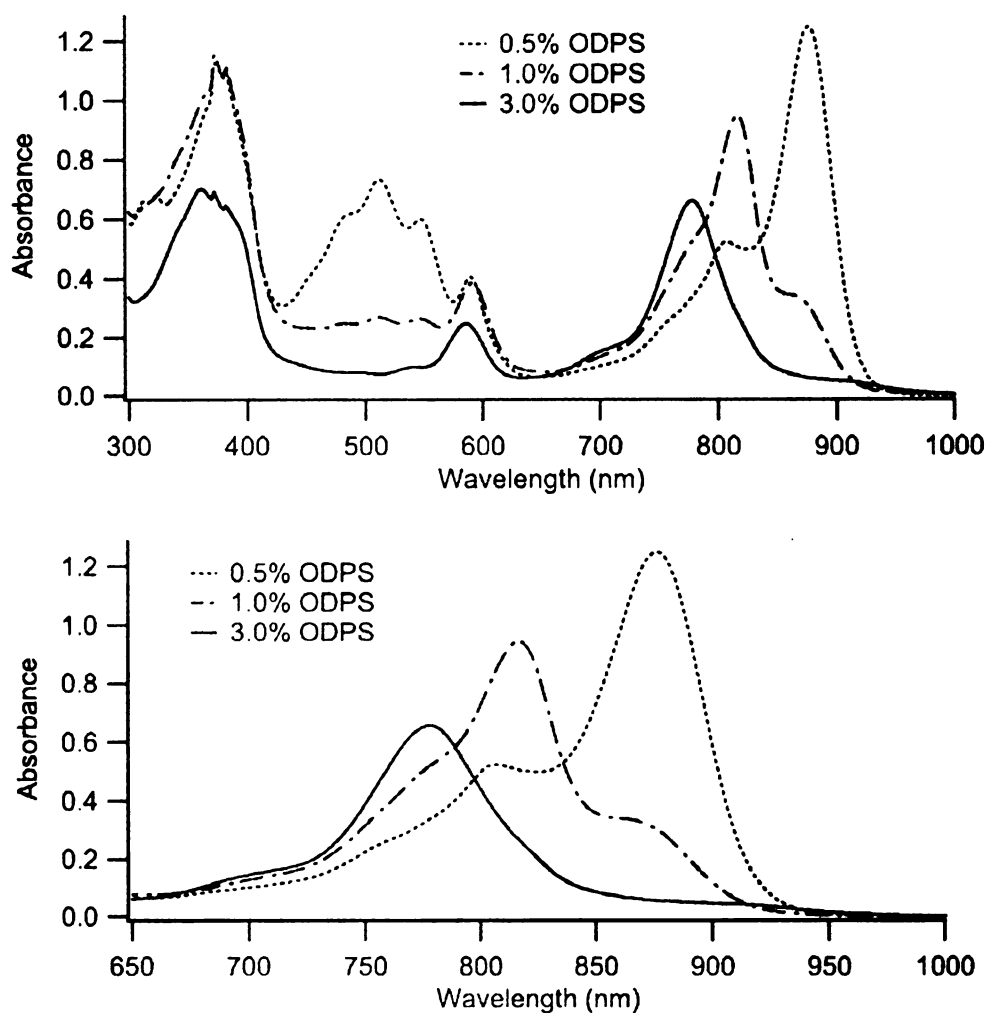


Figure 5.5. Absorption spectra illustrating the formation of B777 subunits from detergent-solubilized chromatophores isolated from *R. rubrum* G9, top panel. At low concentrations of *n*-octyl-*rac*-2,3-dipropyl sulfoxide (ODPS), only the chromatophores are present, as indicated by the absorption maximum at 873 nm. At intermediate detergent concentrations, chromatophores, B820 subunits, and B777 subunits are simultaneously present within the sample. The B820 population is indicated by the formation of the absorption peak at 820 nm. B777 subunits are exclusively present in the presence of an increased concentration of ODPS detergent (~3.0% (w/v)). The bottom panel shows an expanded view of the Q_y absorption band so that the conversion of the initial 870 nm peak to the 777 nm peak can be more easily observed.

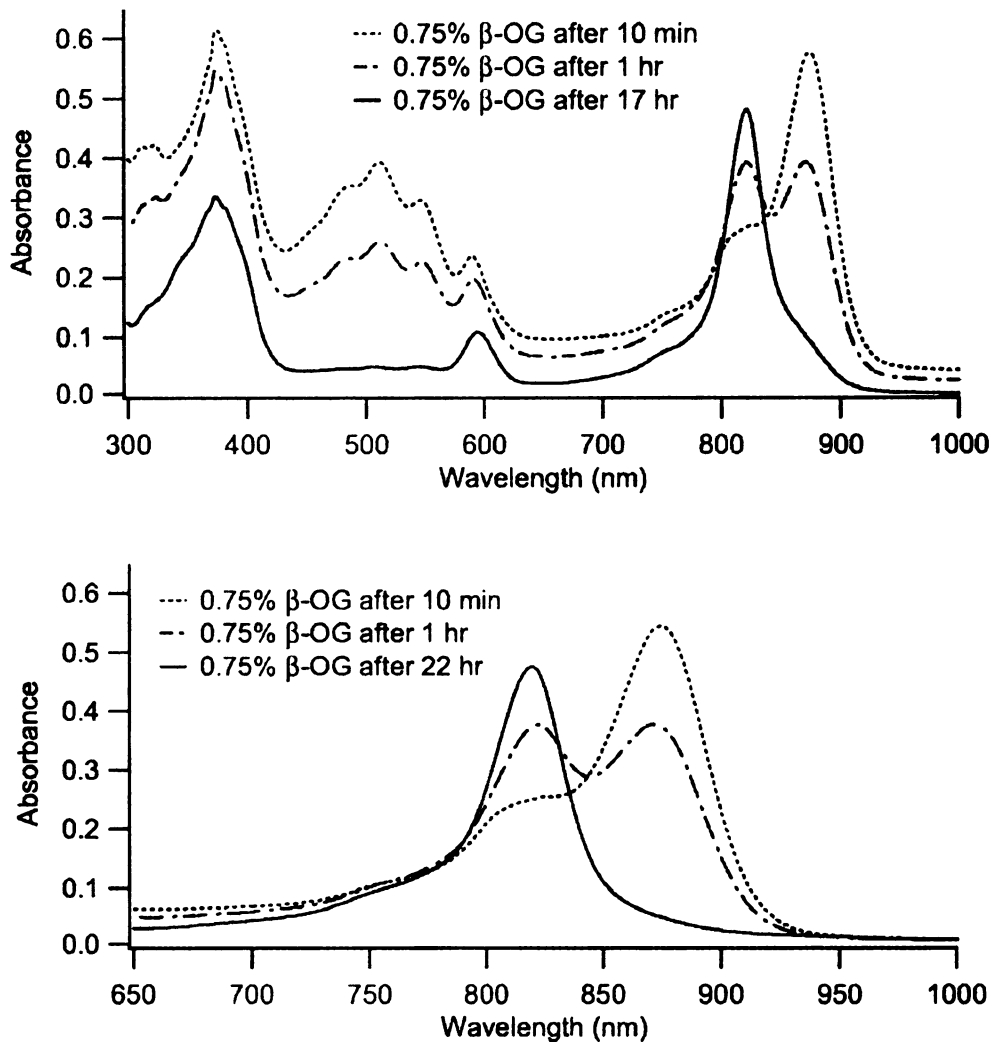


Figure 5.6. Absorption spectra illustrating the formation of B820 subunits from detergent-solubilized chromatophores isolated from *R. rubrum* G9 over a period of 17 hours, top panel. The chromatophores were solubilized with 0.75% (w/v) octyl β -D-glucopyranoside (OG). The bottom panel shows an expanded view of the Q_y absorption band. No chromatophores are present in the sample 22 hours after the addition of OG solution.

chromatophores treated with ODPS detergent, where an equilibrium between B777 and B820 is maintained even at fairly high detergent concentrations, chromatophores treated with OG yield only B820 subunits.

5.1.1.2 Isolation and Preparation of B777 Subunits

B777 subunits were prepared by the addition of ODPS to a suspension of chromatophores until the concentration of ODPS was ~3.0 % (w/v). Additional ODPS was added until no change in absorbance at 777 nm occurred and no visible peak at 820 from unsolubilized B820 was observed. The gradual formation of B777 from chromatophores is shown in figure 5.5. ODPS, rather than OG, was used in the preparation of B777 because it was not possible to drive the equilibrium completion to the B777 form in the presence of OG under our conditions. Again, all steps were conducted in the dark at room temperature (22 °C).

5.1.2 Continuous-Wave Spectroscopy

Continuous-wave absorption and fluorescence spectra for all samples were acquired at room temperature with Hitachi U-2000 and Hitachi F-4500 spectrometers, respectively. The fluorescence intensities were corrected as described in chapter 3.

5.1.3 Femtosecond Spectroscopy

Dynamic-absorption spectroscopy was performed with the femtosecond pump-probe spectrometer described in chapter 2, consisting of a self-mode-locked ti:sapphire oscillator and a rapid-scanning Mach-Zehnder interferometer. The output spectrum emitted by the oscillator exhibited a band width of 12 nm. The spectrum was centered at

818 nm for experiments performed on B820 in OG and 750 nm for experiments performed on B777 in ODPS. Extracavity compression employed a pair of SF10 prisms, which were adjusted to produce 60-fs pulses (sech^2) in all experiments. Probe light for experiments done on B820 was detected at 818 nm (2-nm band pass) and 757 nm (2-nm band pass) for experiments done on B777.

B820 and B777 samples for femtosecond spectroscopy were held at room temperature (22 °C) in a 1-mm fused-silica flow cuvette. Samples were circulated using a peristaltic pump through the cuvette at a rate of 5 mL/min. The absorption spectrum of the sample was monitored throughout the duration of the experiment for changes arising from photochemistry or permanent photobleaching.

5.2 Results

5.2.1 Continuous-Wave Spectroscopy

Figures 5.7 and 5.8 show the absorption and fluorescence spectra exhibited by B820 in OG and B777 in ODPS, respectively, at room temperature. The spectra are plotted as $A(\nu)/\nu$ and $F(\nu)/\nu^3$, respectively, with normalization to unit area. As plotted, the sum of the spectra can be compared to the time-integrated dynamic-absorption spectrum in the weak-field limit.²² The 0–0 vibronic transition in B820 occurs in the vicinity of 11900 cm^{-1} (840 nm), where the two normalized spectra cross. Also shown in figure 5.7 is the intensity spectrum from the ti:sapphire laser that was the source of pump and probe pulses in the dynamic-absorption experiments. The intensity spectrum, centered at $\sim 820 \text{ nm}$, was tuned away from the stimulated emission to favor detection of ground-state vibrational coherence prepared by resonant impulsive stimulated Raman scattering. The shaded region coincides with the portion of the transmitted probe spectrum that was

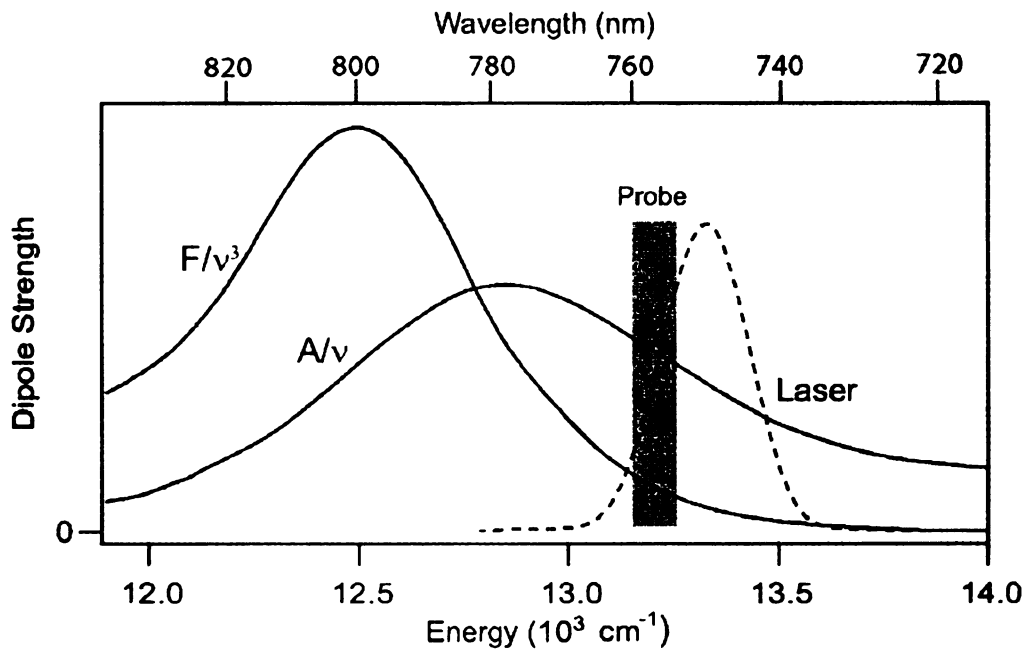


Figure 5.7. Continuous-wave absorption and fluorescence spectra from B777 in ODPS plotted as the dipole strength, $A(\nu)/\nu$ and $F(\nu)/\nu^3$, respectively, and normalized to unit area. The dashed curve shows the intensity spectrum emitted by the ti:sapphire oscillator. The shaded region shows the range of the transmitted probe light that was passed by the monochromator to the detector in the dynamic-absorption experiment.

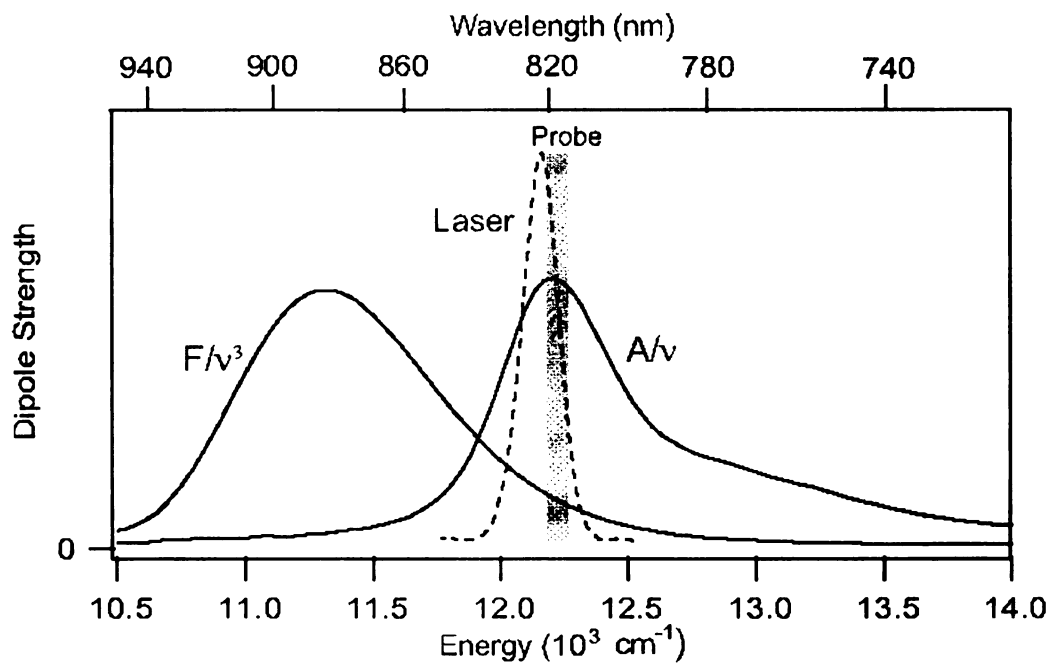


Figure 5.8. Continuous-wave absorption and fluorescence spectra from B820 in OG plotted as the dipole strength, $A(\nu)/\nu$ and $F(\nu)/\nu^3$, respectively, and normalized to unit area. The dashed curve shows the intensity spectrum emitted by the ti:sapphire oscillator. The shaded region shows the range of the transmitted probe light that was passed by the monochromator to the detector in the dynamic-absorption experiment.

passed by the monochromator to the photodiode. The 0–0 vibronic transition in B777 in ODPS occurs in the vicinity of 12800 cm^{-1} (785 nm), as can be seen in figure 5.8. The intensity spectrum from the ti:sapphire laser was centered at 750 nm. As in the experiments described in Chapter 4, the choice of pump spectrum and detected probe band width favors detection of ground-state vibrational coherence. The range of the transmitted probe light can be seen in figure 5.7.

5.2.2 Dynamic-Absorption Experiments

Figure 5.9 shows the dynamic-absorption transient obtained from B777 in ODPS. Following the intense spike near the zero of time, a short series of damped oscillations are observed in the transient prior to 1 ps, as can be seen in the inset of figure 5.9. These strong recurrences correspond to the rapidly damped features discussed in the previous chapters. The dynamic-absorption transient obtained from B820 in OG is shown in figure 5.10. The zoomed inset in figure 5.10 shows the rapidly damped vibrational coherence exhibited by B820, with at least two recurrences lasting as long as 2 ps.

Figures 5.11 and 5.12 present a time-domain modeling of the rapidly damped oscillatory signals from B820 in OG and B777 in ODPS, respectively. In each case, the oscillatory signal was isolated by subtracting a fitted triple-exponential function from the signal starting at 150 fs and extending to the end of the recorded range at 12 ps. The oscillatory residual can be fit to a model consisting of a sum of one or more distributions of damped cosinusoids. As in the time-domain modeling of the signals obtained from the BChl solutions described in Chapter 4, the distributions are defined by,

$$I(t) = \int_0^{\infty} d\omega \mathcal{L}(\omega, A, \omega_0, \Delta\omega, \rho) \cos(\omega t - \phi) e^{-t/\gamma} \quad (5.1)$$

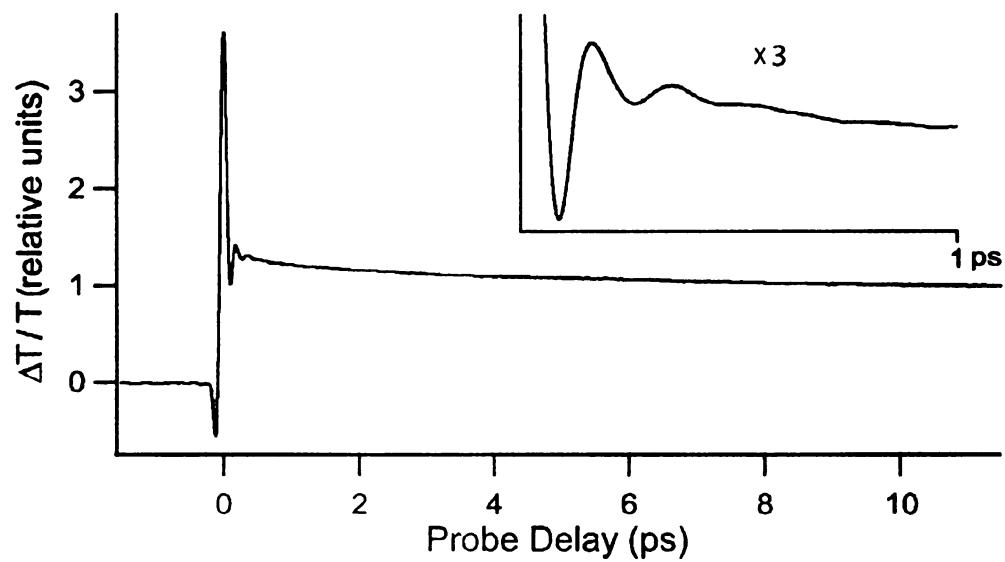


Figure 5.9. Pump-probe signal obtained from B777 in ODPS at room temperature.

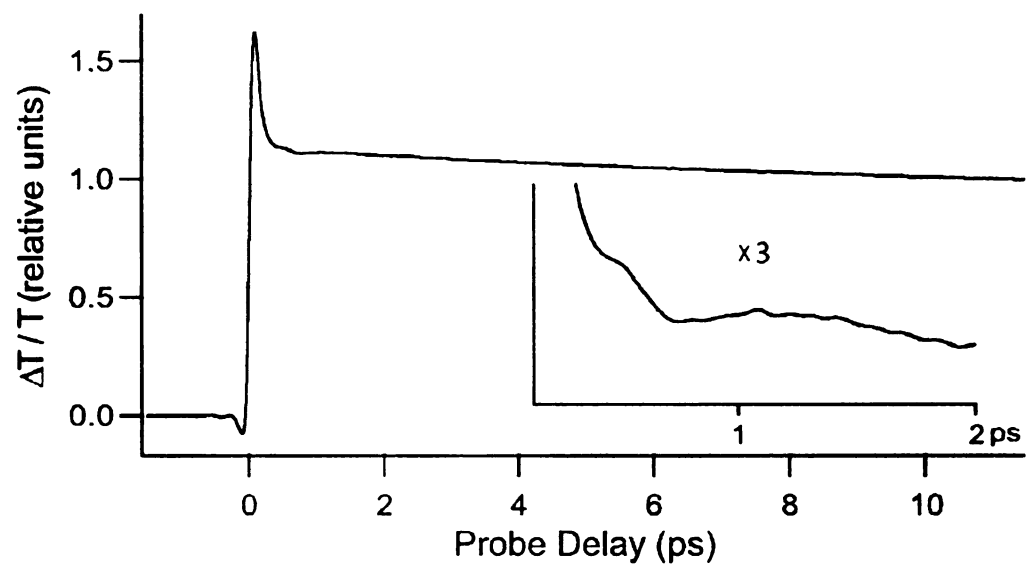


Figure 5.10. Pump-probe signal obtained from B820 in OG at room temperature.

The intensity \mathcal{L} for a cosinusoid of frequency ω is determined here by a log-normal distribution, as parameterized by the area (A), center frequency (ω), width ($\Delta\omega$), and asymmetry ($\rho \geq 1$).²³ The values for the area A report the integral over the distribution $\mathcal{L}(\omega)$,

$$A = \int_0^{\infty} d\omega \mathcal{L}(\omega) \quad (5.2)$$

The distribution was sampled at 5 cm^{-1} intervals from 1 cm^{-1} to 500 cm^{-1} . The intrinsic damping time, γ , was arbitrarily fixed to 1.5 ps.

Figure 5.11 shows that the sum of two distributions of damped cosinusoids is required to fit the early time oscillatory signal from B777 in ODPS. Both distributions were defined by equation 4.2; each was allowed to have an independent phase ϕ and asymmetry ρ . The lognormal components are centered at 147 cm^{-1} and 184 cm^{-1} . A comparison of figure 5.11 and 5.12 shows that the rapidly damped vibrational coherence exhibited by B820 is more than ten times weaker in intensity than that of B777. A model arising from three lognormal distribution functions provides a good description of the signal observed from B820 in OG. The intensity distributions for the three individual components are shown in the lower panel of figure 5.11. Two of the components have fairly narrow line shapes and maxima at 28 cm^{-1} and 102 cm^{-1} . A third component with a broader line shape is observed at 48 cm^{-1} . Note that the three components in the signal from B820 are centered at lower frequencies than observed in B777 or in the BChl solutions described in Chapter 4.

An additional high frequency modulation can also be seen in the signal in figure 5.12 from B820. These features were not considered in the modeling of the rapidly damped

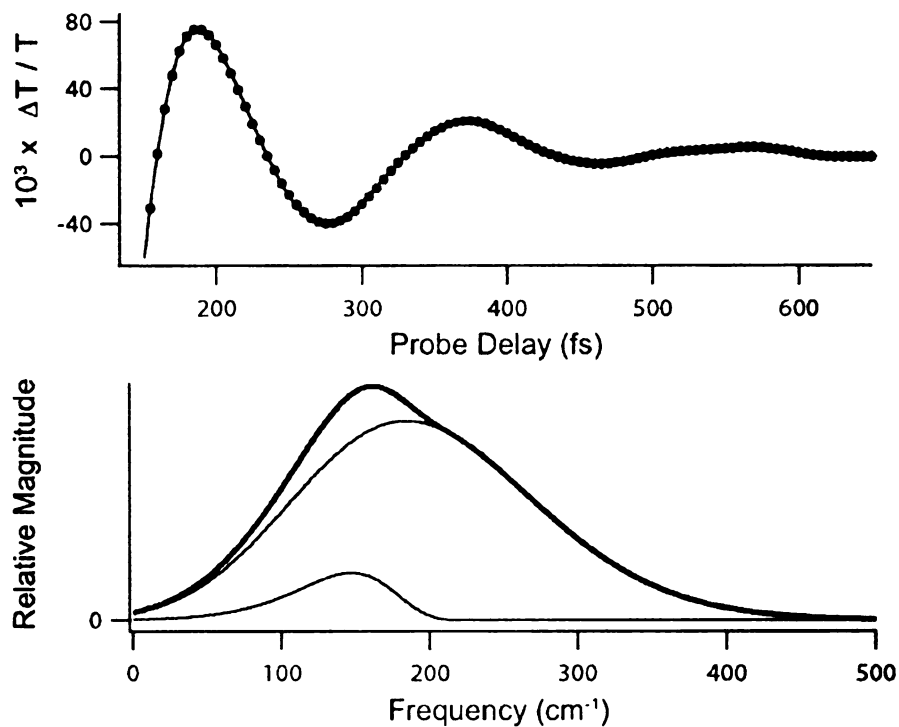


Figure 5.11. Expanded view of the rapidly damped oscillation observed in the dynamic-absorption transient from B777 in ODPS (see figure 5.9) superimposed with a model defined by the sum of two independent log-normal distributions $\mathcal{L}(\omega)$ of damped cosinusoids, each defined by equation 5.2. The scaling of the ordinate is relative to the magnitude of the pump-probe ground-state depletion signal, as in figure 5.9. Bottom: Plots of $\mathcal{L}(\omega)$ for the two components observed in ODPS and their sum, $\mathcal{M}(\omega)$ (thick curve). The model parameters are provided in table 5.1.

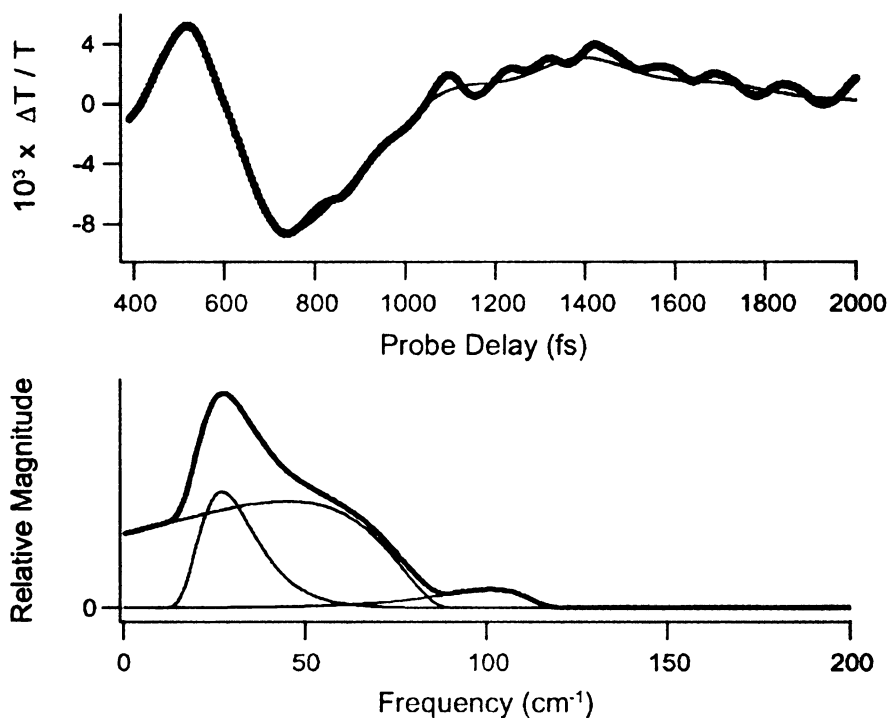


Figure 5.12. Expanded view of the rapidly damped oscillation observed in the dynamic-absorption transient from B820 in OG (see figure 5.10) superimposed with a model defined by the sum of two independent log-normal distributions $\mathcal{L}(\omega)$ of damped cosinusoids, each defined by equation 5.2. The scaling of the ordinate is relative to the magnitude of the pump-probe ground-state depletion signal, as in figure 5.10. Bottom: Plots of $\mathcal{L}(\omega)$ for the two components observed in OG and their sum, $\mathcal{M}(\omega)$ (thick curve). The model parameters are provided in table 5.1.

Table 5.1. Model parameters for the rapidly damped vibrational coherence observed in BChl-containing proteins^a

Component	Parameter ^b	B777	B820
1	ω_0, cm^{-1}	147	28
	$\Delta\omega, \text{cm}^{-1}$	79	20
	ρ	-1.3	1.4
	ϕ, rad	1.514	1.303
	A	0.190	0.081
2	ω_0, cm^{-1}	184	102
	$\Delta\omega, \text{cm}^{-1}$	202	29
	ρ	1.1	-1.5
	ϕ, rad	1.558	-0.035
	A	4.985	0.072
3	ω_0, cm^{-1}	—	48
	$\Delta\omega, \text{cm}^{-1}$	—	100
	ρ	—	-1.8
	ϕ, rad	—	0.5484
	A	—	0.020
Sum	$\langle\omega\rangle, \text{cm}^{-1}$	191	41
	$\sum_i A_i$	1.508	0.084

^a Figures 5.11–5.12

^bSee equations 5.3–5.5 and the text.

oscillations. The damping time for the components is in the range of those assigned to intramolecular vibrations in BChl solutions, see chapter 3.

The model parameters for the rapidly damped vibrational coherence observed in the BChl proteins are compared in table 5.1. As described in chapter 4, an analysis of the mean frequency of the fitted distributions was performed on the signals obtained from B777 and B820. The mean frequency is defined by,

$$\langle \omega \rangle = \frac{\int_0^{\infty} d\omega \mathcal{M}(\omega) \omega}{\int_0^{\infty} d\omega \mathcal{M}(\omega)} \quad (5.3)$$

with the integral calculated over the ω axis with the sum of the distributions $\mathcal{L}_i(\omega)$ from the two or three components,

$$\mathcal{M}(\omega) = \sum_i \mathcal{L}_i(\omega) \quad (5.4)$$

The results are compared in table 5.1. The integrated areas for B777 and B820 are relative to those observed from BChl in neat pyridine, discussed in chapter 4.

5.3 Discussion

5.3.1 Comparison of Line Shapes and Components in the Vibrational Coherence From B777 and B820

As in the BChl solutions (see chapter 4), the rapidly damped vibrational coherence observed in B777 and B820 probably arises from formally intermolecular interactions between groups in the surrounding solvent or protein and the BChl macrocycle. This assignment is based on the comparable line shapes and frequencies observed in the two classes of systems. The changes in the line shape and intensity that occur in moving from

B777 to B820 are consistent with their structures (see figures 5.3 and 5.4). The main issue involves the number and degree of order of the surrounding molecules that attack the BChl macrocycles in the two systems. One face of the BChl macrocycle in B777 is apparently exposed to a large number of mobile dipoles near the aqueous boundary of its detergent micelle, producing a broad component in the vibrational coherence that is very similar to that observed from BChl in the organic solvents.

In contrast, the two BChl macrocycles in B820 are largely protected from solvent molecules, as can be seen in figure 5.13. This space-filling rendering of the B820 system shows that very little of the π -electron density of either BChl macrocycle can be approached by solvent molecules owing to coverage by the α helix on one side and by the adjacent BChl macrocycle on the other. We suggest that this protection leads to the loss of the large component at 184 cm^{-1} in the B777 signal. The detected components in the vibrational coherence in B820 probably arise from a small number of relatively ordered interactions with protein-derived groups, so the intensity of the modulation in the time domain is smaller and the line shapes in the frequency domain are narrower. Additionally, the strongly-coupled electronic character of the B820 system impacts the observed intensity of the vibrational coherence. Delocalization of the π -electron density over both macrocycles in a given B820 molecule would be expected to attenuate the displacement of a given intermolecular interaction between a solvent molecule and the adjacent π -electron density of a given BChl macrocycle. Because the resonance Raman cross section scales with the square of the displacement,^{24,25} the intensity of the ground-state vibrational coherence^{22,26-28} observed in B820 should be intrinsically smaller than observed in the monomeric B777 system.

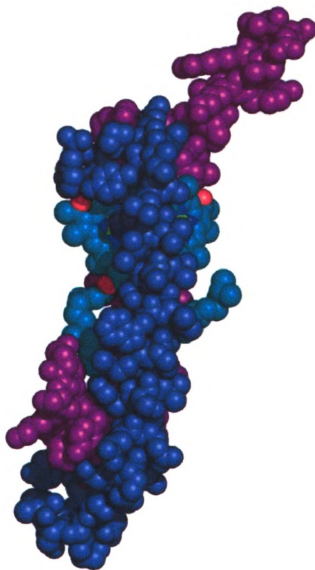


Figure 5.13. Space-filling (CPK) representation of the BChl dimer in the B820 subunit from LH1 based on the calculations of Schulten and coworkers.¹⁵

5.3.2 Assignments for Components in the Vibrational Coherence in B777 and B820

The vibrational coherence from B777 is dominated by a large, broad component at $\sim 184\text{ cm}^{-1}$. The relatively high frequency of this component is similar to those observed in BChl solutions. It is reasonable to assign the 184-cm^{-1} vibrational mode to an ion-dipole interaction arising from the interaction between the BChl macrocycle and the charged end of the detergent molecules in the surrounding micelle. These interactions might resemble those discussed in the previous chapter where dipoles from the first-shell solvent molecules attack the π -electron density above and below the plane of the BChl α macrocycle. The protein, however, introduces the added complexity of a possible interaction with the polypeptide chain as well as the surrounding solvent environment.

A lower frequency component, around 140 cm^{-1} , is also observed in the vibrational coherence from B777. This component is similar in both frequency and line shape to the 110-cm^{-1} mode observed in the vibrational coherence from B820. The narrowed line shapes of these components suggest a more ordered interaction. It is possible, then, that these mode interactions involve an attack on the π -electron density of the BChl monomer or dimer by specific polar residues from the surrounding protein medium. The presence of a large, non-zero intensity component in B820, in the $0\text{--}15\text{-cm}^{-1}$ regime, suggests that a significant fraction of the signal also arises from a *collective* interaction between the BChl dimer and polar groups attached to the polypeptide backbone.

We can compare the vibrations in B820 to those in B777 without much consideration of the strong electronic coupling between the two BChl macrocycles in B820 because the experiment was designed to detect mostly ground-state wave packet motion, and only the lower exciton state in B820 is pumped. It has been long suspected,²⁹⁻³¹ however, that an

interdimer mode, in which the two macrocycles vibrate with respect to each other, should be observed in the resonance Raman spectrum in the $< 100 \text{ cm}^{-1}$ region. In the strong electronic coupling limit, the π -electron density is delocalized over both macrocycles and effectively produce a supermolecule. Warshel and coworkers²⁹⁻³¹ predicted the interdimer mode to be at about 100 cm^{-1} for the special pair in the reaction center of *Rhodobacter sphaeroides*. Bocian and coworkers,³² in contrast, have speculated that this mode should be observed around 30 cm^{-1} . The interaction between the two BChls in B820 is weaker than that in the reaction center, so the interdimer mode might be observed at a somewhat lower frequency. The 30 cm^{-1} mode observed in B820 might arise from the interaction between the BChl and the polypeptide chain, but a similar feature is not observed in the vibrational coherence from B777. Therefore, it is attractive to assign the 30 cm^{-1} feature in B820 to an interdimer vibrational.

5.3.3 BChl-Protein Interactions in B820 and in the Photosynthetic Reaction Center

As discussed in the last section, the components in the rapidly-damped vibrational coherence in B820 and B777 that have relatively narrow line shapes may arise from interactions with polar amino acid residues in the surrounding protein structure. A similar argument might be applied to the vibrational coherence from P in the photosynthetic reaction center, where site-directed mutations were observed to cause frequency shifts.³³ In the following, we consider structural assignments for some of these interactions.

In B820, only a small number of the polar residues are close enough, within 6 \AA of the BChl dimer, to be capable of interacting directly with the π -electron density. Figure 5.14 and table 5.2 show these possible residues. The tabulated distances were estimated

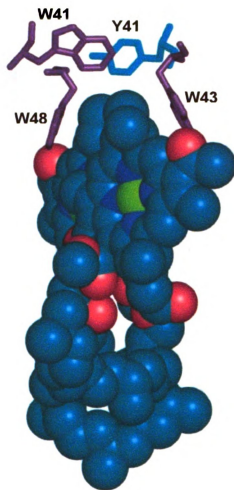


Figure 5.14. Model of the BChl dimer in the B820 subunit from LH1 based on the calculations of Schulten and coworkers.¹⁵ The polar residues in the vicinity of the dimer are shown as line structures; tryptophan 41, tryptophan 43, tryptophan 48, and tyrosine 41. These residues are possible candidates for the interaction between the π -electron density of the dimer and the protein medium. In order to simplify the figure, the axially coordinated histidines, H32 and H39, are not shown.

Table 5.2. Potential residue candidates for the interaction between the BChl dimer and the surrounding protein medium in B820^a

Residue	Distance (Å)^b
Y41	5.51
W43	4.44
W45	3.24
W48	5.53

^a Model of the B820 subunit from LH1 based on the calculations of Schulten and coworkers.¹⁵

^b The distances were estimated using Pymol.³⁴

using Pymol³⁴ from the B820 model developed by Hu and Schulten.¹⁵ In the reaction center from *Rhodobacter sphaeroides*, the residues within 6 Å of P are indicated in figure 5.15 and table 5.3. There are several residues in the reaction center of *R. sphaeroides* that are at comparable distances from the BChl dimer as those in B820. Vos, Martin, and coworkers showed that the vibrational coherence from P* exhibits frequency shifts and intensity changes in response to a range of point mutations that altered the hydrogen-bonding pattern between the pair of BChl macrocycles and the surrounding protein structure. Specifically, the removal of the hydrogen bond between H168 (see figure 5.15) and the protein resulted in significant changes to the vibrational spectrum.³³

5.4 Conclusions and Future Work

The work described in this thesis provides a new perspective on the structural origin of the vibrational modes that control the dynamics of electron transfer in purple bacterial reaction centers. In solution, the intermolecular modes between BChl and its clustered polar solvent molecules make a dominant contribution to the low-frequency vibrational coherence, but the frequency dependence of the intermolecular mode as a function of the solvent's dipole moment shows that the London dispersion interaction, arising from the polarizability of the surrounding molecules, makes a significant contribution. In a hydrophobic region, such as in the transmembrane region of the reaction center, the dispersion interaction would be expected to be especially important. The presence of a few polar side chains in the neighborhood, as discussed in the previous section, would afford a tuning of the coupled mode frequency so that the reorganization energy and the driving force could be precisely matched. Reorganization of the protein medium, through

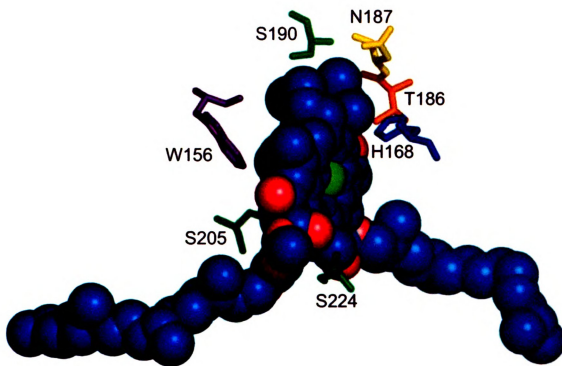


Figure 5.15. The primary electron donor, P, from the reaction center from *Rhodobacter sphaeroides*. The polar residues in the vicinity of the special pair are shown as line structures; serine 190, serine 205, serine 224, tryptophan 156, asparagine 187, threonine 186, and histidine 168. These residues are possible candidates for the interaction between the π -electron density of the special pair and the protein medium. In order to simplify the figure, the axially coordinated histidines, H173 and H202, are not shown.

Table 5.3. Potential residue candidates for the interaction between the BChl dimer and the surrounding protein medium in *Rhodobacter sphaeroides*^a

Residue	Distance (Å)^b
W156	4.64
H168	3.46
T186	3.65
N187	5.07
S190	4.42
S205	4.62
S244	4.25

^a Structure obtained from the RCSB Protein Data Bank.³⁵

^b The distances were estimated using Pymol.³⁴

polar and nonpolar (viscoelastic) solvation responses,³⁶⁻³⁸ would be expected to play an additional, energy dissipative role in the dynamics that affords control over the reversibility of the charge-separation reactions. These ideas can be tested in experiments that probe the nature of the line shape and the mode frequency for the intermolecular mode in protein hosts.

A project that can potentially provide a more sophisticated understanding of the solvent-derived intermolecular modes would involve studies of low-frequency vibrational coherence in free-base and Zn(II)-substituted porphyrin systems in solution. Porphyrin compounds are frequently used as components in artificial light-harvesting arrays³⁹⁻⁴⁴ and donor-acceptor.⁴⁵⁻⁴⁷ An advantage to using porphyrins as a target system is that they can be studied as isolated chromophores and as parts of charge-transfer complexes. The Zn(II) porphyrins are structurally comparable to the BChl systems. As a result, the intermolecular modes between porphyrins and the cluster solvent molecules should be comparable to the ones we have studied in the bacteriochlorophyll systems as described in this thesis.

5.5 References

- (1) Zuber, H. In *The Photosynthetic Reaction Center*; Deisenhofer, J., Ed.; Academic Press, Inc.: San Diego, 1993; Vol. I, p 43–100.
- (2) Kühlbrandt, W.; Wang, D. N. *Nature* **1991**, *350*, 130–134.
- (3) Kühlbrandt, W.; Wang, D. N.; Fujiyoshi, Y. *Nature* **1994**, *367*, 614–621.
- (4) Miller, J. F.; Hinchigeri, S. B.; Parkes-Loach, P. S.; Callahan, P. M.; Sprinkle, J. R.; Riccobono, J. R.; Loach, P. A. *Biochemistry* **1987**, *26*, 5055–5062.
- (5) Parkes-Loach, P. S.; Sprinkle, J. R.; Loach, P. A. *Biochemistry* **1988**, *27*, 2718–2727.
- (6) van Mourik, F.; van der Oord, C. J. R.; Visscher, K. J.; Parkes-Loach, P. S.; Loach, P. A.; Visschers, R. W.; van Grondelle, R. *Biochim. Biophys. Acta* **1991**, *1059*, 111–119.
- (7) Visschers, R. W.; Nunn, R.; Calkoen, F.; van Mourik, F.; Hunter, C. N.; Rice, D. W.; van Grondelle, R. *Biochim. Biophys. Acta* **1992**, *1100*, 259–266.
- (8) Visschers, R. W.; van Mourik, F.; Monshouwer, R.; van Grondelle, R. *Biochim. Biophys. Acta* **1993**, *1141*, 238–244.
- (9) Visschers, R. W.; van Grondelle, R.; Robert, B. *Biochim. Biophys. Acta* **1993**, *1183*, 369–373.
- (10) Pullerits, T.; van Mourik, F.; Monshouwer, R.; Visschers, R. W.; van Grondelle, R. *J. Lumin.* **1994**, *58*, 168–171.
- (11) Visser, H. M.; Somsen, O. J. G.; van Mourik, F.; Lin, S.; van Stokkum, I. H. M.; van Grondelle, R. *Biophys. J.* **1995**, *69*, 1083–1099.
- (12) Pullerits, T.; Sundström, V. *Acc. Chem. Res.* **1996**, *29*, 381–389.
- (13) Monshouwer, R.; van Grondelle, R. *Biochim. Biophys. Acta* **1996**, *1275*, 70–75.
- (14) Creemers, T. M. H.; De Caro, C. A.; Visschers, R. W.; van Grondelle, R.; Völker, S. *J. Phys. Chem. B* **1999**, *103*, 9770–9776.
- (15) Hu, X.; Schulten, K. *Biophys. J.* **1998**, *75*, 683–694.
- (16) McDermott, G.; Prince, S. M.; Freer, A. A.; Hawthornthwaite-Lawless, A. M.; Papiz, M. Z.; Cogdell, R. J.; Isaacs, N. W. *Nature* **1995**, *374*, 517–521.
- (17) Karrasch, S.; Bullough, P. A.; Ghosh, R. *EMBO J.* **1995**, *14*, 631–638.

- (18) Jordan, P.; Fromme, P.; Witt, H. T.; Klukas, O.; Saenger, W.; Krauß, N. *Nature* **2001**, *411*, 909–917.
- (19) Rhee, K.-H.; Morris, E. P.; Barber, J.; Kühlbrandt, W. *Nature* **1998**, *396*, 283–286.
- (20) Cohen-Bazire, G.; Sistrom, W. R.; Stanier, R. Y. *J. Cell. Comp. Physiol.* **1957**, *49*, 25–43.
- (21) Loach, P. A.; Androes, G. M.; Maksim, A. F.; Calvin, M. *Photochem. Photobiol.* **1964**, *2*, 443–454.
- (22) Pollard, W. T.; Mathies, R. A. *Annu. Rev. Phys. Chem.* **1992**, *43*, 497–523.
- (23) Siano, D. B.; Metzler, D. E. *J. Chem. Phys.* **1969**, *51*, 1856–1861.
- (24) Tang, J.; Albrecht, A. C. In *Raman Spectroscopy: Theory and Practice*; Szymanski, H. A., Ed.; Plenum: New York, 1970; Vol. 2, p 33–68.
- (25) Myers, A. B.; Mathies, R. A. In *Biological Applications of Raman Spectroscopy*; Spiro, T. G., Ed.; Wiley-Interscience: New York, 1987; Vol. 2, *Resonance Raman Spectra of Polyenes and Aromatics*, p 1–58.
- (26) Pollard, W. T.; Lee, S.-Y.; Mathies, R. A. *J. Chem. Phys.* **1990**, *92*, 4012–4029.
- (27) Pollard, W. T.; Dexheimer, S. L.; Wang, Q.; Peteanu, L. A.; Shank, C. V.; Mathies, R. A. *J. Phys. Chem.* **1992**, *96*, 6147–6158.
- (28) Johnson, A. E.; Myers, A. B. *J. Chem. Phys.* **1996**, *104*, 2497–2507.
- (29) Warshel, A. *Proc. Natl. Acad. Sci. USA* **1980**, *77*, 3105–3109.
- (30) Warshel, A.; Parson, W. W. *J. Am. Chem. Soc.* **1987**, *109*, 6143–6152.
- (31) Warshel, A.; Creighton, S.; Parson, W. W. *J. Phys. Chem.* **1988**, *92*, 2696–2701.
- (32) Czarniecki, K.; Diers, J. R.; Chynwat, V.; Erickson, J. P.; Frank, H. A.; Bocian, D. F. *J. Am. Chem. Soc.* **1997**, *119*, 415–426.
- (33) Rischel, C.; Spiedel, D.; Ridge, J. P.; Jones, M. R.; Breton, J.; Lambry, J.-C.; Martin, J.-L.; Vos, M. H. *Proc. Natl. Acad. Sci. USA* **1998**, *95*, 12306–12311.
- (34) *Pymol*; Delano Scientific LLC: San Francisco, CA.
- (35) Stowell, M. H., McPhillips, T.M., Rees, D.C., Soltis, S.M., Abresch, E., Feher, G. *Science* **1997**, *279*, 812–816.

- (36) Lampa-Pastirk, S.; Lafuente, R. C.; Beck, W. F. *J. Phys. Chem. B* **2004**, *108*, 12602–12607.
- (37) Berg, M. *J. Phys. Chem. A* **1998**, *102*, 17–30.
- (38) Berg, M. *J. Chem. Phys.* **1999**, *110*, 8577–8588.
- (39) Prathapan, S.; Johnson, T. E.; Lindsey, J. S. *J. Am. Chem. Soc.* **1993**, *115*, 7519–7520.
- (40) Hsiao, J.-S.; Krueger, B. P.; Wagner, R. W.; Johnson, T. E.; Delayen, J. K.; Mauzerall, D. C.; Fleming, G. R.; Lindsey, J. S.; Bocian, D. F.; Donohoe, R. J. *J. Am. Chem. Soc.* **1996**, *118*, 11181–11193.
- (41) Loewe, R. S.; Lammi, R. K.; Diers, J. R.; Kirmaier, C.; Bocian, D. F.; Holten, D.; Lindsey, J. S. *J. Mater. Chem.* **2002**, *12*, 1530–1552.
- (42) Bothner-By, A. A.; Dadok, J.; Johnson, T. E.; Lindsey, J. S. *J. Phys. Chem.* **1996**, *100*, 17551–17557.
- (43) Strachan, J.-P.; Gentemann, S.; Seth, J.; Kalsbeck, W. A.; Lindsey, J. S.; Holten, D.; Bocian, D. F. *J. Am. Chem. Soc.* **1997**, *119*, 11191–11201.
- (44) Yatskou, M. M.; Koehorst, R. B. M.; van Hoek, A.; Donker, H.; Schaafsma, T. J.; Gobets, B.; van Stokkum, I.; van Grondelle, R. *J. Phys. Chem. A* **2001**, *105*, 11432–11440.
- (45) Wagner, R. W.; Lindsey, J. S. *J. Am. Chem. Soc.* **1994**, *116*, 9759–9760.
- (46) Wagner, R. W.; Lindsey, J. S.; Seth, J.; Palaniappan, V.; Bocian, D. F. *J. Am. Chem. Soc.* **1996**, *118*, 3996–3997.
- (47) Prathapan, S.; Yang, S. I.; Seth, J.; Miller, M. A.; Bocian, D. F.; Holten, D.; Lindsey, J. S. *J. Phys. Chem. B* **2001**, *105*, 8237–8248.

MICHIGAN STATE UNIVERSITY LIBRARIES



3 1293 02845 5263